

# AN IMPROVED MODEL OF HIGH-LATITUDE F-REGION SCINTILLATION (WBMOD VERSION 13)

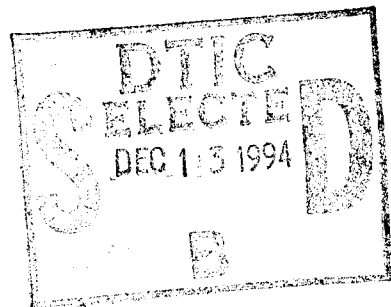
James A. Secan  
Robert M. Bussey

Northwest Research Associates, Inc.  
PO Box 3027  
Bellevue, WA 98009-3027

31 August 1994

Final Report  
1 September 1993 through 31 August 1994

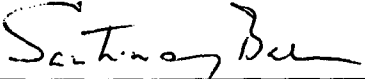
Approved for public release; distribution unlimited



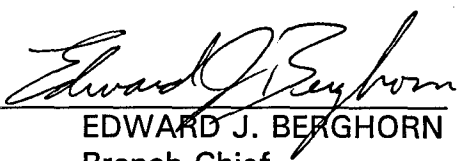
**PHILLIPS LABORATORY**  
**Directorate of Geophysics**  
**AIR FORCE MATERIEL COMMAND**  
**HANSCOM AIR FORCE BASE, MA 01731-3010**

1994/2/17 10:25

"This technical report has been reviewed and is approved for publication"

  
SANTIMAY BASU

Contract Manager

  
EDWARD J. BERGHORN  
Branch Chief

  
WILLIAM K. VICKERY

Division Director

This document has been reviewed by the ESC Public Affairs Office (PA) and is releasable to the National Technical Information Service (NTIS).

Qualified requestors may obtain additional copies from the Defense Technical Information Center. All others should apply to the National Technical Information Service.

If your address has changed, or if you wish to be removed from the mailing list, or if the addressee is no longer employed by your organization, please notify PL/IM, 29 Randolph Road, Hanscom AFB, MA 01731-3010. This will assist us in maintaining a current mailing list.

Do not return copies of this report unless contractual obligations or notices on a specific document requires that it be returned.

REPORT DOCUMENTATION PAGE			Form Approved OMB No. 0704-0188
<p>Public reporting burden for this collection of information is estimated to average 1 hour per response, including the time for reviewing instructions, searching existing data sources, gathering and maintaining the data needed, and completing and reviewing the collection of information. Send comments regarding this burden estimate or another aspect of this collection of information, including suggestions for reducing this burden, to Washington Headquarters Services, Directorate for Information Operations and Reports, 1215 Jefferson Davis Highway, Suite 1204, Arlington, VA 22202-4302, and to the Office of Management and Budget, Paperwork Reduction Project (0704-0188), Washington, DC 20503.</p>			
1. AGENCY USE ONLY (Leave blank)	2. REPORT DATE	3. REPORT TYPE AND DATES COVERED	
	31 August 1994	Final Report, 1 September 1993 through 31 August 1994	
4. TITLE AND SUBTITLE  An Improved Model of High-Latitude F-Region Scintillation (WBMOD Version 13)		5. FUNDING NUMBERS  F19628-91-C-0152 PE63707F PR AWS9 TA 10 WU AA	
6. AUTHOR(S)  James A. Secan, Robert M. Bussey			
7. PERFORMING ORGANIZATION NAME(S) AND ADDRESS(ES)  Northwest Research Associates, Inc. 300 120th Ave NE, Bldg 7, Ste 220 P.O. Box 3027 Bellevue, WA 98009-3027		8. PERFORMING ORGANIZATION REPORT NUMBER  NWRA-CR-94-R120	
9. SPONSORING / MONITORING AGENCY NAME(S) AND ADDRESS(ES)  Phillips Laboratory 29 Randolph Road Hanscom AFB, MA 01731-3010 Contract Manager: Santimay Basu/GPIA		10. SPONSORING / MONITORING AGENCY REPORT NUMBER  PL-TR-94-2254	
11. SUPPLEMENTARY NOTES  The model development will benefit AF Space Forecast Center to support customers requiring climatological specification of C3I outages for any earth-to-satellite link with satellite altitude above 700 km and at any frequency above 100 MHz.			
12a. DISTRIBUTION / AVAILABILITY STATEMENT  Approved for public release; distribution unlimited		12b. DISTRIBUTION CODE	
13. ABSTRACT (Maximum 200 words)  Many modern military systems used for communications, command and control, navigation, and surveillance depend on reliable and relatively noise-free transmission of radiowave signals through the earth's ionosphere. Small-scale irregularities in the ionospheric density can cause severe distortion, known as radiowave scintillation, of both the amplitude and phase of these signals. The WBMOD computer program can be used to estimate these effects on a wide range of systems. The objective of this study is to investigate improvements to the WBMOD model based on extensive data sets covering both the equatorial and high-latitude regimes. This report summarizes the work completed during the third year of this project, which includes completion of the new model for the high-latitude (auroral and polar cap) region of the WBMOD model.			
14. SUBJECT TERMS  Ionosphere, Ionospheric density irregularities, High-latitude radiowave scintillation, Ionospheric modelling, Scintillation, Command control communication		15. NUMBER OF PAGES 92	
		16. PRICE CODE	
17. SECURITY CLASSIFICATION OF REPORT  Unclassified	18. SECURITY CLASSIFICATION OF THIS PAGE  Unclassified	19. SECURITY CLASSIFICATION OF ABSTRACT  Unclassified	20. LIMITATION OF ABSTRACT  SAR



## CONTENTS

	Page
Preface	ix
1. Introduction	1
2. A Brief History of WBMOD	1
3. High Latitude Model Development	2
3.1 Modeling Philosophy	3
3.2 Variation with Geophysical Conditions	3
3.3 Seasonal/Longitudinal Variation	18
3.4 Modification to Mid-Latitude $\log(C_k L)$ Model	31
3.5 Variation of the $\log(C_k L)$ PDF Width	32
3.6 Comparison with Narssarssuaq Observations	33
4. WBMOD Version 13	33
5. Conclusion	33
References	37
Appendix A. Grey-Shade Plots of High-Latitude $\log(C_k L)$ .	41
Appendix B. Results of High-Latitude $\log(C_k L)$ Modeling	55

DTIC QUALITY INSPECTOR: 0

Accession For	
NTIS GRAIL	<input checked="" type="checkbox"/>
DTIC TAB	<input type="checkbox"/>
Unclassified	<input type="checkbox"/>
Justification	
By	
Distribution/Av	
Availability Codes	
1	Avail and/or Specified
2	Specified
3	
4	
5	
6	
7	
8	
9	
10	
11	
12	
13	
14	
15	
16	
17	
18	
19	
20	
21	
22	
23	
24	
25	
26	
27	
28	
29	
30	
31	
32	
33	
34	
35	
36	
37	
38	
39	
40	
41	
42	
43	
44	
45	
46	
47	
48	
49	
50	
51	
52	
53	
54	
55	
56	
57	
58	
59	
60	
61	
62	
63	
64	
65	
66	
67	
68	
69	
70	
71	
72	
73	
74	
75	
76	
77	
78	
79	
80	
81	
82	
83	
84	
85	
86	
87	
88	
89	
90	
91	
92	
93	
94	
95	
96	
97	
98	
99	
100	
101	
102	
103	
104	
105	
106	
107	
108	
109	
110	
111	
112	
113	
114	
115	
116	
117	
118	
119	
120	
121	
122	
123	
124	
125	
126	
127	
128	
129	
130	
131	
132	
133	
134	
135	
136	
137	
138	
139	
140	
141	
142	
143	
144	
145	
146	
147	
148	
149	
150	
151	
152	
153	
154	
155	
156	
157	
158	
159	
160	
161	
162	
163	
164	
165	
166	
167	
168	
169	
170	
171	
172	
173	
174	
175	
176	
177	
178	
179	
180	
181	
182	
183	
184	
185	
186	
187	
188	
189	
190	
191	
192	
193	
194	
195	
196	
197	
198	
199	
200	
201	
202	
203	
204	
205	
206	
207	
208	
209	
210	
211	
212	
213	
214	
215	
216	
217	
218	
219	
220	
221	
222	
223	
224	
225	
226	
227	
228	
229	
230	
231	
232	
233	
234	
235	
236	
237	
238	
239	
240	
241	
242	
243	
244	
245	
246	
247	
248	
249	
250	
251	
252	
253	
254	
255	
256	
257	
258	
259	
260	
261	
262	
263	
264	
265	
266	
267	
268	
269	
270	
271	
272	
273	
274	
275	
276	
277	
278	
279	
280	
281	
282	
283	
284	
285	
286	
287	
288	
289	
290	
291	
292	
293	
294	
295	
296	
297	
298	
299	
300	
301	
302	
303	
304	
305	
306	
307	
308	
309	
310	
311	
312	
313	
314	
315	
316	
317	
318	
319	
320	
321	
322	
323	
324	
325	
326	
327	
328	
329	
330	
331	
332	
333	
334	
335	
336	
337	
338	
339	
340	
341	
342	
343	
344	
345	
346	
347	
348	
349	
350	
351	
352	
353	
354	
355	
356	
357	
358	
359	
360	
361	
362	
363	
364	
365	
366	
367	
368	
369	
370	
371	
372	
373	
374	
375	
376	
377	
378	
379	
380	
381	
382	
383	
384	
385	
386	
387	
388	
389	
390	
391	
392	
393	
394	
395	
396	
397	
398	
399	
400	
401	
402	
403	
404	
405	
406	
407	
408	
409	
410	
411	
412	
413	
414	
415	
416	
417	
418	
419	
420	
421	
422	
423	
424	
425	
426	
427	
428	
429	
430	
431	
432	
433	
434	
435	
436	
437	
438	
439	
440	
441	
442	
443	
444	
445	
446	
447	
448	
449	
450	
451	
452	
453	
454	
455	
456	
457	
458	
459	
460	
461	
462	
463	
464	
465	
466	
467	
468	
469	
470	
471	
472	
473	
474	
475	
476	
477	
478	
479	
480	
481	
482	
483	
484	
485	
486	
487	
488	
489	
490	
491	
492	
493	
494	
495	
496	
497	
498	
499	
500	
501	
502	
503	
504	
505	
506	
507	
508	
509	
510	
511	
512	
513	
514	
515	
516	
517	
518	
519	
520	
521	
522	
523	
524	
525	
526	
527	
528	
529	
530	
531	
532	
533	
534	
535	
536	
537	
538	
539	
540	
541	
542	
543	
544	
545	
546	
547	
548	
549	
550	
551	
552	
553	
554	
555	
556	
557	
558	
559	
560	
561	
562	
563	
564	
565	
566	
567	
568	
569	
570	
571	
572	
573	
574	
575	
576	
577	
578	
579	
580	
581	
582	
583	
584	
585	
586	
587	
588	
589	
590	
591	
592	
593	
594	
595	
596	
597	
598	
599	
600	
601	
602	
603	
604	
605	
606	
607	
608	
609	
610	
611	
612	
613	
614	
615	
616	
617	
618	
619	
620	
621	
622	
623	
624	
625	
626	
627	
628	
629	
630	
631	
632	
633	
634	
635	
636	
637	
638	
639	
640	
641	
642	
643	
644	
645	
646	
647	
648	
649	
650	
651	
652	
653	
654	
655	
656	

## Illustrations

1	Composite shade plot of $\log(C_k L)$ for all $SSN$ and all $K_p$ . The radial axis is the latitude distance from the SSJ/4 precipitation boundary (solid white line) and the azimuthal coordinate is geomagnetic (apex) local time. The solid white circle indicates the zero point for the radial axis ( <i>i.e.</i> , the SSJ/4 boundary) .....	5
2	Variation of $\log(C_k L)$ with the latitude distance from the SSJ/4 precipitation boundary for six geomagnetic (apex) local time ranges. Data are from all HiLat/Polar BEAR stations for all $SSN$ and all $K_p$ .....	6
3	Continuation of comparison in Figure 2. ....	7
4	Variation of $\log(C_k L)$ with the latitude distance from the SSJ/4 precipitation boundary for six geomagnetic (apex) local time ranges for all $SSN$ and all $K_p$ . The light solid curve indicates the observations, the heavy solid curve the new high-latitude model, and the heavy dashed curve the current WBMOD high-latitude model. ....	13
5	Continuation of comparison in Figure 4. ....	14
6	Variation of the residual $\log(C_k L)$ as a function of days since the launch of HiLat at Tromso (top plot), Sondre Stromfjord (middle plot), and Ft. Churchill (bottom plot) for the night sector (2100 to 0300 GMLT). ....	19
7	Same as Figure 6 for the noon sector (0900 to 1500 GMLT). ....	20
8	Same as Figure 6 for the AM sector (0300 to 0900 GMLT). ....	21
9	Same as Figure 6 for the PM sector (1500 to 2100 GMLT). ....	22
10	Data from Figure 6 (night sector) with the results of the regression analysis (dotted curve). ....	24
11	Data from Figure 7 (noon sector) with the results of the regression analysis (dotted curve). ....	25
12	Data from Figure 8 (AM sector) with the results of the regression analysis (dotted curve). ....	26
13	Data from Figure 9 (PM sector) with the results of the regression analysis (dotted curve). ....	27
14	Location of stations used in the analysis. ....	28

15	Variation of the residual $\log(C_k L)$ as a function of days since the launch of Wideband at Poker Flat for the night (top plot) and day (bottom plot) sectors. Also shown is the regression fit to these data (dotted curves).	29
16	Variation of $\sigma_{SD}$ with the latitude distance from the SSJ/4 precipitation boundary for six geomagnetic (apex) local time ranges for all $SSN$ and all $K_p$ for all four HiLat/Polar BEAR stations (solid curve: Bellevue; dotted curve: Tromso; short-dash curve: Ft. Churchill; long-dash curve: Sondre Stromfjord). The heavy dotted line indicates the value for $\sigma_{SD}$ corresponding to WBMOD Version 12, and the heavy dotted line indicates the new value.	34
17	Continuation of comparison in Figure 16.	35
18	Observed seasonal variation of scintillation at Narssarssuaq, Greenland (from <i>Basu</i> [1975]).	36
19	Modeled seasonal variation at Narssarssuaq. The solid line is the percent of time that $S_4 \geq 30\%$ and the dotted line is the average $S_4$ .	36
20	Composite shade plot of $\log(C_k L)$ for all $SSN$ and all $K_p$ . The radial axis is the latitude distance from the auroral precipitation boundary (solid white line) and the azimuthal coordinate is geomagnetic (apex) local time. The solid white circle indicates the zero point for the radial axis ( <i>i.e.</i> , the auroral precipitation boundary).	42
21	Composite shade plot of $\log(C_k L)$ for all $K_p$ and $0 \leq SSN \leq 25$ . Axis definition and annotation are as in Figure 20.	43
22	Composite shade plot of $\log(C_k L)$ for all $K_p$ and $25 \leq SSN \leq 50$ . Axis definition and annotation are as in Figure 20.	44
23	Composite shade plot of $\log(C_k L)$ for all $K_p$ and $50 \leq SSN \leq 75$ . Axis definition and annotation are as in Figure 20.	45
24	Composite shade plot of $\log(C_k L)$ for all $K_p$ and $75 \leq SSN \leq 100$ . Axis definition and annotation are as in Figure 20.	46
25	Composite shade plot of $\log(C_k L)$ for all $K_p$ and $100 \leq SSN \leq 125$ . Axis definition and annotation are as in Figure 20.	47
26	Composite shade plot of $\log(C_k L)$ for all $K_p$ and $SSN \geq 125$ . Axis definition and annotation are as in Figure 20.	48
27	Composite shade plot of $\log(C_k L)$ for all $SSN$ and $0^\circ \leq K_p \leq 1^\circ$ . Axis definition and annotation are as in Figure 20.	49

28	Composite shade plot of $\log(C_k L)$ for all SSN and $1^\circ \leq K_p \leq 2^\circ$ . Axis definition and annotation are as in Figure 20.	50
29	Composite shade plot of $\log(C_k L)$ for all SSN and $2^\circ \leq K_p \leq 3^\circ$ . Axis definition and annotation are as in Figure 20.	51
30	Composite shade plot of $\log(C_k L)$ for all SSN and $3^\circ \leq K_p \leq 4^\circ$ . Axis definition and annotation are as in Figure 20.	52
31	Composite shade plot of $\log(C_k L)$ for all SSN and $4^\circ \leq K_p \leq 5^\circ$ . Axis definition and annotation are as in Figure 20.	53
32	Composite shade plot of $\log(C_k L)$ for all SSN and $K_p \geq 5^\circ$ . Axis definition and annotation are as in Figure 20.	54
33	Comparison of WBMOD Version 12.02 (heavy dashed line) and SCINT- MOD Version 1.0 (heavy solid line) to composite observations of $\log(C_k L)$ (light solid line) for all SSN and all $K_p$ .	56
34	Continuation of comparison in Figure 33.	57
35	Comparison of WBMOD Version 12.02 (heavy dashed line) and SCINT- MOD Version 1.0 (heavy solid line) to composite observations of $\log(C_k L)$ (light solid line) for all $K_p$ and $0 \leq SSN \leq 25$ .	58
36	Continuation of comparison in Figure 35.	59
37	Comparison of WBMOD Version 12.02 (heavy dashed line) and SCINT- MOD Version 1.0 (heavy solid line) to composite observations of $\log(C_k L)$ (light solid line) for all $K_p$ and $25 \leq SSN \leq 50$ .	60
38	Continuation of comparison in Figure 37.	61
39	Comparison of WBMOD Version 12.02 (heavy dashed line) and SCINT- MOD Version 1.0 (heavy solid line) to composite observations of $\log(C_k L)$ (light solid line) for all $K_p$ and $50 \leq SSN \leq 75$ .	62
40	Continuation of comparison in Figure 39.	63
41	Comparison of WBMOD Version 12.02 (heavy dashed line) and SCINT- MOD Version 1.0 (heavy solid line) to composite observations of $\log(C_k L)$ (light solid line) for all $K_p$ and $75 \leq SSN \leq 100$ .	64
42	Continuation of comparison in Figure 41.	65
43	Comparison of WBMOD Version 12.02 (heavy dashed line) and SCINT- MOD Version 1.0 (heavy solid line) to composite observations of $\log(C_k L)$ (light solid line) for all $K_p$ and $100 \leq SSN \leq 125$ .	66

44	Continuation of comparison in Figure 43. ....	67
45	Comparison of WBMOD Version 12.02 (heavy dashed line) and SCINT- MOD Version 1.0 (heavy solid line) to composite observations of $\log(C_k L)$ (light solid line) for all $K_p$ and $SSN \geq 125$ .	68
46	Continuation of comparison in Figure 45. ....	69
47	Comparison of WBMOD Version 12.02 (heavy dashed line) and SCINT- MOD Version 1.0 (heavy solid line) to composite observations of $\log(C_k L)$ (light solid line) for all $SSN$ and $0^\circ \leq K_p \leq 1^\circ$ .	70
48	Continuation of comparison in Figure 47. ....	71
49	Comparison of WBMOD Version 12.02 (heavy dashed line) and SCINT- MOD Version 1.0 (heavy solid line) to composite observations of $\log(C_k L)$ (light solid line) for all $SSN$ and $1^\circ \leq K_p \leq 2^\circ$ .	72
50	Continuation of comparison in Figure 49. ....	73
51	Comparison of WBMOD Version 12.02 (heavy dashed line) and SCINT- MOD Version 1.0 (heavy solid line) to composite observations of $\log(C_k L)$ (light solid line) for all $SSN$ and $2^\circ \leq K_p \leq 3^\circ$ .	74
52	Continuation of comparison in Figure 50. ....	75
53	Comparison of WBMOD Version 12.02 (heavy dashed line) and SCINT- MOD Version 1.0 (heavy solid line) to composite observations of $\log(C_k L)$ (light solid line) for all $SSN$ and $3^\circ \leq K_p \leq 4^\circ$ .	76
54	Continuation of comparison in Figure 52. ....	77
55	Comparison of WBMOD Version 12.02 (heavy dashed line) and SCINT- MOD Version 1.0 (heavy solid line) to composite observations of $\log(C_k L)$ (light solid line) for all $SSN$ and $4^\circ \leq K_p \leq 5^\circ$ .	78
56	Continuation of comparison in Figure 55. ....	79
57	Comparison of WBMOD Version 12.02 (heavy dashed line) and SCINT- MOD Version 1.0 (heavy solid line) to composite observations of $\log(C_k L)$ (light solid line) for all $SSN$ and $K_p \geq 5^\circ$ .	80
58	Continuation of comparison in Figure 57. ....	80

## Tables

1	Data available for use in the high-latitude model upgrade. ....	2
2	Definition of the coefficients for the new high-latitude model. ....	11
3	Values of the coefficients for the new high-latitude model. ....	16
4	Results of fitting seasonal variation curves. ....	23
5	Values of the coefficients for the seasonal variation. ....	32

## PREFACE

This report summarizes the work completed during the third year of a project focused on improving the WBMOD model of ionospheric scintillation. This work is part of a larger effort which has the overall objective of providing the USAF Air Weather Service with an improved capability for providing support to their customers who are impacted by ionospheric scintillation effects.

We would like to thank Dr. Santimay Basu of the USAF Phillips Laboratory (PL/GPIA) for his guidance and suggestions for improving the model, Dr. Fred Rich (PL/GPSG) for providing the DMSP SSJ/4 particle boundary data, and Dr. Ed Fremouw (NWRA) for many useful suggestions and numerous discussions over the course of this work.

**THIS PAGE INTENTIONALLY LEFT BLANK**

## 1. Introduction

Many modern military systems used for communications, command and control, navigation, and surveillance depend on reliable and relatively noise-free transmission of radiowave signals through the earth's ionosphere. Small-scale irregularities in the ionospheric density can cause severe distortion, known as radiowave scintillation, of both the amplitude and phase of these signals. A basic tool used in estimating these effects on systems is a computer program, WBMOD, based on a single-scatter phase-screen propagation model and a number of empirical models of the global morphology of ionospheric density irregularities. A recent validation of the WBMOD model showed that it was deficient in a number of areas. Much of this deficiency could be traced to the limited coverage of the data used in developing the model (a single station at high latitudes and two stations at equatorial latitudes). The objective of this study is to investigate and implement improvements to the WBMOD model based on more extensive data sets in both the equatorial and high-latitude regimes.

During the first two years of the study, the equatorial section of the  $\log(C_k L)$  model in WBMOD was upgraded using data sets collected under the auspices of the Directorate of Geophysics of the USAF Phillips Laboratory (PL) [Secan *et al.*, 1993; Secan and Bussey, 1993]. This report summarizes the upgrade to the high-latitude section of the WBMOD  $\log(C_k L)$  model.

## 2. A Brief History of WBMOD

This document marks the passing of the name WBMOD for this model. The name was appropriate when it was first coined in the early 1980s (denoting the WideBand MODel) as the model was largely based on analysis of data from the Defense Nuclear Agency (DNA) Wideband satellite experiment [Fremouw *et al.*, 1978]. With inclusion of data from the subsequent DNA HiLat and Polar BEAR satellites [Fremouw *et al.*, 1985; Fremouw, 1986] and from the Phillips Laboratory equatorial scintillation network [Secan *et al.*, 1993], the name WBMOD no longer holds any significance. We are retaining the name for one final version, which will be denoted WBMOD Version 13, as it is our plan to develop a completely new user interface for the model as part of a new computer code which will be named SCINTMOD.

As a matter of historical record, the full lineage of SCINTMOD begins with the BPMOD code developed at SRI International in the early 1970s [de la Beaujardiere and McNeil, 1971; Fremouw and Rino, 1973]. This model was based on a propagation theory from Briggs and Parkin [1963] and a global model of  $\langle \Delta N_e \rangle$  (RMS  $\Delta N_e$ ) derived from analysis of scintillation data published in the open literature [Fremouw and Bates, 1971]. The successor to BPMOD was a model called IONSCNT [Rino *et al.*, 1977; Fremouw and Rino, 1978] which replaced the propagation model with a new phase-screen propagation theory [Rino and Fremouw, 1977] and retained the BPMOD model for  $\langle \Delta N_e \rangle$ . The first version of WBMOD was developed in the early 1980s [Fremouw and Lansinger, 1981], which replaced the propagation model in IONSCNT with the completed phase-screen theory as described in Rino [1977] and replaced

the  $\langle \Delta N_e \rangle$  model with a model of the path-integrated irregularity strength. The WBMOD model has passed through many upgrades and improvements, culminating in the model described in this document and in *Secan and Bussey, [1993]*.

### 3. High-Latitude Model Development

With completion of the equatorial region of the model, attention has been moved to upgrading the high-latitude region. A very different set of data will be used in this part of the model-upgrade effort from that used in the equatorial upgrade. As with the equatorial database, one of the components of the high-latitude database is a set of data taken from the WIDEBAND satellite experiment, collected at Poker Flat, Alaska. The remaining data were collected from the HiLat and Polar BEAR satellites from four ground stations: Bellevue, Washington; Tromso, Norway; Ft. Churchill, Canada; and Sondre Stromfjord, Greenland. Table lists information about each of these five data sets. The column labeled IPP in this table is the geomagnetic (apex) latitude at the 350-km ionospheric penetration point, and is the average for each data set.

Table 1: Data available for use in the high-latitude model upgrade.

Ground Station	Satellite	IPP	Dates	Points
Bellevue	HiLat/PB	54.1°	1984-1987	86,240
Poker Flat	WIDEBAND	65.9°	1976-1979	61,340
Tromso	HiLat/PB	67.1°	1984-1987	512,490
Ft. Churchill	HiLat/PB	69.7°	1984-1988	317,090
Sondre Stromfjord	HiLat/PB	74.0°	1984-1988	696,020

Data types —

$S_4$  : Intensity scintillation index (RMS)  
 $\sigma_\phi$  : Phase scintillation index (RMS)  
 $T$  : Phase PDS spectral strength (1Hz)  
 $p$  : Phase PDS spectral slope

The basic parameter from this database used in the modeling described in this document is  $C_k L$  calculated from the slope (p) and spectral strength (T) parameters derived from the phase power-density spectrum (PDS). The method used to calculate  $C_k L$  from T and p was described in Section 3.2 of *Secan and Bussey, [1993]*.

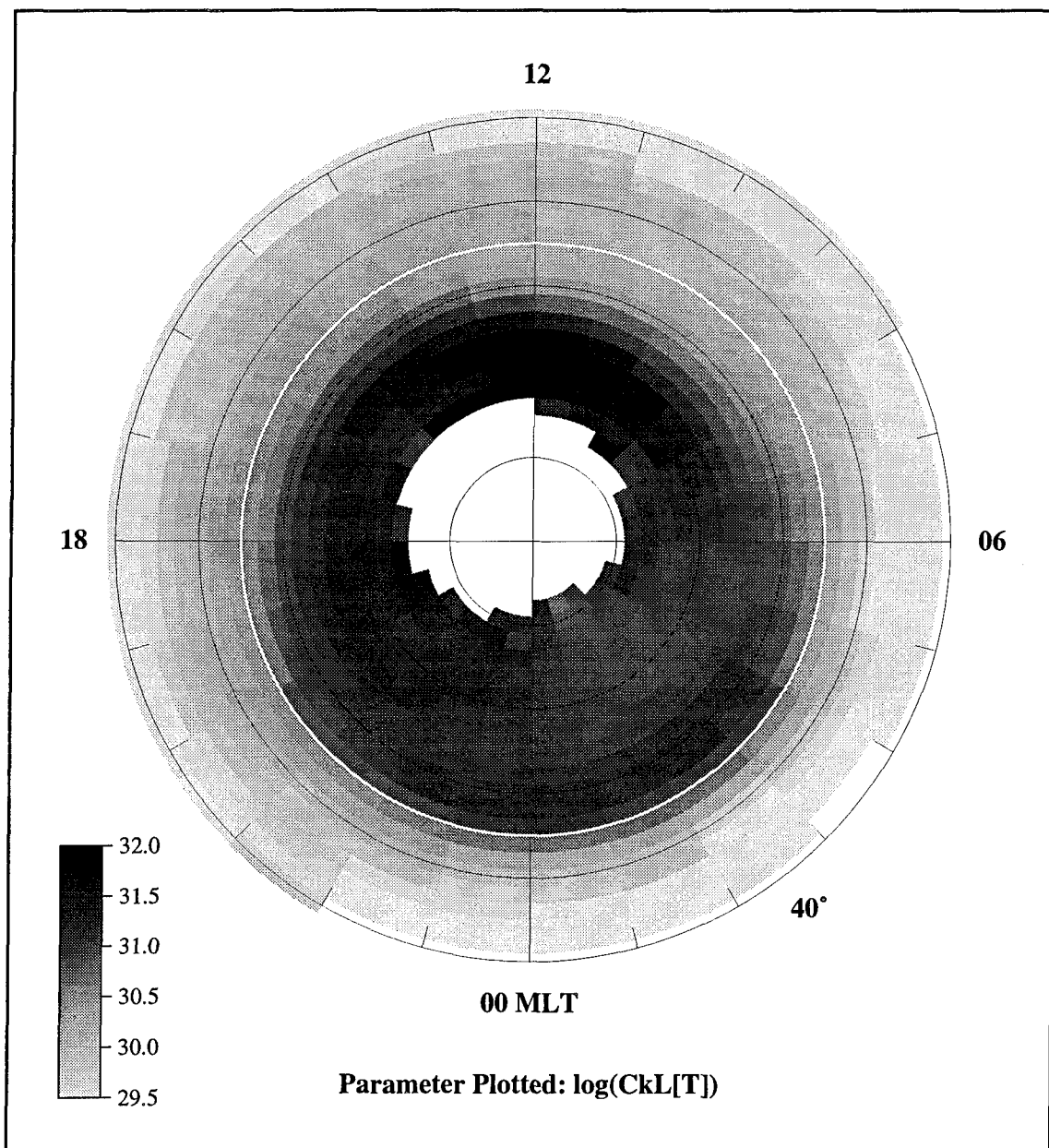
**3.1 Modeling Philosophy.** We were able to use a somewhat simpler approach to modeling at high latitudes than that used for the equatorial modeling [*Secan et al.*, 1993; *Secan and Bussey*, 1993] because the distribution of  $\log(C_k L)$  in the high-latitude region is very nearly gaussian. This permits us to model the average  $\log(C_k L)$  (the PDF parameter  $\mu$ ) and the half-width of the distribution of  $\log(C_k L)$  ( $\sigma$ ) independent of one another. In addition, we have access to the full  $\log(C_k L)$  PDF since we are using  $T$  and  $p$  to derive  $C_k L$ , whereas in the equatorial modeling we used  $SI(dB)$  and  $S_4$  to derive  $C_k L$ , both of which lead to distortions of the high end of the  $\log(C_k L)$  distribution due to Fresnel filtering. Thus our approach to the high-latitude modeling is to develop a model for the average  $\log(C_k L)$  to provide the  $\mu$  PDF parameter, and then develop a second model for  $\sigma$ .

**3.2 Variation with Geophysical Conditions.** The first stage in the  $\log(C_k L)$  modeling was to (1) establish the over-all framework of the high-latitude  $\log(C_k L)$  model, (2) define the features to be included in this model, and (3) determine the variation of these features with local time and with variations in geophysical conditions. The initial plan was to address these items separately, but it became obvious early on that the complexity of the high-latitude behavior would require us to deal with all of these aspects in concert rather than as independent problems. In general, we moved through the three phases of this stage outlined at the start of this paragraph in a linear fashion, but there was some “doubling back” as we found aspects of the framework that were inadequate or additional features that needed to be added.

The first decision concerning the framework of the model was that of the coordinate “space” in which the model would be defined. As described in *Secan and Bussey* [1993], the spatial coordinate system is the distance in geomagnetic latitude from the equatorward boundary of auroral electron precipitation ( $\Lambda$ ) and geomagnetic local time ( $\tau$ ). The location of the equatorward boundary of auroral precipitation is calculated from a model of that location based on analysis of data from the DMSP SSJ sensors [*Gussenhoven et al.*, 1983]. This model can use either an observed boundary location or the three-hour  $K_p$  index from which the location of the boundary at all geomagnetic local times is produced. We found early on that this latitude coordinate ordered the scintillation observations well, and subsequent model development has supported this finding.

The next decision, or set of decisions, was the definition of features (boundaries, peaks, depressions, etc.) to be included in the new high-latitude model. Our decisions were based initially on visual inspection of the data, decisions that were revisited and modified several times during the modeling process. Figures 1, 2, and 3 illustrate the types of displays of this large data set that were used in this definition stage and in later modeling work. Figure 1 is a gray-shade plot of bin-averaged  $\log(C_k L)$  as a function of  $\Lambda$  (radial axis) and  $\tau$  (azimuthal axis) from all HiLat/Polar BEAR stations for all  $SSN$  and all  $K_p$  values. The location of the precipitation boundary on this plot ( $\Lambda = 0$ ) is indicated by the solid white circle. Figures 2 and 3 show these same data, with bin-averaged  $\log(C_k L)$  plotted as a function of  $\Lambda$  for six geomagnetic local time (GMLT) periods.

### Composite -- All Kp / All SSN



Latitude axis:  $55 + (\text{GMLAT-BNDLAT})$   
Range: 40.0 to 90.0  
Step size: 2.00

Time axis: Apex Local Time  
Step size: 1.00

Figure 1: Composite shade plot of  $\log(C_k L)$  for all  $SSN$  and all  $K_p$ . The radial axis is the latitude distance from the  $SSJ/4$  precipitation boundary (solid white line) and the azimuthal coordinate is geomagnetic (apex) local time. The solid white circle indicates the zero point for the radial axis (*i.e.*, the  $SSJ/4$  boundary).

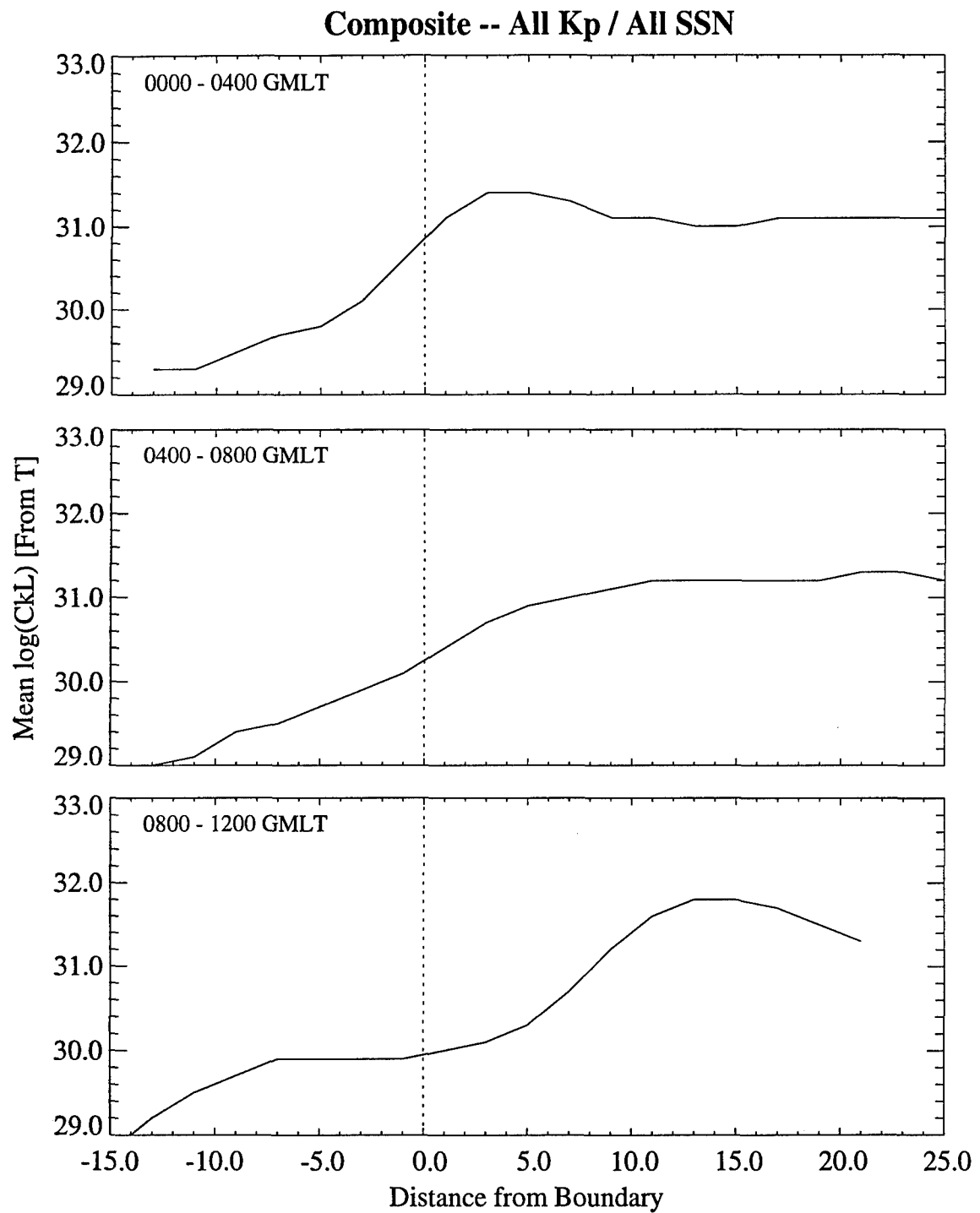


Figure 2: Variation of  $\log(C_k L)$  with the latitude distance from the SSJ/4 precipitation boundary for six geomagnetic (apex) local time ranges. Data are from all HiLat/Polar BEAR stations for all  $SSN$  and all  $K_p$ .

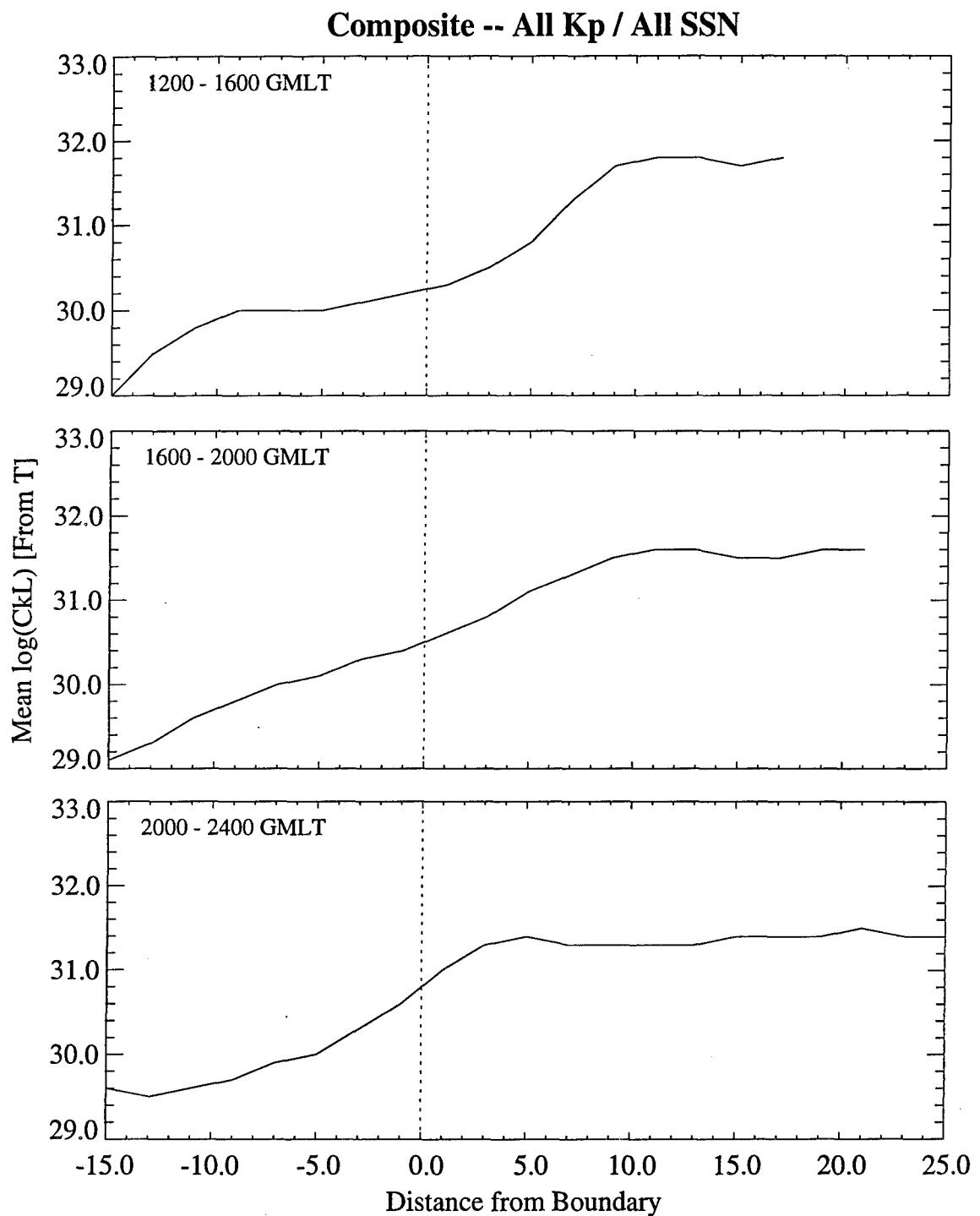


Figure 3: Continuation of comparison in Figure 2.

[Note: This and all other gray-shade plots shown in this document are somewhat poor substitutes for the corresponding color plots actually used in the modeling effort. Some effort was made to find a good gray-shade range that would highlight features in these plots as clearly as they are in a color plot, but many features that are very prominent in color plots do not stand out as well in these gray-shade plots.]

In reviewing these figures (and as a result of iterations during the modeling that followed), the following features were identified and included in the new high-latitude  $\log(C_k L)$  model:

- A high-latitude boundary across which  $C_k L$  changes by over an order of magnitude. This boundary is poleward of the precipitation boundary by a distance that is markedly larger on the day side than on the night side.
- Enhancements in  $C_k L$  along the top of this boundary near the midnight and noon sectors. (This latitude band in which the enhancements occur is somewhat loosely denoted the “auroral” region in later discussions. While it is clearly within the auroral precipitation region in the midnight sector, it is significantly poleward of such precipitation in the noon sector.)
- High levels of  $C_k L$  in the noon-to-dusk sector of the polar-cap region.
- A depression in  $C_k L$  in the midnight-to-dawn sector of the polar-cap region. (This feature is denoted the polar cap “hole” in later discussions.)
- A transition region equatorward of the sharp transition into the auroral region where the  $C_k L$  levels are elevated above typical mid-latitude values for  $C_k L$ . This region is very evident in the 0800 to 1200 GMLT sector in Figure 2 and the 1200 to 1600 GMLT sector in Figure 3. (This feature is denoted the sub-auroral, or SA region, in later discussions.)

After several iterations through the process of determining the values for model coefficients (described later), a set of model equations was constructed that reproduce the variations and patterns found in the data. The basic equation for calculating  $\log(C_k L)$  in the high-latitude region is

$$\log(C_k L) = C_0 + (C_A - C_0) \exp \left[ - \left( \frac{\Lambda - \Lambda_A}{W} \right)^2 \right] \quad (1)$$

$$\Lambda = \lambda_m - \lambda_{J4} \quad (2)$$

where  $C_A$  is the value of  $\log(C_k L)$  at the center of the auroral enhancement region;  $C_0$  is the value of  $\log(C_k L)$  either in the polar cap region (if  $\Lambda$  is poleward of the center of the auroral

enhancement region,  $\Lambda_A$ ) or in the sub-auroral (SA) region (if  $\Lambda$  is equatorward of  $\Lambda_A$ );  $\lambda_m$  is the geomagnetic latitude; and  $\lambda_{J4}$  is the geomagnetic latitude of the equatorward boundary of auroral precipitation as specified by the DMSP SSJ/4 model either from observations of the boundary location or from  $K_p$ . The center latitude of the auroral enhancement region is given by

$$\Lambda_A = \left[ \frac{\Lambda_{A,N} + \Lambda_{A,D}}{2} \right] + \left[ \frac{\Lambda_{A,N} - \Lambda_{A,D}}{2} \right] \cos(\tau - \tau_A) \quad (3)$$

where  $\tau_A$  is defined as the time on the nightside where the boundary reaches its maximum equatorward extent.

The  $C_0$  and  $W$  parameters in Eq. (1) are calculated as follows:

For  $\Lambda < \Lambda_A$

$$C_0 = C_M + \frac{\Delta C_{SA}}{2} \left[ 1 + \operatorname{erf} \left( \frac{\Lambda - \Lambda_{SA}}{W_{SA}} \right) \right] \quad (4)$$

and

$$W = \left[ \frac{W_{A,SA,D} + W_{A,SA,N}}{2} \right] + \left[ \frac{W_{A,SA,D} - W_{A,SA,N}}{2} \right] \cos(\tau - \tau_A) \quad (5)$$

where  $C_M$  is the mid-latitude  $\log(C_k L)$  given by

$$C_M = C_{M,0} + \Delta C_{M,R} R + \Delta C_{M,\tau} \cos(\tau) \quad (6)$$

where  $R \equiv SSN/100$  and  $\tau$  is the geomagnetic local time,  $\Delta C_{SA}$  is the difference between the mid-latitude  $\log(C_k L)$  and  $\log(C_k L)$  in the sub-auroral region, given by

$$\Delta C_{SA} = \Delta C_{SA,0} + \Delta C_{SA,\tau} \cos(\tau - \tau_{SA}) \quad , \quad (7)$$

and  $\Lambda_{SA}$  is the latitude at the center of the transition from the mid-latitude to the sub-auroral regions given by

$$\Lambda_{SA} = \left[ \frac{\Lambda_{SA,D} + \Lambda_{SA,N}}{2} \right] + \left[ \frac{\Lambda_{SA,D} - \Lambda_{SA,N}}{2} \right] \cos(\tau - \tau_{SA}) \quad (8)$$

where  $\tau_{SA}$  is defined as the time on the dayside where the boundary reaches its maximum equatorward extent.

Initially, model parameters derived in an earlier effort [Robins *et al.*, 1986] were used in the mid-latitude model [Eq. (6)]. In deriving the parameters for the high-latitude model, however, we found that we needed to adjust these parameters in order to obtain the best fit to the observations. This is discussed further in the next section.

For  $\Lambda \geq \Lambda_A$

$$C_0 = C_{PC} \quad (9)$$

and

$$W = \left[ \frac{W_{A,PC,D} + W_{A,PC,N}}{2} \right] + \left[ \frac{W_{A,PC,D} - W_{A,PC,N}}{2} \right] \cos(\tau - \tau_A) \quad (10)$$

The value of  $\log(C_k L)$  at the center of the auroral enhancement region,  $C_A$ , is calculated as an offset from the  $\log(C_k L)$  value in the polar cap region, or

$$C_A = C_{PC} + \Delta C_A \quad (11)$$

where

$$C_{PC} = C_{PC,0} + \Delta C_{PC,H} \times G(\tau, \tau_{PC,H}, W_{PC,H}^-, W_{PC,H}^+) \times F(\lambda, \lambda_{PC,H}) \quad , \quad (12)$$

and

$$\begin{aligned} \Delta C_A = & \Delta C_{A,0} + \Delta C_{A,D} \times G(\tau, \tau_{A,D}, \Delta \tau_{A,D}, W_{A,D}^-, W_{A,D}^+) \\ & + \Delta C_{A,N} \times G(\tau, \tau_{A,N}, \Delta \tau_{A,N}, W_{A,N}^-, W_{A,N}^+) \quad . \end{aligned} \quad (13)$$

The two functions  $F$  and  $G$  in Eq. (12) and Eq. (13) are given by

$$F(X, X_0) = \begin{cases} \exp \left[ - \left( \frac{X - X_0}{W_F} \right)^2 \right] & \text{if } X > X_0 \\ 1.0 & \text{if } X \leq X_0 \end{cases} \quad (14)$$

$$W_F = (90 - X_0) \sqrt{(-\ln |\delta|)} \quad (15)$$

where  $\delta$  is set to 0.001, and

$$G(\tau, \tau_0, \Delta\tau, W^-, W^+) = \begin{cases} 1.0 & \tau \text{ within } \pm \frac{\Delta\tau}{2} \text{ of } \tau_0 \\ \exp\left[-\left(\frac{X^+}{W^+}\right)^2\right] + \exp\left[-\left(\frac{X^-}{W^-}\right)^2\right] & \text{otherwise} \end{cases} \quad (16)$$

where

$$X^+ = (\tau - \tau_0) - \frac{\Delta\tau}{2} \quad (17)$$

$$X^- = (\tau - \tau_0) + \frac{\Delta\tau}{2} \quad (18)$$

This set of equations then defines the new high-latitude  $\log(C_k L)$  model. It includes 29 model coefficients, which are listed in Table . The next step in the modeling process was to establish values for these parameters, and to determine which of them varied as functions of either  $SSN$  or  $K_p$ .

The method used to determine the values for the model coefficients is similar to that used in the Ionospheric Scintillation Analysis Model (program IONSAM) developed for the USAF Space Forecast Center [Secan *et al.*, 1990]. The model is treated as a complex function that is to be fitted to a set of data by adjusting all or some subset of the model coefficients. In the IONSAM program, the Levenberg-Marquardt method was used to fit the high-latitude model to  $C_k L$  data sets derived from ground-based scintillation observations and *in situ* density measurements from the DMSP satellite. Due to the greater complexity of the new high-latitude model, it was decided to use a somewhat simpler method for fitting the model to the observations. In particular, a method that did not require matrix inversion was desired due to the much larger number of model coefficients (a number that increased from 29 to 51 when variations with  $SSN$  and  $K_p$  were added to the model). The method selected was a simple gradient search method as described in Chapter 11 of Bevington [1969] (see the discussion of program GRADLS on pages 215-222). This method was implemented in such a way that any of the model parameters could be adjusted in the fitting process.

In order to speed up the process of determining the model coefficients, the fitting procedure used several sets of bin-averaged  $\log(C_k L)$  values rather than “raw”  $\log(C_k L)$  values directly from the four station databases. A total of thirteen data sets were generated: one that included data for all  $SSN$  and all  $K_p$  (shown in Figures 1 through 3), six for all  $K_p$  for

Table 2: Definition of the coefficients for the new high-latitude model.

Symbol	Description
$C_{PC,0}$	$\log(C_k L)$ in polar cap region (base term)
$\Delta C_{PC,H}$	Depth of polar-cap “hole”
$\tau_{PC,H}$	MLT of the center of the polar-cap “hole”
$\Delta\tau_{PC,H}$	MLT width of polar-cap “hole”
$W_{PC,H}^-$	MLT half-width of polar-cap “hole” (-)
$W_{PC,H}^+$	MLT half-width of polar-cap “hole” (+)
$\lambda_{PC,H}$	Poleward boundary of polar-cap “hole”
$\Delta C_{A,0}$	$\Delta\log(C_k L)$ at the auroral boundary
$\Delta C_{A,D}$	$\Delta\log(C_k L)$ at dayside maximum
$\Delta\tau_{A,D}$	Width of dayside maximum
$\tau_{A,D}$	MLT of dayside maximum
$W_{A,D}^-$	MLT half-width of dayside maximum (-)
$W_{A,D}^+$	MLT half-width of dayside maximum (+)
$\Delta C_{A,N}$	$\Delta\log(C_k L)$ at nightside maximum
$\Delta\tau_{A,N}$	Width of nightside maximum
$\tau_{A,N}$	MLT of nightside maximum
$W_{A,N}^-$	MLT half-width of nightside maximum (-)
$W_{A,N}^+$	MLT half-width of nightside maximum (+)
$\Lambda_{A,D}$	Dayside extent of the auroral boundary
$\Lambda_{A,N}$	Nightside extent of the auroral boundary
$\tau_A$	MLT of maximum nighttime extent
$W_{A,SA,N}$	Half-width of SA $\rightarrow$ A transition (nightside)
$W_{A,SA,D}$	Half-width of SA $\rightarrow$ A transition (dayside)
$W_{A,PC,N}$	Half-width of A $\rightarrow$ PC transition (nightside)
$W_{A,PC,D}$	Half-width of A $\rightarrow$ PC transition (dayside)
$\Delta C_{SA,0}$	$\Delta\log(C_k L)$ in the SA region
$\Delta C_{SA,\tau}$	Diurnal variation of $\log(C_k L)$ in the SA region
$\Lambda_{SA,N}$	Nightside extent of the SA region
$\Lambda_{SA,D}$	Dayside extent of the SA region
$\tau_{SA}$	MLT of maximum dayside extent
$W_{SA}$	Half-width of SA transition

six ranges of  $SSN$ , and six for all  $SSN$  for six ranges of  $K_p$ . Grey-shade plots for these data sets are included in Appendix A. The  $\log(C_k L)$  values in these data sets were the average  $\log(C_k L)$  from all four stations in  $\Lambda-\tau$  bins that were  $2^\circ$  wide in latitude by 30 minutes wide in time. Similar binned data sets of  $SSN$  and  $K_p$  were generated for each case for use in determining variations with  $SSN$  and  $K_p$ .

Initial values for the 30 model coefficients were established first by inspection of the all- $SSN$ /all- $K_p$  case, then by fitting the model to this case with all model parameters included in the analysis. Figures 4 and 5 show the results of this initial fit in format similar to that used in Figures 2 and 3. In these figures, the heavy solid curve is the result of the fitting procedure, and the heavy dashed curve shows the variation of  $\log(C_k L)$  from the current WBMOD high-latitude model. The two model curves are not as smooth as one would expect from the smooth functions they are based on due to the fact that the bin-averaged  $SSN$  and  $K_p$  values valid at each data point were used in the models rather than values averaged over the entire set.

With the base values established for the model coefficients, the next step was to ascertain which of the coefficients would vary with geophysical conditions and to establish relationships between these coefficients and the appropriate geophysical indices. We first addressed the issue of variation with  $SSN$ . The fitting procedure was executed on each of the six data sets constructed for various ranges of  $SSN$  with all of the 30 coefficients included in the fitting procedure. The variation of each of the coefficients as a function of  $SSN$  was examined, and those that showed no clear definable variation with  $SSN$  were set to average values and excluded from future adjustment. The fits were performed again, and the variation of the remaining non-fixed coefficients were examined. After several iterations, we settled on 4 of the 30 coefficients that clearly (and in a simple fashion) varied with  $SSN$ :  $C_{PC,0}$  and  $\tau_{A,D}$  varied linearly with  $SSN$ ; and  $\Delta C_{A,0}$  and  $\Delta C_{SA,0}$  varied as  $SSN^2$ . [Note: The model actually uses a parameter  $R \equiv SSN/100$  for the  $SSN$ .]

With an initial model for the variation with  $SSN$  established, the same procedure was executed using the six data sets constructed for various ranges of  $K_p$ . In this analysis, we found that 12 of the 30 coefficients varied with  $K_p$ :  $\Delta C_{PC,H}$ ,  $\Delta C_{A,0}$ ,  $\Delta C_{SA}$ ,  $\tau_{PC,H}$ ,  $\tau_{A,N}$ ,  $\Lambda_{A,D}$ ,  $\Lambda_{A,N}$ ,  $\Lambda_{SA,D}$ ,  $W_{A,SA,N}$ , and  $W_{A,SA,D}$  varied linearly with  $K_p$ ; and  $C_{PC,0}$ ,  $\Delta C_{A,N}$ , and  $\Delta C_{A,D}$  varied as  $K_p^2$ .

[Note: Care was taken in establishing the functional forms of the variation of model coefficients with  $SSN$  and  $K_p$ . In all cases where the variation is quadratic, the coefficient to the linear term is opposite that of the coefficient to the quadratic term. Thus, in all of these cases, there is a saturation effect in that there is a threshold  $SSN$  (or  $K_p$ ), defined by the minimum or maximum of the curve, above or below which the coefficient is “frozen” at the value obtained at the threshold  $SSN$  (or  $K_p$ ). This precludes the model from “running wild” for abnormally high values of either geophysical parameter.]

The final step in this process was to fit the model simultaneously to both the  $SSN$ -

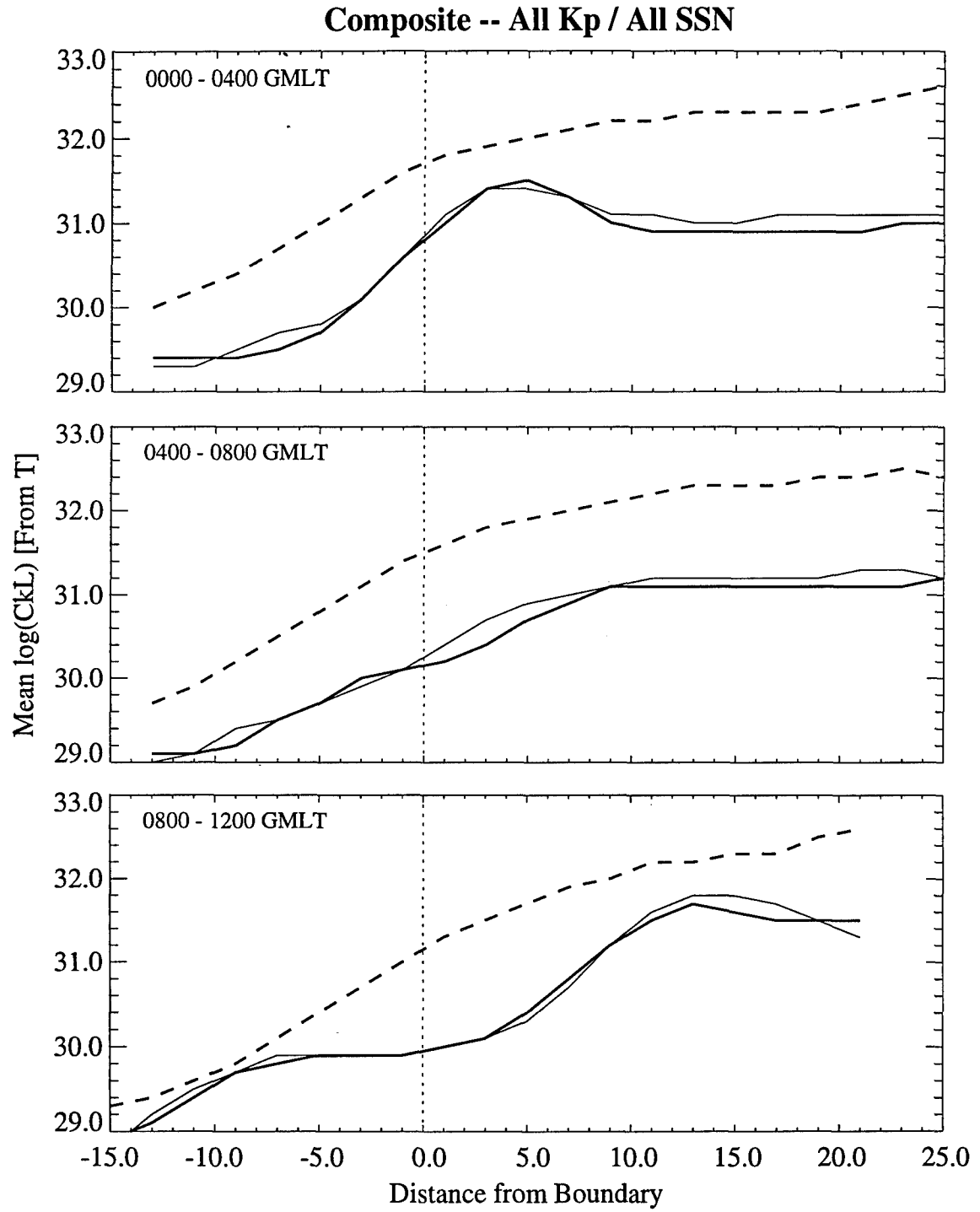


Figure 4: Variation of  $\log(C_{kL})$  with the latitude distance from the SSJ/4 precipitation boundary for six geomagnetic (apex) local time ranges for all SSN and all  $K_p$ . The light solid curve indicates the observations, the heavy solid curve the new high-latitude model, and the heavy dashed curve the current WBMOD high-latitude model.

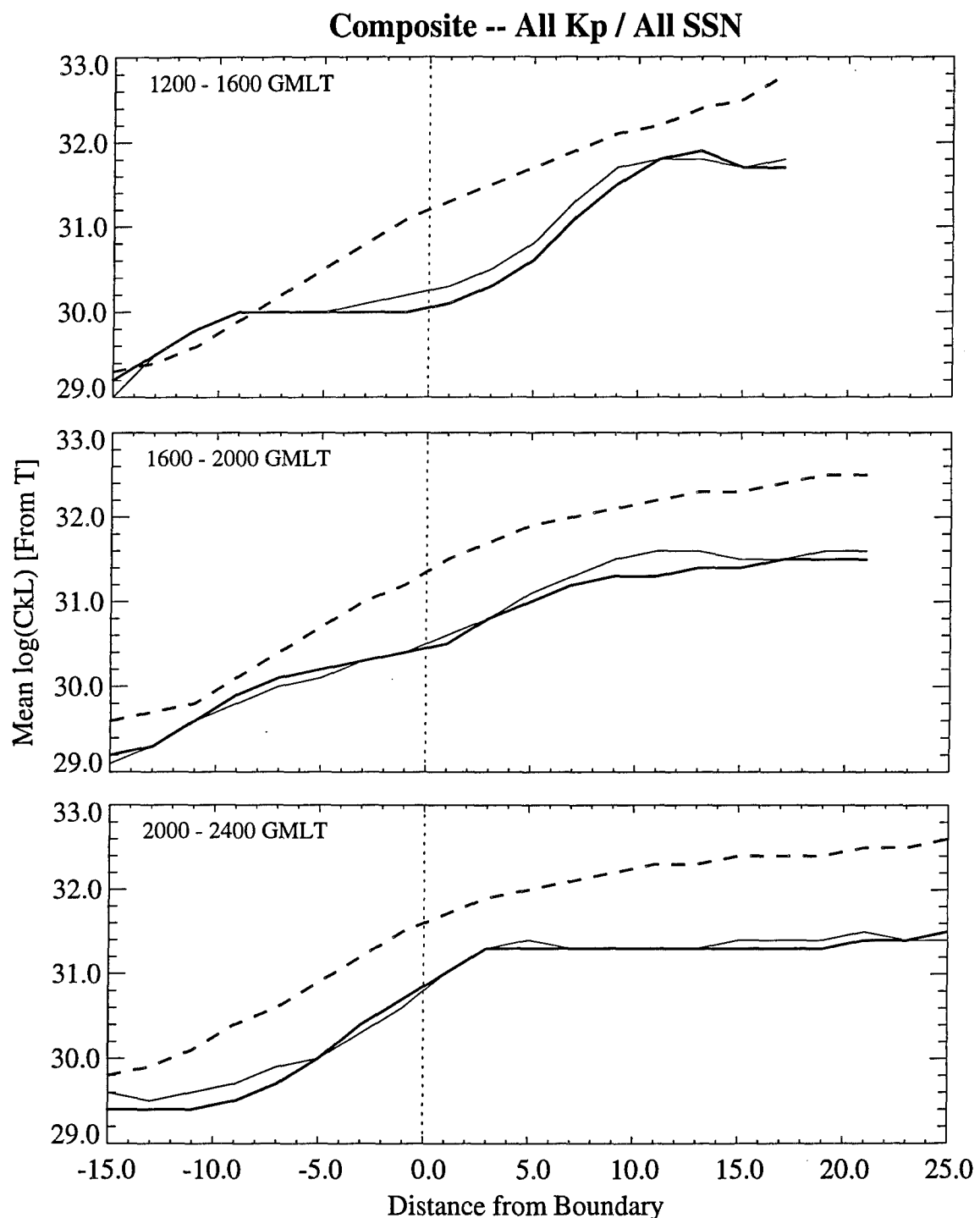


Figure 5: Continuation of comparison in Figure 4.

invariant data sets and the  $K_p$ -invariant data sets. All of the bin-averaged  $\log(C_k L)$  (and the corresponding bin-averaged  $SSN$  and  $K_p$ ) from the 12 data sets were passed to the fitting procedure using the same methods described in the last two paragraphs. At this point, the number of model coefficients had increased to 53 by including coefficients to the linear and quadratic variation of some of the model coefficients with  $SSN$  and  $K_p$ . After a number of iterations, it was found that the variation of the  $\Delta C_{PC,H}$  coefficient with  $K_p$  was no longer significant, and this variation was dropped from the model. In the final analysis, the following model coefficients were found to be functions of either  $SSN$ ,  $K_p$ , or both:

$$\begin{aligned} C_{PC,0} &= f(R, K_p, K_p^2) \\ \Delta C_{A,0} &= f(R, R^2, K_p) \\ \Delta C_{A,D} &= f(K_p, K_p^2) \\ \Delta C_{A,N} &= f(K_p, K_p^2) \\ \Delta C_{SA,0} &= f(R, R^2, K_p) \end{aligned}$$

$$\begin{aligned} \tau_{PC,H} &= f(K_p) \\ \tau_{A,D} &= f(R) \\ \tau_{A,N} &= f(K_p) \end{aligned}$$

$$\begin{aligned} \Lambda_{A,D} &= f(K_p) \\ \Lambda_{A,N} &= f(K_p) \\ \Lambda_{SA,D} &= f(K_p) \end{aligned}$$

$$\begin{aligned} W_{A,SA,N} &= f(K_p) \\ W_{A,SA,D} &= f(K_p) \end{aligned}$$

The final values for the 52 model coefficients, including the variations with  $SSN$  and  $K_p$ , are listed in Table . Comparisons of the resulting model and the current WBMOD model with the twelve  $SSN$  and  $K_p$  data sets in the same format as Figures 4 and 5 are presented in Appendix B.

This new model for the behavior of  $C_k L$  at high latitudes is quite a bit more complex than the old model (in WBMOD Version 12), which is not surprising given that the old model was based on analysis of data from a single site (Poker Flat, Alaska) in only two local time sectors (pre-noon and pre-midnight). The variations in local time and with geophysical conditions include the following:

- The sub-auroral (SA) region, which may be associated with effects from the plasma-pause (although without a more in-depth study, this connection must be classified as strictly a supposition), is almost non-existent in the night sector, but extends up to

Table 3: Values of the coefficients for the new high-latitude model.

Value	Symbol	Description
31.32	$C_{PC,0}$	$\log(C_k L)$ in polar cap region (base term)
0.84		Variation with $R$
-0.12		Variation with $K_p$
0.023		Variation with $K_p^2$
-0.50	$\Delta C_{PC,H}$	Depth of polar-cap “hole”
1.80	$\tau_{PC,H}$	MLT of the center of the polar-cap “hole”
0.33		Variation with $K_p$
1.75	$\Delta \tau_{PC,H}$	MLT width of polar-cap “hole”
3.46	$W_{PC,H}^-$	MLT half-width of polar-cap “hole” (-)
3.18	$W_{PC,H}^+$	MLT half-width of polar-cap “hole” (+)
76.69	$\lambda_{PC,H}$	Poleward boundary of polar-cap “hole”
-0.31	$\Delta C_{A,0}$	$\Delta \log(C_k L)$ at the auroral boundary
-0.49		Variation with $R$
0.12		Variation with $R^2$
0.081		Variation with $K_p$
0.91	$\Delta C_{A,D}$	$\Delta \log(C_k L)$ at dayside maximum
0.037		Variation with $K_p$
-0.027		Variation with $K_p^2$
0.31	$\Delta \tau_{A,D}$	MLT width of dayside maximum
12.01	$\tau_{A,D}$	MLT of dayside maximum
0.71		Variation with $R$
3.02	$W_{A,D}^-$	MLT half-width of dayside maximum (-)
3.69	$W_{A,D}^+$	MLT half-width of dayside maximum (+)
0.59	$\Delta C_{A,N}$	$\Delta \log(C_k L)$ at nightside maximum
0.20		Variation with $K_p$
-0.022		Variation with $K_p^2$
1.64	$\Delta \tau_{A,N}$	MLT width of nightside maximum
1.31	$\tau_{A,N}$	MLT of nightside maximum
0.20		Variation with $K_p$
2.91	$W_{A,N}^-$	MLT half-width of nightside maximum (-)
2.69	$W_{A,N}^+$	MLT half-width of nightside maximum (+)

Table 3: Values of the coefficients for the new high-latitude model (continued).

Value	Symbol	Description
13.52	$\Lambda_{A,D}$	Dayside extent of the auroral boundary
-0.025		Variation with $K_p$
2.10		Nightside extent of the auroral boundary
0.94		Variation with $K_p$
23.37		MLT of maximum nighttime extent
5.65		Half-width of SA $\rightarrow$ A transition (nightside)
0.051		Variation with $K_p$
6.01		Half-width of SA $\rightarrow$ A transition (dayside)
0.39		Variation with $K_p$
2.52		Half-width of A $\rightarrow$ PC transition (nightside)
3.19	$W_{A,PC,D}$	Half-width of A $\rightarrow$ PC transition (dayside)
0.52	$\Delta C_{SA}$	$\Delta \log(C_k L)$ in the SA region
0.44		Variation with $R$
-0.11		Variation with $R^2$
0.20		Variation with $K_p$
0.19		Diurnal variation of $\log(C_k L)$ in the SA region
-3.16		Nightside extent of the SA region
-16.72		Dayside extent of the SA region
1.74		Variation with $K_p$
13.69	$\tau_{SA}$	MLT of maximum dayside extent
3.86	$W_{SA}$	Half-width of SA transition

$15^\circ$  equatorward of the precipitation boundary in the post-noon sector. The scintillation level in this region is a function of both  $SSN$  and  $K_p$  (increasing with both), and the boundary on the dayside moves toward the precipitation boundary with increasing  $K_p$ .

- The main scintillation boundary, denoted  $\Lambda_A$  in the model equations, is much farther poleward of the precipitation boundary on the dayside than it is on the nightside, with the peak of the auroral enhancement occurring roughly  $2^\circ$  poleward of the precipitation boundary near midnight and almost  $14^\circ$  near noon. Both the location of the auroral enhancement and the half-width of this feature change with the level of geomagnetic activity ( $K_p$ ), broadening on both the dayside and the nightside and moving farther poleward off the boundary on the nightside and closer to the boundary on the dayside.
- The auroral enhancement region (that latitude band at the “top” of the main increase in  $C_k L$  with latitude) has two distinct maxima: one in the midnight sector and one in the noon sector. Both maxima increase in intensity with increasing  $K_p$ , while the center time of the night peak moves to later local times (starting at 0121 GMLT) with

increasing  $K_p$  and the time of the day peak moves to later times (starting at 1157 GMLT) with increasing  $SSN$ .

- The polar cap region shows a strong enhancement in the post-noon sector, and a depression (or hole) in the post-midnight sector. The overall  $C_kL$  level in the polar cap increases with increasing  $SSN$  and decreases with increasing  $K_p$ . The hole region, which may be associated with lower levels of density and of polar-cap patches due to convection dynamics within the polar cap region, is located at 0148 GMLT and moves to later local times with increasing  $K_p$ . The decrease in  $C_kL$  within the center of this region does not appear to change in a systematic fashion with either  $SSN$  or  $K_p$ , although there is some evidence that the difference between the average  $C_kL$  in the hole region and the average  $C_kL$  in the rest of the polar cap may become smaller with increasing  $K_p$ .

**3.3 Seasonal/Longitudinal Variation.** The present high-latitude model for  $\log(C_kL)$  in WBMOD does not include a seasonal variation, as no seasonal variation was found in the analysis of Wideband data collected at Poker Flat [Fremouw and Lansinger, 1981]. There was, however, strong evidence at other latitude sectors for such a variation, as shown by Basu [1975] and Basu and Aarons [1980] (in particular, see Figure 3 in Basu [1975]), and a number of studies over the past decade have focused on the issue of seasonal and longitudinal (or UT) variations in the polar cap [de la Beaujardiere *et al.*, 1985; Buchau *et al.*, 1985; Sojka *et al.*, 1994]. The next step in this model upgrade was to look for evidence of a seasonal variation in the HiLat/Polar BEAR data set and, if found, develop a model for the variation to be included in the upgrade.

Such a variation was found and it is, for the most part, in agreement with the variations reported by Basu [1975] and Basu and Aarons [1980]. Figures 6 through 9 show the variation of the residual  $\log(C_kL)$ , defined as the observed  $\log(C_kL)$  minus the  $\log(C_kL)$  derived from the model described in the previous section, as a function of the time elapsed since the launch of the HiLat satellite for each of the high-latitude HiLat/Polar BEAR stations for each of four geomagnetic local time (GMLT) sectors. The clearest signals in these figures are the strong seasonal variations at Ft. Churchill in both the midnight and noon sectors, and at Sondre Stromfjord in the noon sector, although there are varying levels of a seasonal variation visible in other stations/time-sectors as well. Note also that the variations at Ft. Churchill in the noon sector are opposite in phase to those in the midnight sector, a phenomenon reported by Basu and Aarons [1980] in their data set from Narssarssuaq, Greenland.

As an initial step toward including these variations in the model, each of the twelve curves shown in Figures 6 through 9 were fit using a multiple regression analysis to an equation of the form

$$\Delta\log(C_kL) = c_0 + c_R \left( \frac{SSN}{100} \right) + c_D \cos(D - D_0) \quad (19)$$

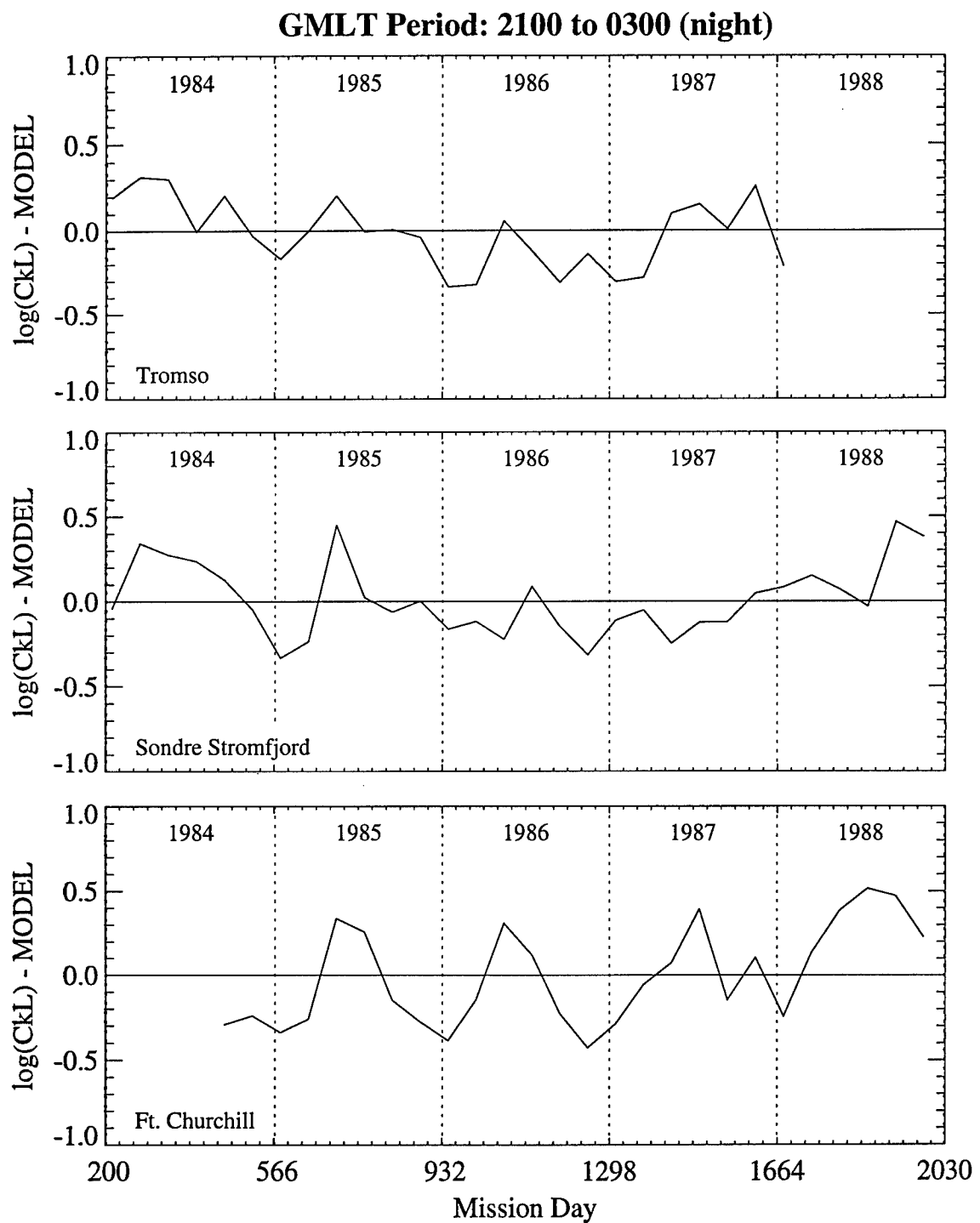


Figure 6: Variation of the residual  $\log(C_k L)$  as a function of days since the launch of HiLat at Tromso (top plot), Sondre Stromfjord (middle plot), and Ft. Churchill (bottom plot) for the night sector (2100 to 0300 GMLT).

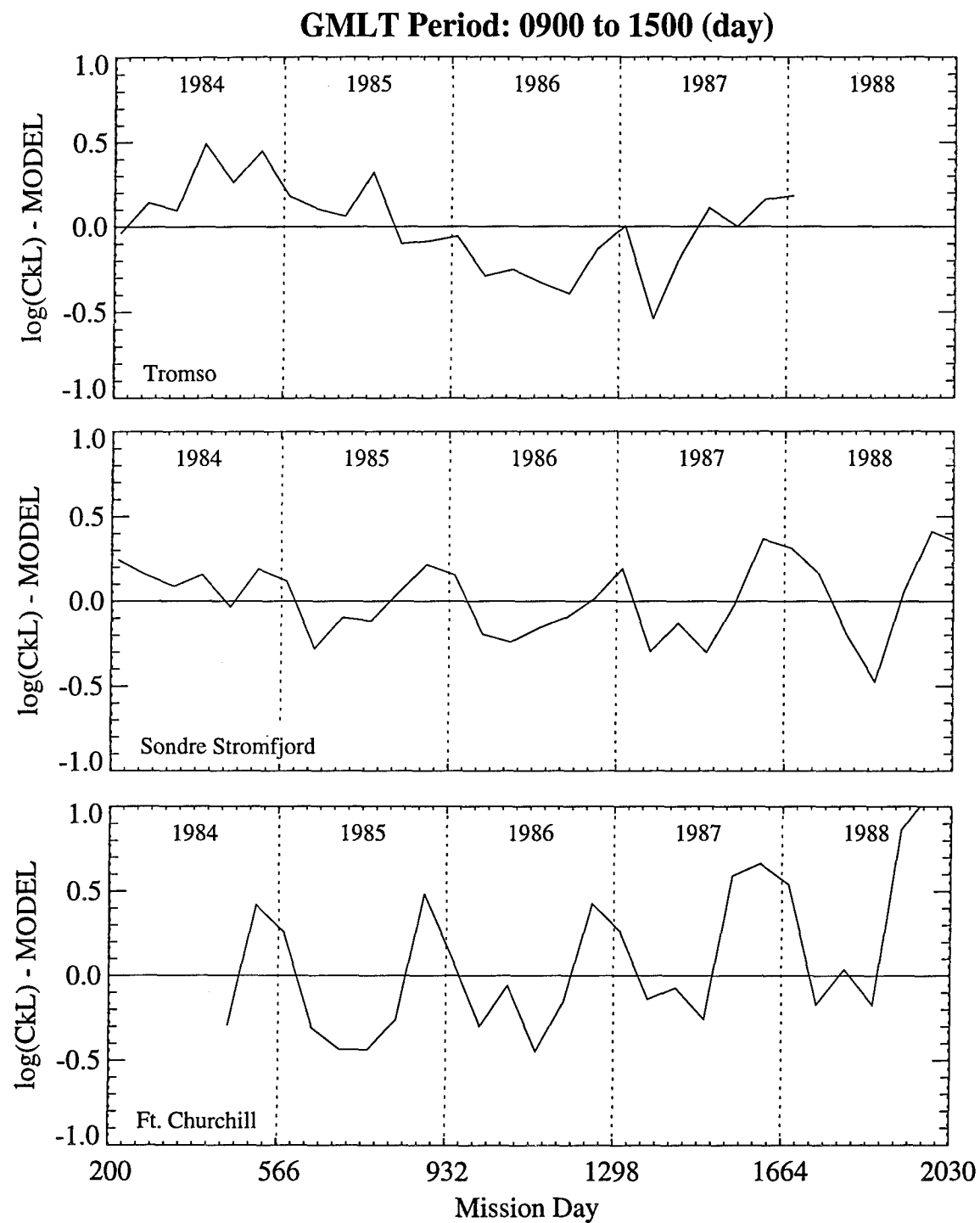


Figure 7: Same as Figure 6 for the noon sector (0900 to 1500 GMLT).

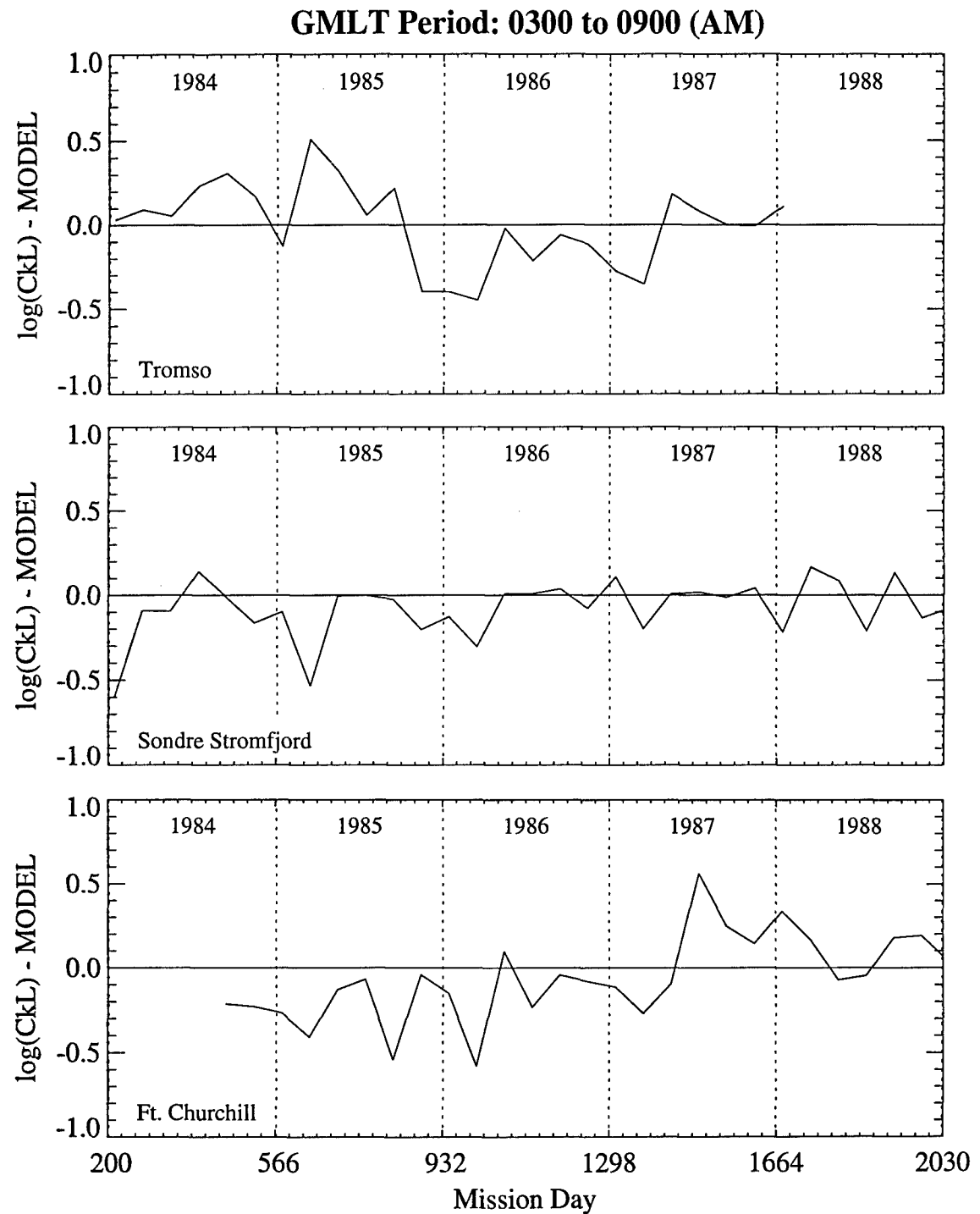


Figure 8: Same as Figure 6 for the morning (AM) sector (0300 to 0900 GMLT).

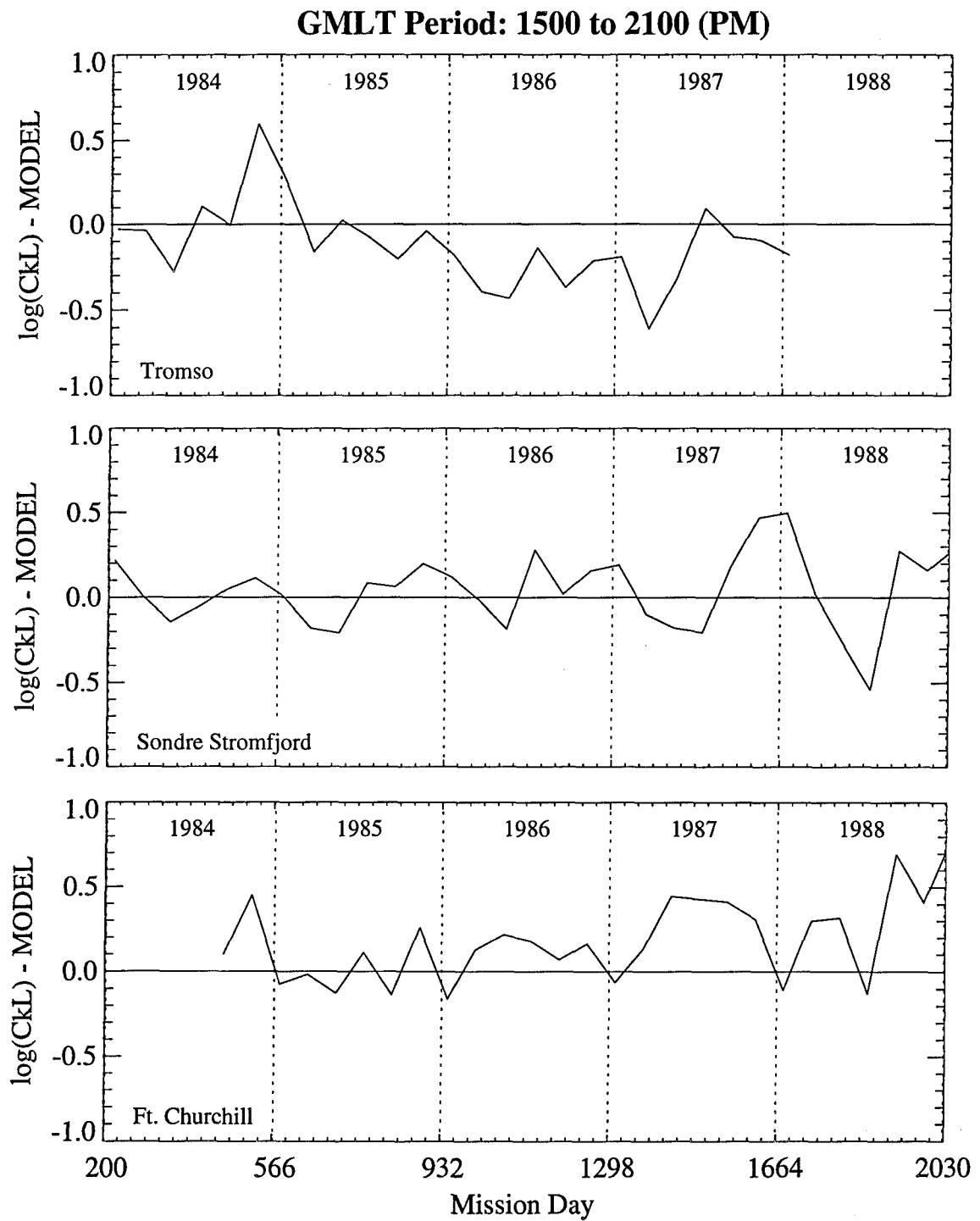


Figure 9: Same as Figure 6 for the evening (PM) sector (1500 to 2100 GMLT).

where  $D$  is the day of the year. The  $SSN$  dependence was included, as it was obvious that at least a few of the stations showed a modulation of the seasonal curve as a function of  $SSN$ . (This  $SSN$ -dependence will be discussed further at the end of this section.) The results of these fits are shown in Figures 10 through 13 (the fits are the dotted curves) and are summarized in Table .

Table 4: Results of fitting seasonal variation curves.

Station	$c_0$	$c_R$	$c_D$	$D_0$	$\chi^2$
Day Sector (0900 to 1500)					
TR	-0.02	0.10	0.08	76.1	1.45
SS	-0.35	0.10	0.22	6.5	0.68
FC	-0.14	0.57	0.43	14.8	1.17
PM Sector (1500 to 2100)					
TR	-0.16	0.16	0.14	61.5	1.15
SS	0.05	-0.02	0.22	20.8	0.72
FC	0.06	0.25	0.05	76.4	1.13
Night Sector (2100 to 0300)					
TR	-0.17	0.57	0.13	161.7	0.57
SS	-0.12	0.31	0.06	167.7	0.97
FC	-0.15	0.45	0.29	183.3	0.45
AM Sector (0300 to 0900)					
TR	-0.09	0.34	0.14	153.2	1.15
SS	-0.07	0.00	0.11	138.6	0.72
FC	-0.12	0.13	0.07	104.7	1.13
$c_0 + c_R \frac{SSN}{100} + c_D \cos(D - D_0)$					

It is apparent from these figures that there is definitely a seasonal variation in high-latitude scintillation and that it is a complex function of local time, longitude sector, and latitude regime. We have chosen to focus on the dominant characteristics rather than attempt to model all of the subtleties of the variations seen in these figures for two reasons. First, two large pieces of the “puzzle” are missing: we have no observations from the Russian longitude sector, and only limited data from the polar cap (Sondre Stromfjord in the night sector). Second, we have found it difficult to reconcile behavior seen at various stations in the same time and longitude sectors within the context of the present modeling effort.

Figure 14 shows the distribution of stations at which data used in this study were col-

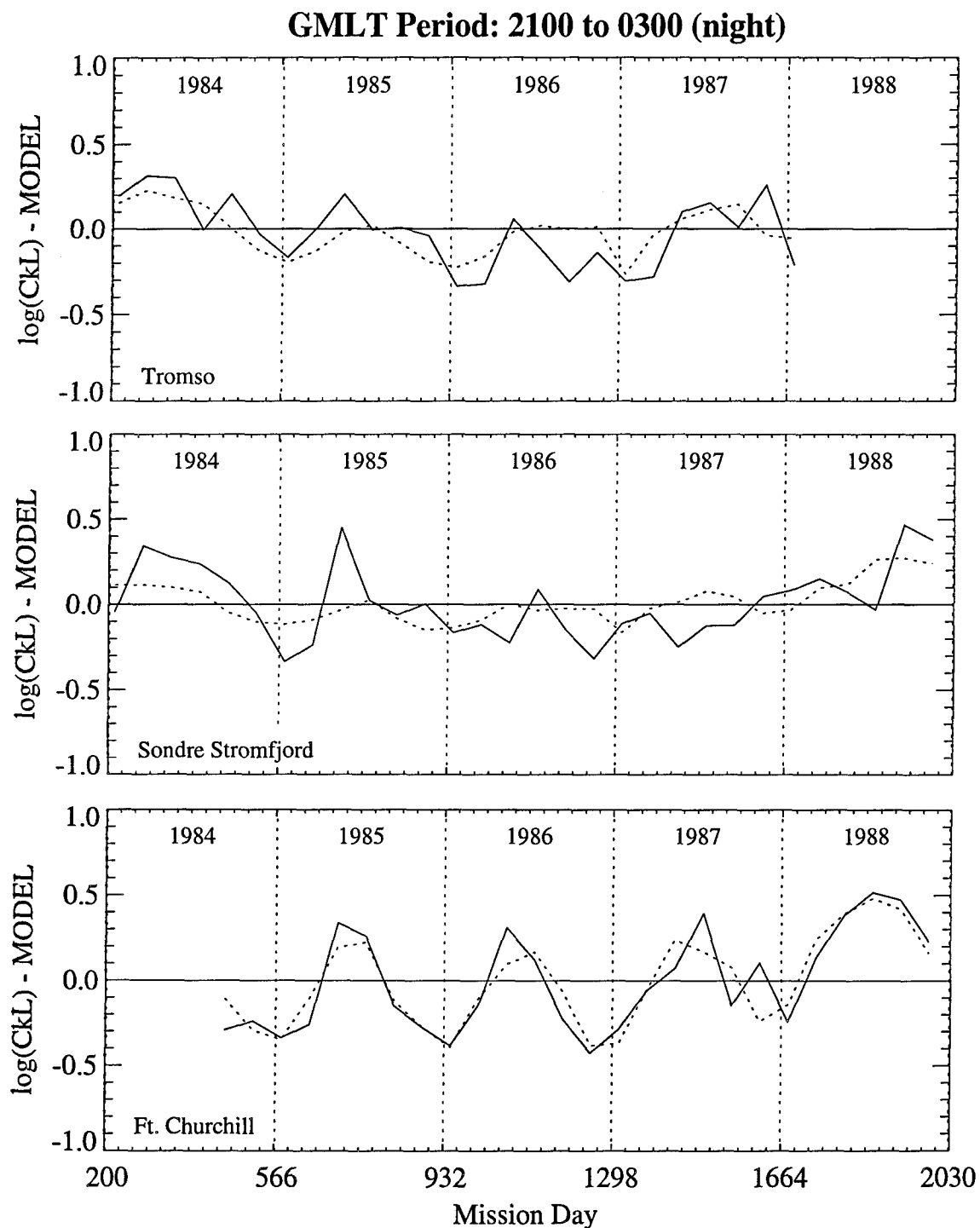


Figure 10: Data from Figure 6 (night sector) with the results of the regression analysis (dotted curve).

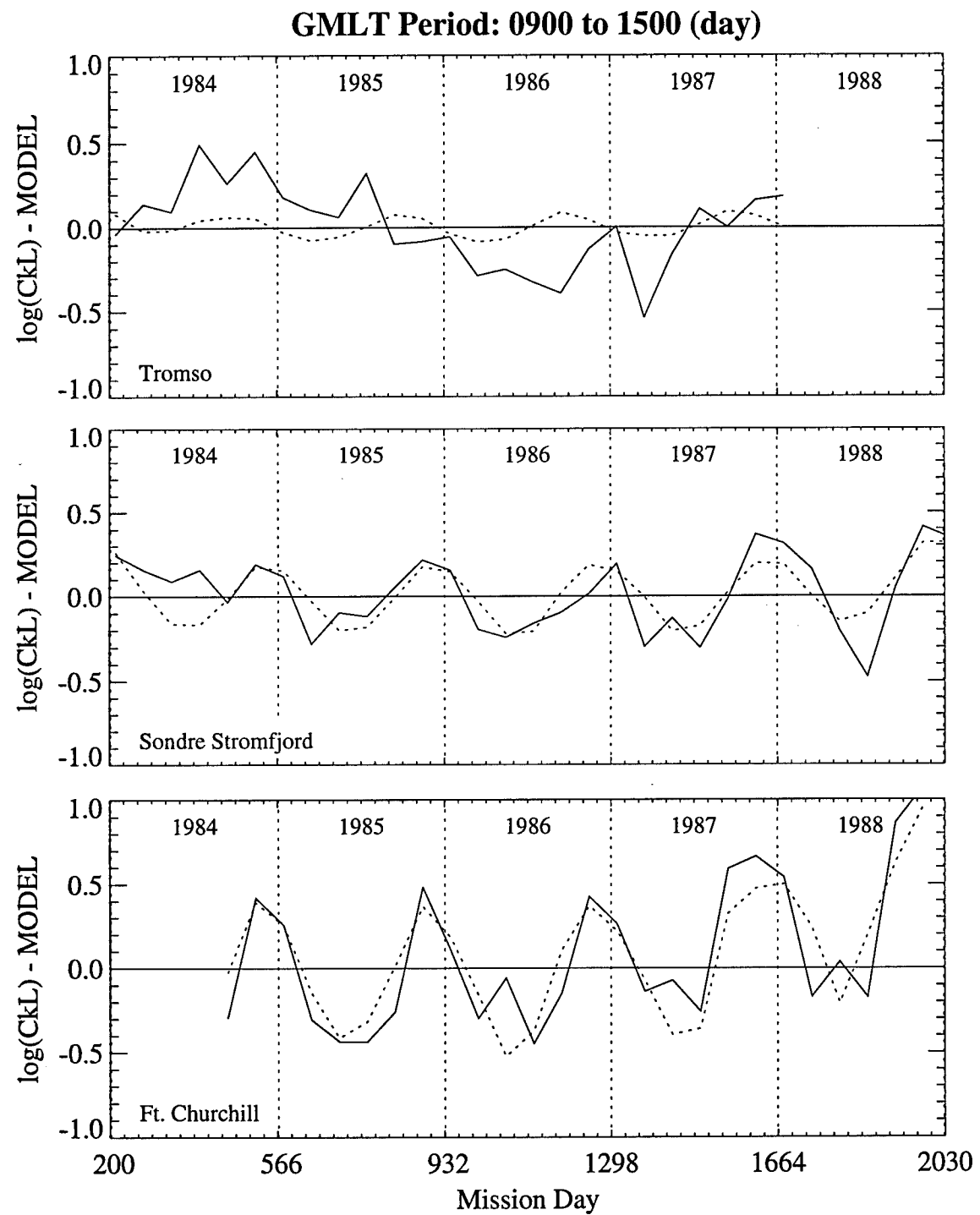


Figure 11: Data from Figure 7 (day sector) with the results of the regression analysis (dotted curve).

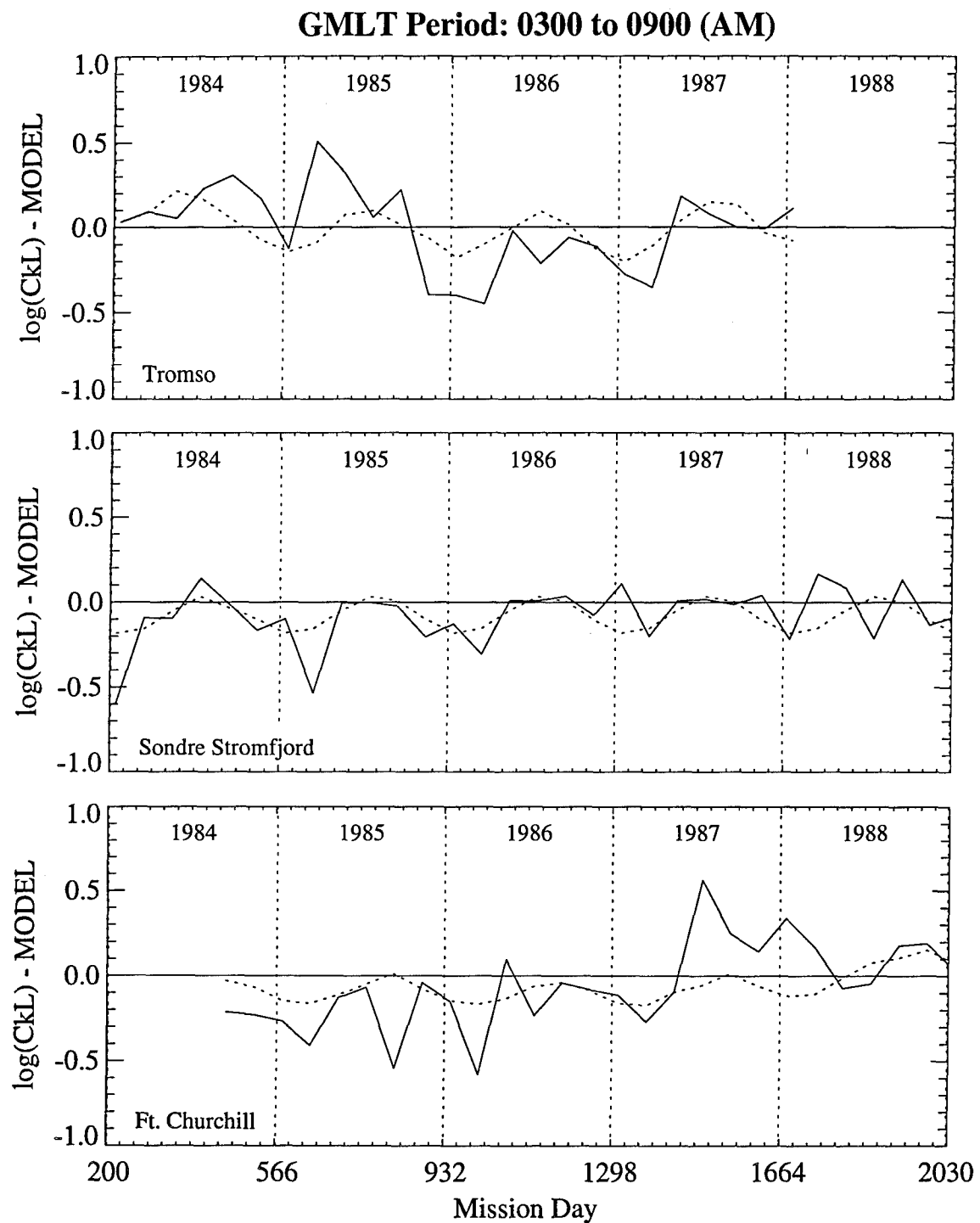


Figure 12: Data from Figure 8 (AM sector) with the results of the regression analysis (dotted curve).

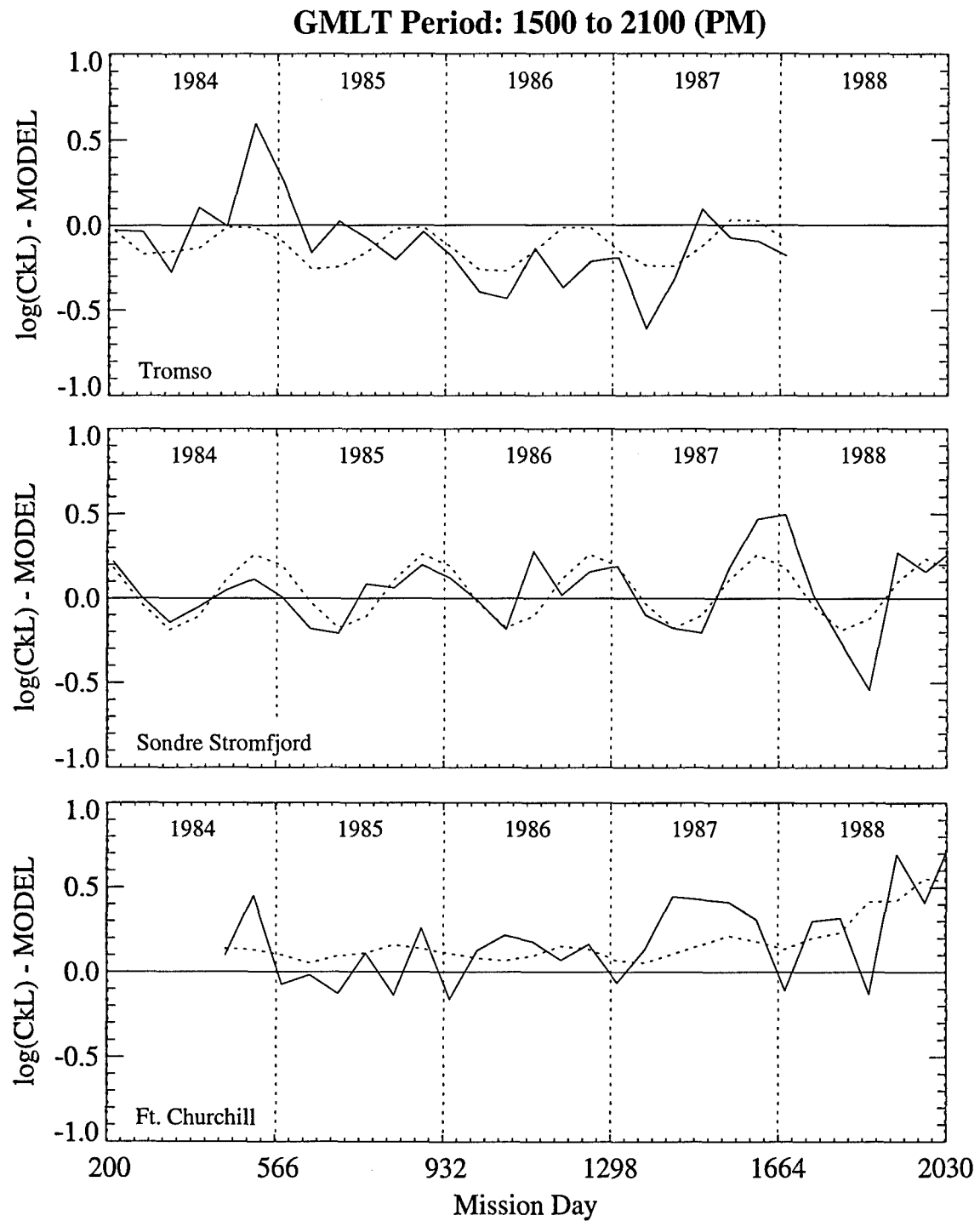


Figure 13: Data from Figure 9 (PM sector) with the results of the regression analysis (dotted curve).

lected. The longitudinal “hole” in our data set is quite obvious here — we have no observations covering the longitude sector from 45°E to 180°E. Our main question is whether the variations seen at Ft. Churchill will also be seen in this missing sector, or if there will be no seasonal variation in this sector. Based on works cited earlier in this section, we have chosen the latter option of limiting the seasonal variation to the US sector. This, then, leads to the next problem: at what longitudes is this behavior bound. On the Altantic side, we use the fact that there is little seasonal variation seen in the Tromso data set, and have set the eastern bound to half-way between Narssarssuaq and Tromso. Initially, we were inclined to use previous analyses that showed a similar lack of seasonal behavior at Poker Flat to use that station as a bound on the Pacific side. First, however, we generated plots similar to those shown for the HiLat/Polar BEAR stations for the Poker Flat (Wideband) data (night and day sectors), which are shown in Figure 15. The variations seen in this figure are strikingly similar to those seen at Ft. Churchill. This presents the problem of deciding where, to the west of Poker Flat, to terminate the seasonal variation with no data on which to base our decision. For now, we have arbitrarily set the western bound of the seasonal variation just to the west of Poker Flat.

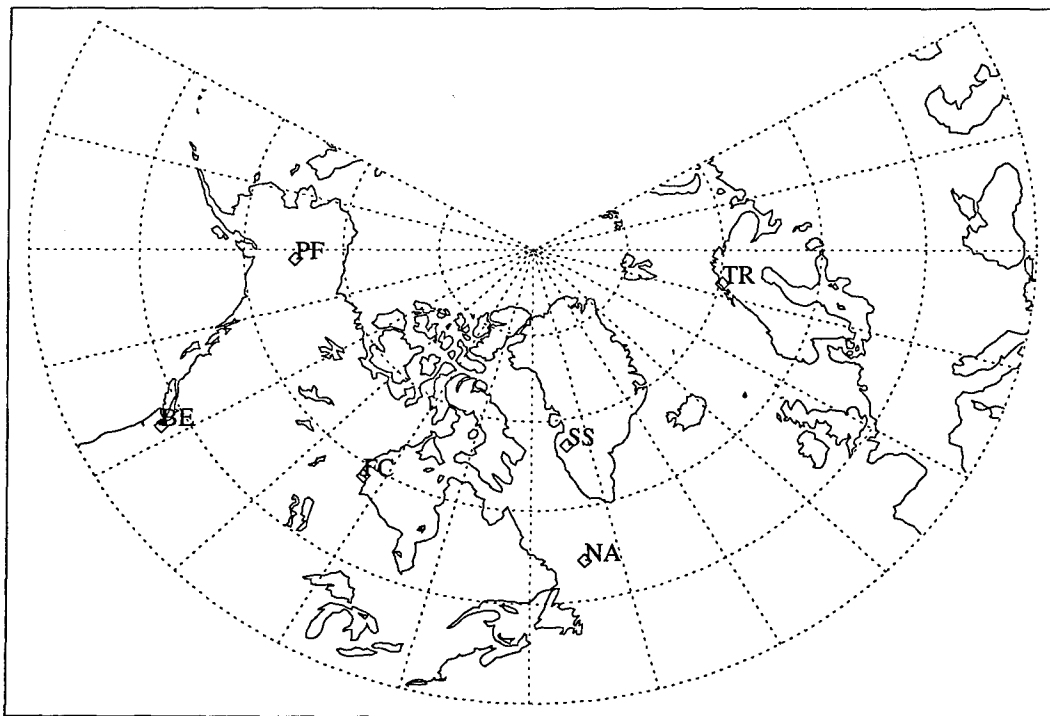


Figure 14: Location of stations used in the analysis.

The reconciliation problems involved the seasonal variation in the night sector as seen at Ft. Churchill and Sondre Stromfjord (Figure 10) and that observed at Narssarssuaq [Basu, 1975, Figure 3]. The Narssarssuaq observations were made largely in the auroral region, as were the bulk of the observations at Ft. Churchill. The Sondre Stromfjord observations (in

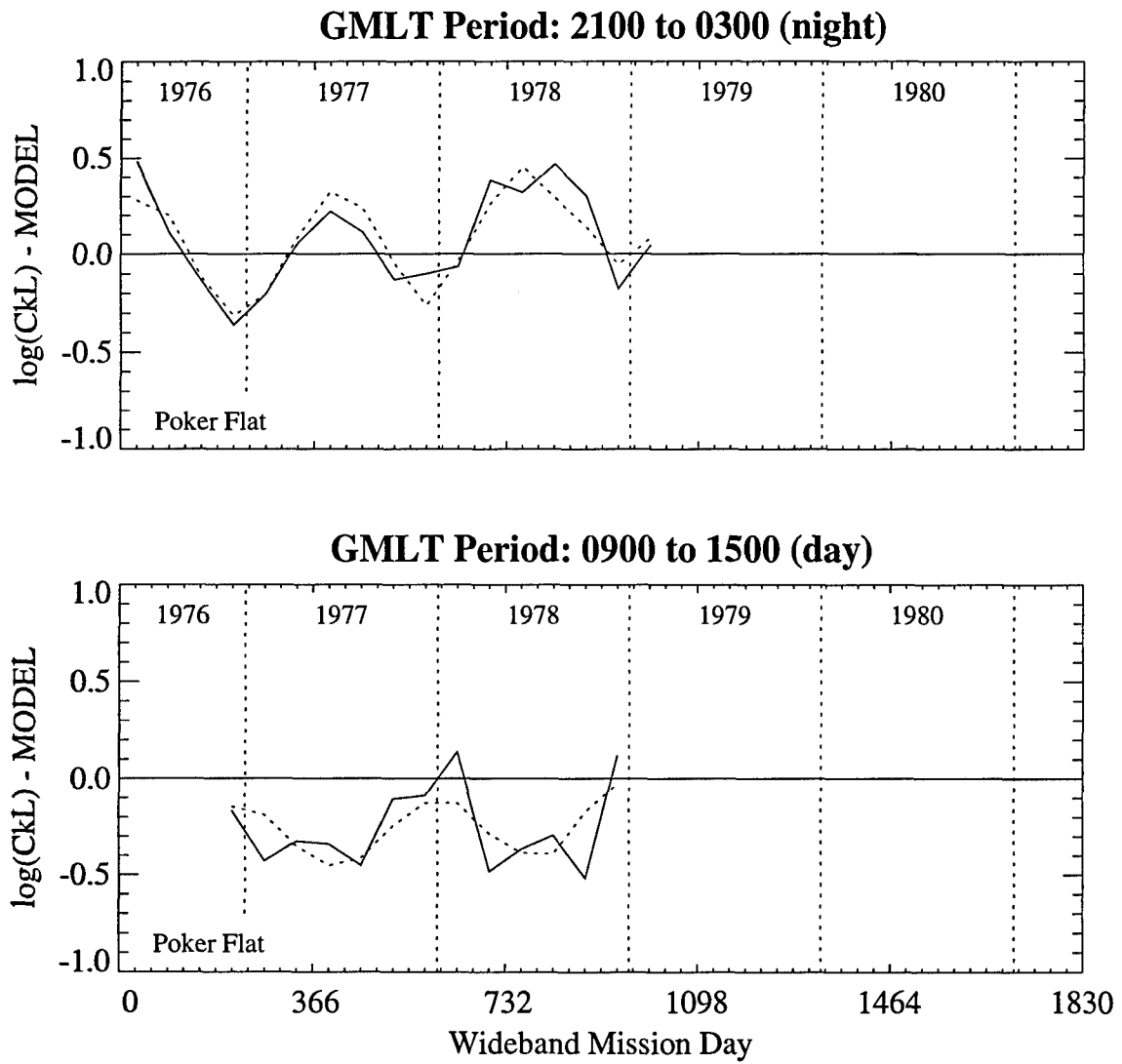


Figure 15: Variation of the residual  $\log(C_k L)$  as a function of days since the launch of Wideband at Poker Flat for the night (top plot) and day (bottom plot) sectors. Also shown is the regression fit to these data (dotted curves).

the night sector) were made largely in the polar cap, as were a subset of the Ft. Churchill observations. Both Ft. Churchill and Narssarssuaq show strong seasonal behavior in the night sector, but Sondre Stromfjord shows little. The Ft. Churchill and Sondre Stromfjord data sets were further subdivided into latitude categories to see if the seasonal signature was absent in the Ft. Churchill observations made in the polar cap (designated here as observations more than  $5^\circ$  poleward of the auroral enhancement latitude from the model) or present in the Sondre Stromfjord observations made in the auroral region (less than  $5^\circ$  poleward of the auroral enhancement latitude). The polar-cap subset of the Ft. Churchill data continued to show a seasonal variation, while a very weak seasonal variation appeared in the auroral subset of the Sondre Stromfjord data.

After trying numerous schemes for modeling this behavior, we have settled on a compromise solution. The seasonal variation is modeled independently for the polar cap region and the auroral (and sub-auroral) region. The point (in latitude) at which these two regions are divided is defined as  $5.5^\circ$  poleward of the auroral enhancement latitude, with a transition width set to damp out the seasonal variation seen at Ft. Churchill's latitude just poleward of the equatorward edge of Sondre Stromfjord's field-of-view. Note that this problem was not encountered in the day sector, where both Ft. Churchill and Sondre Stromfjord are equatorward of the "auroral enhancement" and showed the same seasonal variation. The seasonal variation is implemented in the following equation:

$$f_S(\Lambda, \phi_m, \tau_m, D, SSN) = f_{S,A} + (f_{S,PC} - f_{S,A}) F_1(\Lambda) \quad (20)$$

where  $\Lambda$  is as defined in Eq. (2),  $\phi_m$  is the geomagnetic longitude,  $\tau_m$  is the geomagnetic local time,  $D$  is the day of the year,  $f_{S,A}$  and  $f_{S,PC}$  are the seasonal variations in the auroral and polar-cap regions, respectively, and  $F_1$  is an interpolation function given by

$$F_1(\Lambda) = \frac{1}{2} \left[ 1 + \operatorname{erf} \left( \frac{\Lambda - \Lambda_S}{W_S} \right) \right] \quad . \quad (21)$$

The variation in the aurora region is given by

$$f_{S,A} = [c_1 + (c_2 - c_1) F_2(\tau_m)] G(\phi_m, \phi_{m,S}, \Delta\phi_{m,S}, W_{\phi,S}, W_{\phi,S}) \quad (22)$$

where  $G$  is given by Eq. (16),  $F_2$  is given by

$$F_2(\tau_m) = \frac{1}{2} \left[ 1 + \operatorname{erf} \left( \frac{\tau_m - \tau_{m,S}}{W_{\tau,S}} \right) \right] \quad , \quad (23)$$

and the  $c_1$  and  $c_2$  parameters are the seasonal variation in two adjacent local-time sectors given by

$$c_n = c_{n,0} + c_{n,R} \frac{SSN}{100} + c_{n,D} \cos(D - D_{n,0}) \quad , \quad (24)$$

where  $n$  is 1 – 4 corresponding to the four GMLT sectors (1: midnight, 2: AM, 3: noon, 4: PM). The  $\tau_{m,S}$  times in Eq. (23) are the GMLT values that define the boundaries between these time sectors (3.0, 9.0, 15.0, and 21.0).

Given the limited amount of “pure” polar-cap observations other than the night sector from Sondre Stromfjord, we have set the  $f_{S,PC}$  term in Eq. (20) to zero. We were tempted to put in an ad hoc variation based on recent modeling work by *Sojka et al.* [1994], but have decided to leave this issue to be addressed at a later time using a data set collected within the polar cap. (Note: A data set that would be useful in this regard is the PL/GPIA Thule scintillation data set.)

The 22 model parameters in these equations were derived from the considerations discussed earlier in this section and from the behavior at Ft. Churchill and Poker Flat. Table summarizes the values of these parameters. The seasonal term calculated from Eq. (20) is then added to the model value for  $\log(C_k L)$  calculated from Eq. (1).

Earlier, we mentioned that an  $SSN$ -dependence was included in the seasonal variation as the residual- $\log(C_k L)$  plots showed a clear variation with  $SSN$ , in spite of our assumption that we would be removing  $SSN$  effects by removing the model for  $SSN$  variation described in Section 3.2. The fact that the seasonal variation does depend on  $SSN$  is not in itself surprising, particularly if this effect is due to movement of solar-produced plasma in and around the high-latitude region. Our concern is that our analysis presupposed that the seasonal variation was independent of, or separable from, the  $SSN$  variation so that we could analyze for them separately (a technique used in previous WBMOD modeling work [*Fremouw and Robins, 1985*]). Given time and resources, we would reopen the geophysical variations analysis and approach the modeling of these variations together, much as the  $SSN$  and  $K_p$  variations were dealt with together. As neither time nor additional resources are available, we will implement these variations as they are described herein, with a caveat that there *may* be a double accounting for some  $SSN$ -dependent variations.

**3.4 Modification to Mid-Latitude  $\log(C_k L)$  Model.** As stated in Section 3.2, we found that we needed to adjust the parameters to the mid-latitude  $\log(C_k L)$  model [Eq. (6)] in order to obtain the best fit to the observations. As a result of earlier modeling work, the base  $\log(C_k L)$  value [parameter  $C_{M,0}$  in Eq. (6)] was set to 30.24, the variation with  $R$  ( $\Delta C_{M,R}$ ) was set to 0.40, and the diurnal variation ( $\Delta C_{M,\tau}$ ) was set to 0.30 [*Robins et al., 1986*]. The new values for these parameters, derived by including the coefficients to Eq. (6) in the fitting process, are 29.01, 0.40, and 0.37.

Table 5: Values of the coefficients for the seasonal variation.

Value	Symbol	Description
5.5	$\Lambda_S$	Seasonal latitude boundary (auroral/polar cap)
1.0	$W_S$	Width of latitude transition
345.0	$\phi_{m,S}$	Center longitude, seasonal variation
180.0	$\Delta\phi_{m,S}$	Width of longitude sector, seasonal variation
30.0	$W_{\phi,S}$	Width of longitude transitions
0.5	$W_{\tau,S}$	Width of local-time transitions
-0.15	$c_0$	DC term (midnight sector)
-0.10		DC term (AM sector)
-0.15		DC term (noon sector)
0.05		DC term (PM sector)
0.45	$c_R$	SSN term (midnight sector)
0.15		SSN term (AM sector)
0.60		SSN term (noon sector)
0.25		SSN term (PM sector)
0.40	$c_D$	Seasonal magnitude (midnight sector)
0.05		Seasonal magnitude (AM sector)
0.45		Seasonal magnitude (noon sector)
0.05		Seasonal magnitude (PM sector)
183.5	$D_0$	Seasonal phase (midnight sector)
104.5		Seasonal phase (AM sector)
15.0		Seasonal phase (noon sector)
76.5		Seasonal phase (PM sector)

The reduction in the lead term ( $C_{M,0}$ ) is not surprising. When the initial value was derived, it was derived solely from Stanford Wideband observations that provided a higher value for this parameter than did the Bellevue HiLat observations then available. We chose to go with the higher Stanford-Wideband value because we only had a small amount of Bellevue-HiLat data and most of it is from high mid-latitude, and, if the model were to be in error, we wanted it to err on the high side. We had already reduced the value of  $C_{M,0}$  to 29.32 in Version 12 as a result of a parametric study conducted for a system design project, and this change will move the model down into complete agreement with the (now expanded) Bellevue-HiLat/Polar BEAR measurements.

**3.5 Variation of the  $\log(C_k L)$  PDF Width.** The value for the half-width of the  $\log(C_k L)$  PDF,  $\sigma$ , used at high latitudes in WBMOD Version 12 was based on an analysis of a subset of the HiLat/Polar BEAR database conducted several years ago [Secan and Fremouw, 1988]. Values for the half-width were extracted by fitting normal distributions to discrete PDFs

generated from the various data sets. It was found that a value of 1.0 for  $\sigma$  was fairly representative of all times and locations in the data set. In the present analysis, values for  $\sigma$  have been calculated from the standard deviation of  $\log(C_k L)$  from the mean  $\log(C_k L)$ , which we will denote  $\sigma_{SD}$ . The relationship between  $\sigma$  derived in the previous analysis and  $\sigma_{SD}$  is  $\sigma_{SD} = \sigma/\sqrt{2}$ . Thus, the current value for  $\sigma$  of 1.0 corresponds to a  $\sigma_{SD}$  value of  $1/\sqrt{2}$ .

The results of the present study do not appreciably differ from those obtained in the early one. We have looked at various aspects of the variation of  $\sigma_{SD}$  (with latitude, local time,  $SSN$ , and  $K_p$ ) and while we have found variations away from a mean value for  $\sigma_{SD}$ , we have not found any systematic variations significant enough to include in the model. The results are fairly well summarized by Figures 16 and 17. The variation of  $\sigma_{SD}$  as a function of  $\Lambda$  for various GMLT sectors is shown for all four Hilat/Polar BEAR stations, and the present ( $1/\sqrt{2}$ , dotted line) and new (0.8, solid line) constant values for  $\sigma_{SD}$  are shown for comparison. The only change we intend to make in this parameter from WBMOD Version 12 is to change the constant value from 1.0 to 1.13.

**3.6 Comparison with Narssarsuaq Observations.** Figures 18 (from *Basu* [1975]) and 19 provide an independent check of the new high-latitude model. The data in Figure 18 were taken on a propagation path between Narssarsuaq and ATS-3 during the years 1968 through 1972 during the time interval 2200 to 0200 GMLT for  $K_p \leq 30$ . The data plotted in Figure 19 were generated from the new model using  $SSN = 80$  and  $K_p = 1.66$ . The agreement between the two is fairly good, with the most obvious differences being an underestimate of the percent of time that  $S_4$  exceeded 30% during the summer months and the tendency for the observed seasonal variation to be less symmetric than the sine function used in the model. Given that the only information we used from the Narssarsuaq observations was the fact that a seasonal variation was seen at Narssarsuaq, we are very pleased with the level of agreement shown in these two figures.

#### 4. WBMOD Version 13

The new models for high-latitude scintillation described in this report have been implemented in Version 13 of WBMOD. The primary differences between Version 13 and Version 12 are the replacement of the high-latitude model for  $\log(C_k L)$  with the model described in this report and the addition of the DMSP SSJ/4 precipitation boundary as an explicit optional input. The User Guide written for Version 12 has been updated to reflect the changes made in version 13. Copies of this document were provided to PL/GPIA and to the Air Force Space Forecast Center (AFSFC). The AFSFC also received a copy of the research version of WBMOD Version 13 compiled to run on an Intel 80386-class computer.

#### 4. Conclusion

The upgrade to the equatorial and high-latitude regions of the WBMOD  $C_k L$  model has been completed, and the upgrade has been implemented in the research version of WBMOD Version 13. The WBMOD User's Guide has been modified to include changes made to the

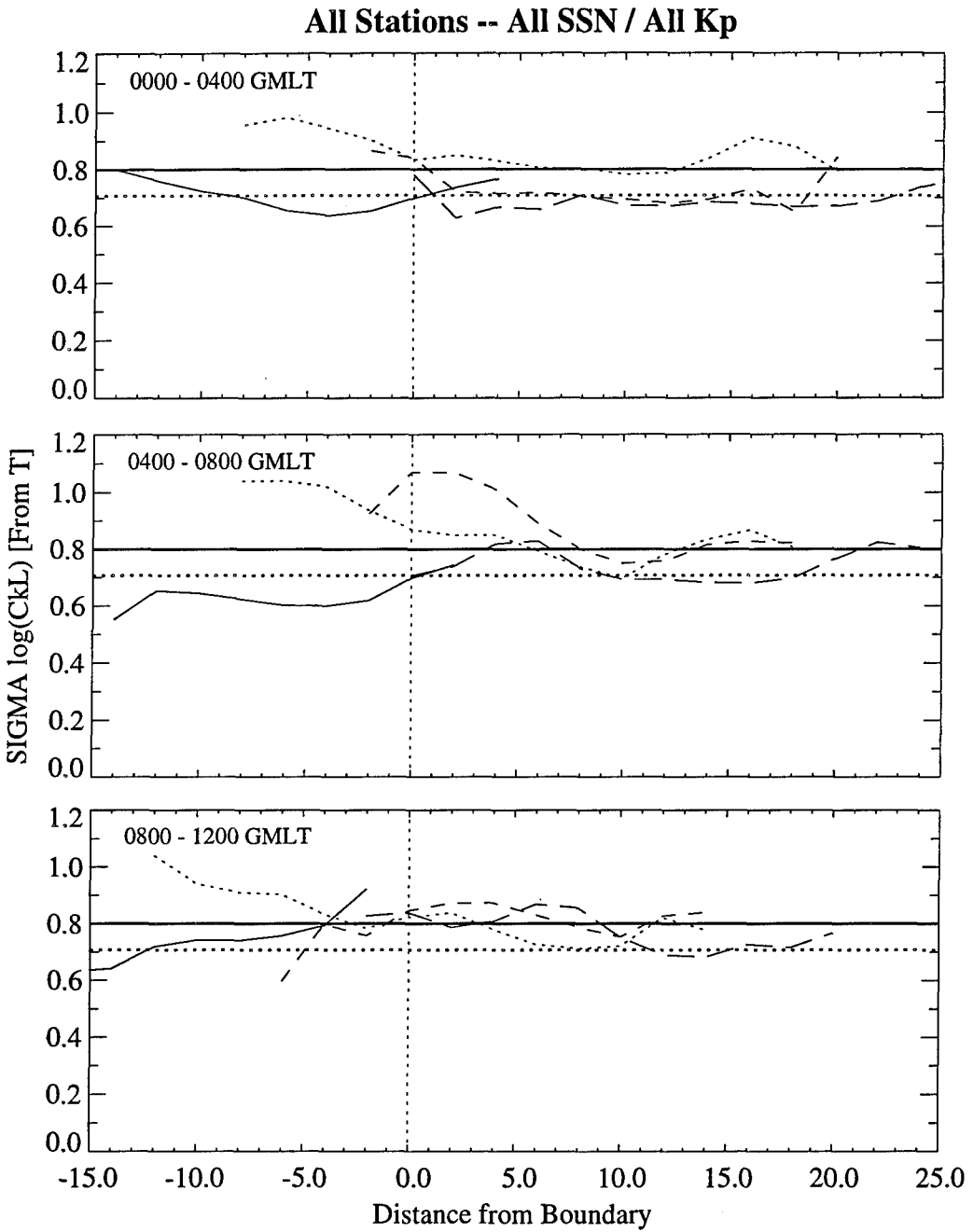


Figure 16: Variation of  $\sigma_{SD}$  with the latitude distance from the SSJ/4 precipitation boundary for six geomagnetic (apex) local time ranges for all  $SSN$  and all  $K_p$  for all four Hi-Lat/Polar BEAR stations (solid curve: Bellevue; dotted curve: Tromso; short-dash curve: Ft. Churchill; long-dash curve: Sondre Stromfjord). The heavy dotted line indicates the value for  $\sigma_{SD}$  corresponding to WBMOD Version 12, and the heavy dotted line indicates the new value.

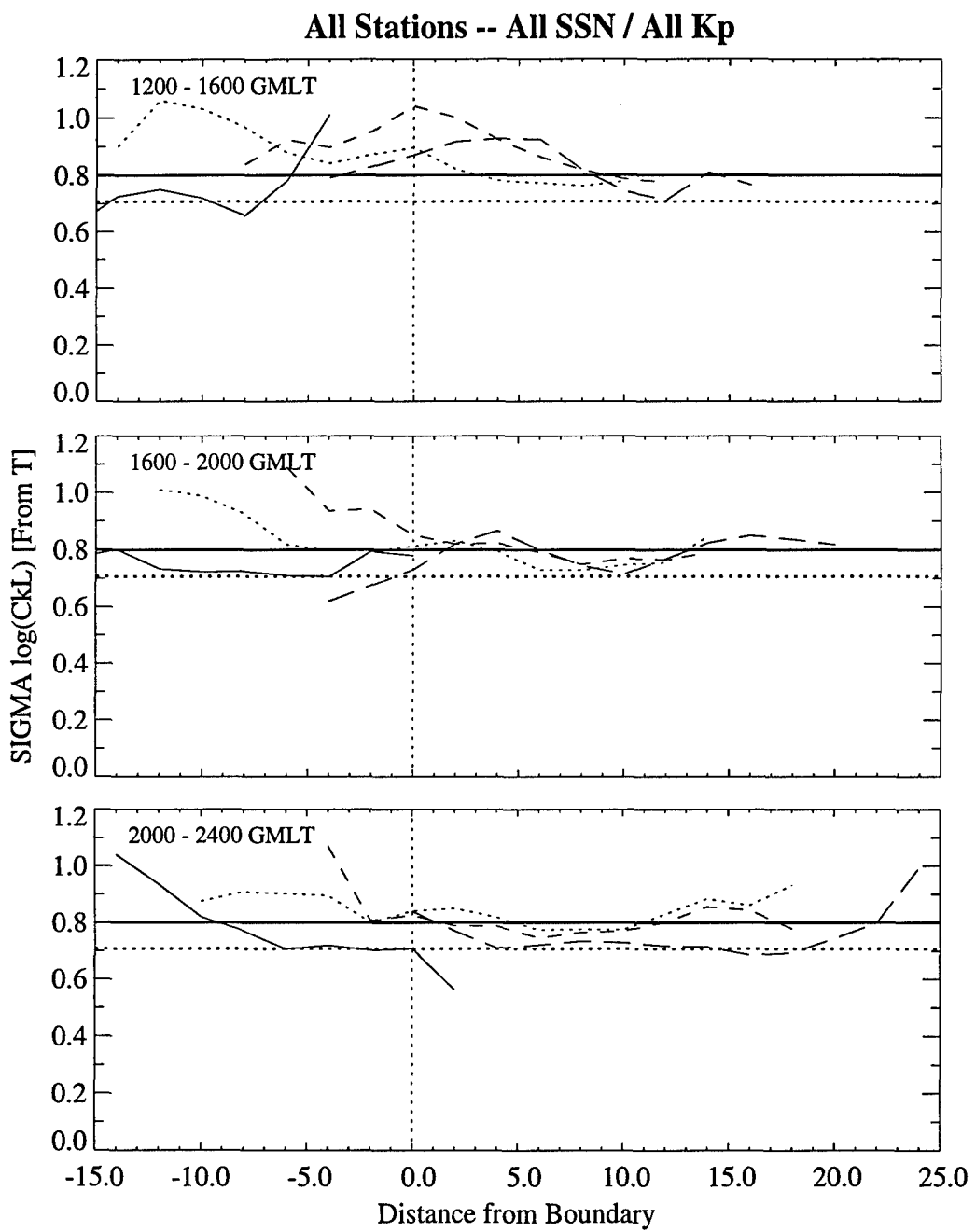


Figure 17: Continuation of comparison in Figure 16.

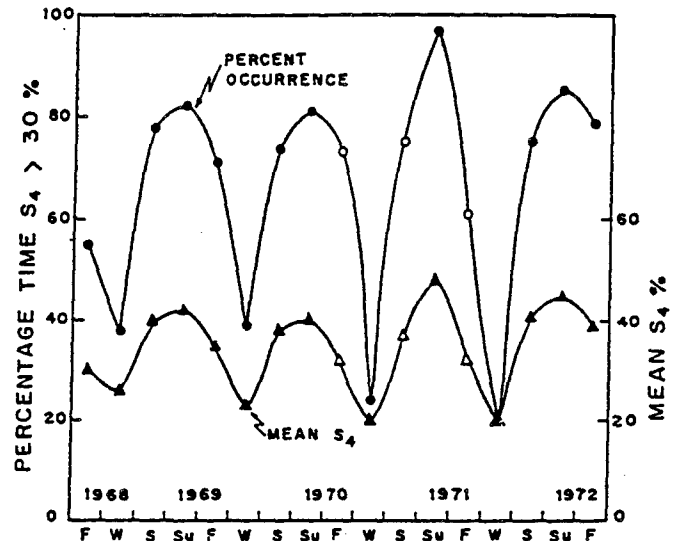


Figure 18: Observed seasonal variation of scintillation at Narssarssuaq, Greenland (from Basu [1975]).

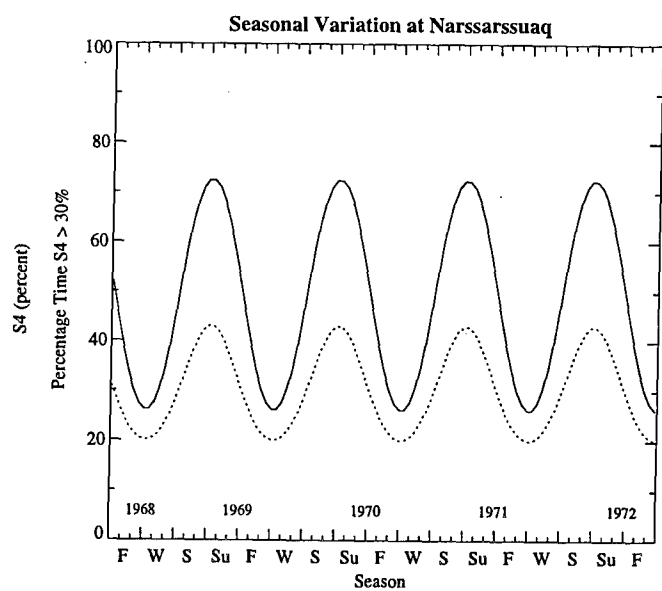


Figure 19: Modeled seasonal variation at Narssarssuaq. The solid line is the percent of time that  $S_4 \geq 30\%$  and the dotted line is the average  $S_4$ .

model as part of the high-latitude upgrade.

While this concludes the planned upgrades to the WBMOD model, there are still several open questions that, if resolved, could improve the model further:

- How does  $\log(C_k L)$  vary with  $K_p$  and  $SSN$  in the polar cap, particularly from just poleward of the cusp region to poleward of the field-of-view at Sondre Stromfjord in the midnight sector?
- What is the seasonal variation in the Russian sector?
- What is the seasonal variation in the polar cap?

As noted in the section describing the seasonal variations, there is a data set that could be used to investigate the polar-cap variation, a set of scintillation observations made at Thule, Greenland, by PL/GPIA over a several-year period. (It was not included in this analysis due to limitation of resources.) Modeling of the seasonal variation in the Russian sector may need to be based on analysis of satellite data, such as that shown in *Sojka et al.* [1994] due to a lack of a large database of ground-based scintillation observations from that sector.

## REFERENCES.

Basu, Su., Universal time seasonal variations of auroral zone magnetic activity and VHF scintillations, *J. Geophys. Res.*, **80**, 4725–4728, 1975.

Basu, Su. and J. Aarons, The morphology of high-latitude VHF scintillation near 70°W, *Radio Sci.*, **15**, 59–70, 1980.

Bevington, P. R., *Data Reduction and Error Analysis for the Physical Sciences*, 336pp., McGraw Hill, New York, 1969.

Briggs, B. H. and I. A. Parkin, On the variation of radio star and satellite scintillations with zenith angle, *J. Atmosph. Terr. Phys.*, **25**, 339–365, 1963.

Buchau, J., E. J. Weber, D. N. Anderson, H. C. Carlson, J. G. Moore, B. W. Reinisch, and R. C. Livingston, Ionospheric structures in the polar cap: Their origin and relation to 250-MHz scintillation, *Radio Sci.*, **20**, 325–338, 1985.

de la Beaujardiere, O. and D. McNeil, A FORTRAN Program for Calculating F-layer-Produced Scintillation, *Tech. Note, SRI Project 1079*, Stanford Research Institute, Menlo Park, CA, 1971.

de la Beaujardiere, O., V. B. Wickwar, G. Caudal, J. M. Holt, J. D. Craven, L. A. Frank, L. H. Brace, S. Evans, J. D. Winningham, and R. A. Heelis, Universal time dependence of nighttime F region densities at high latitude, *J. Geophys. Res.*, **90**, 4319–4332, 1985.

Fremouw, E. J., The Polar BEAR ionospheric experiments, A pre-launch overview, *Report DNA-TR-86-156*, Defense Nuclear Agency, Washington, DC, 1986.

Fremouw, E. J. and H. F. Bates, Worldwide behavior of average VHF-UHF scintillation, *Radio Sci.*, 10, 863-869, 1971.

Fremouw, E. J. and J. M. Lansinger, A Computer Model for High-Latitude Phase Scintillation Based on Wideband Satellite Data from Poker Flat, *Report DNA5686F*, Defense Nuclear Agency, Washington, DC, 1981.

Fremouw, E. J. and C. L. Rino, An empirical model for average F-layer scintillation at VHF/UHF, *Radio Sci.*, 8, 213-222, 1973.

Fremouw, E. J. and C. L. Rino, A signal-statistical and morphological model of ionospheric scintillation, *Proc. of AGARD Conference on Operational Modeling of the Aerospace Environment*, Ottawa, Canada, 1978.

Fremouw, E. J. and R. E. Robins, An Equatorial Scintillation Model, *DNA-TR-85-333*, Defense Nuclear Agency, Washington, DC, 1985.

Fremouw, E. J., R. L. Leadabrand, R. C. Livingston, M. D. Cousins, C. L. Rino, B. C. Fair, and R. A. Long, Early results from the DNA Wideband satellite experiment — Complex-signal scintillation, *Radio Sci.*, 13, 167-187, 1978.

Fremouw, E. J., H. C. Carlson, T. A. Potemra, P. F. Bythrow, C. L. Rino, J. F. Vickrey, R. L. Livingston, C.-I. Meng, D. A. Hardy, F. J. Rich, R. A. Heelis, W. B. Hanson, and L. A. Wittwer, The HiLat satellite mission, *Radio Sci.*, 20, 416-424, 1985.

Gussenhoven, M. S., D. A. Hardy, and N. Heinemann, Systematics of the equatorward diffuse auroral boundary, *J. Geophys. Res.*, 88, 5692-5708, 1983.

Rino, C. L. and E. J. Fremouw, The angle dependence of singly scattered wavefields, *J. Atmosph. Terr. Phys.*, 39, 859-868, 1977.

Rino, C. L., A. R. Hessing, V. E. Hatfield, and E. J. Fremouw, Two FORTRAN Programs for Calculating Global Ionospheric Amplitude and Phase Scintillation, *Tech. Report 8, SRII Project 4259*, SRI International, Menlo Park, CA, 1977.

Robins, R. E., J. A. Secan, and E. J. Fremouw, A Mid-Latitude Scintillation Model, *DNA-TR-86-381*, Defense Nuclear Agency, Washington, DC, 1986.

Secan, J. A., WBMOD Ionospheric Scintillation Model — An Abbreviated User's Guide, *NWRA-CR-93-R098*, Northwest Research Associated, Inc., Bellevue, WA, 1993.

Secan, J. A. and R. M. Bussey, An Investigation of Methods For Improving Models of Ionospheric Plasma-Density Irregularities and Radio-Frequency Scintillation, Scientific Report No. 2, *PL-TR-93-2260*, ADA278568, Phillips Laboratory, Hanscom AFB, MA, 1993.

Secan, J. A. and E. J. Fremouw, Development of Advanced Ionospheric Models in Support of Space-Based Radar Design Studies, Phase I, *NWRA-CR-88-R022*, Northwest Research Associates, Inc., Bellevue, WA, 1988.

Secan, J. A., M. P. Baldwin, and L. A. Reinleitner, Real-Time Scintillation Analysis System, Volume I: Technical Description, *Report NWRA-CR-89-R049*, Northwest Research Associates, Inc., Bellevue, WA, 1990.

Secan, J. A., R. M. Bussey, E. J. Fremouw, and L. A. Reinleitner, An Investigation of Methods For Improving Models of Ionospheric Plasma-Density Irregularities and Radio-Frequency Scintillation, Scientific Report No. 1, *PL-TR-93-2050*, ADA264156, Phillips Laboratory, Hanscom AFB, MA, 1993.

Sojka, J. J., M. D. Bowline, and R. W. Schunk, Patches in the polar ionosphere: UT and seasonal dependence, *J. Geophys. Res.*, 99, 14,959-14,970, 1994.

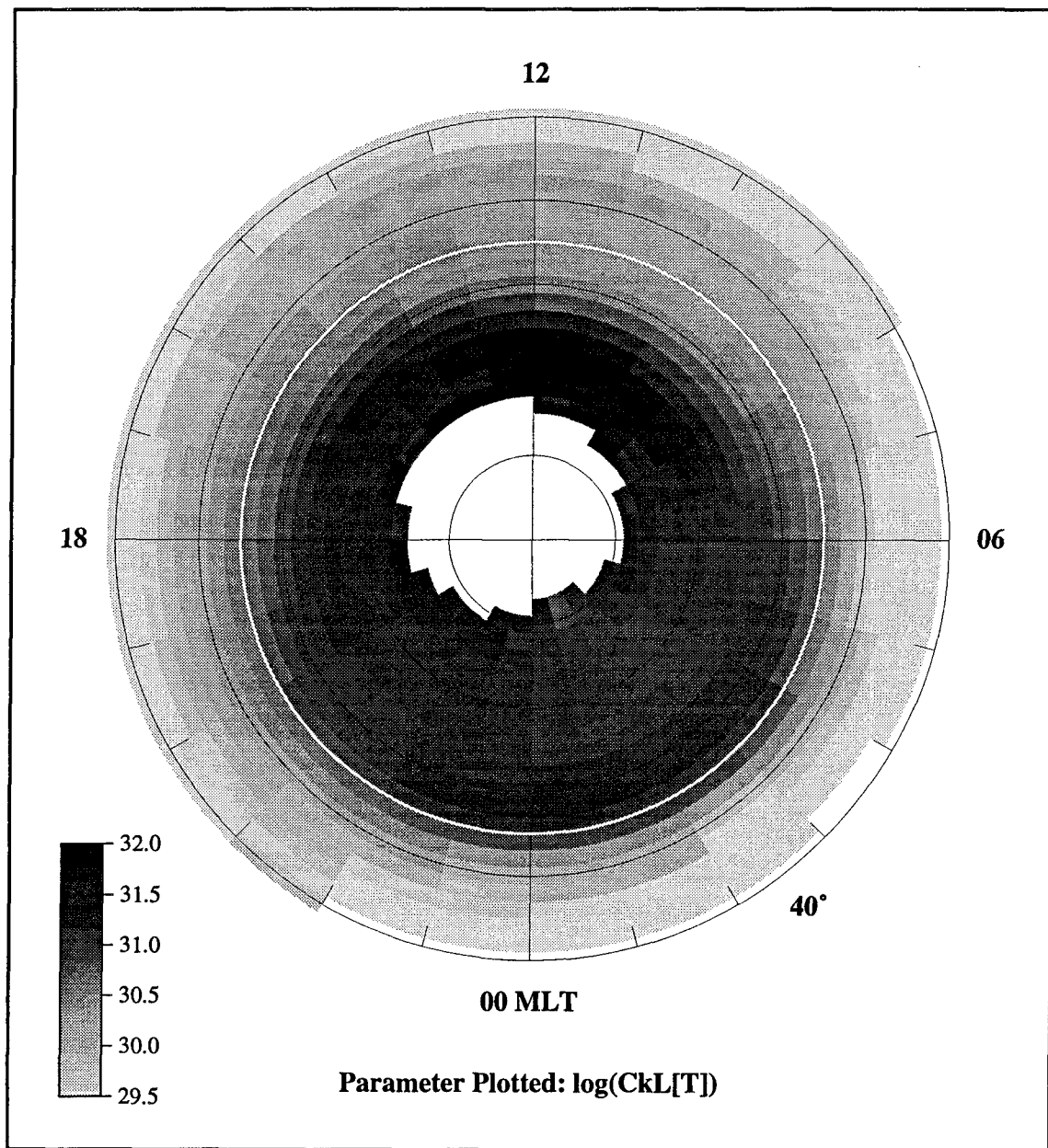
**THIS PAGE INTENTIONALLY LEFT BLANK**

## Appendix A. Grey-Shade Plots of High-Latitude $\log(C_k L)$ .

The figures in this appendix show the variation of  $\log(C_k L)$  from the composite Hi-Lat/Polar BEAR database as a function of the latitude distance from the auroral precipitation boundary ( $\Lambda$ ) and geomagnetic (apex) local time ( $\tau$ ). The location of the precipitation boundary (defined as  $\Lambda = 0$ ) is indicated on all figures by a solid white circle. The first figure is for the entire data set, *i.e.*, for all  $SSN$  and all  $K_p$ . The following six figures are for all  $K_p$  for six ranges of  $SSN$ : 0 to 25, 25 to 50, 50 to 75, 75 to 100, 100 to 125, and  $\geq 125$ . The final six figures are for all  $SSN$  for six ranges of  $K_p$ :  $0^\circ$  to  $1^\circ$ ,  $1^\circ$  to  $2^\circ$ ,  $2^\circ$  to  $3^\circ$ ,  $3^\circ$  to  $4^\circ$ ,  $4^\circ$  to  $5^\circ$ , and  $\geq 5^\circ$ .

These figures show the data used in the fitting process described in Section 3.2.

### Composite -- All Kp / All SSN

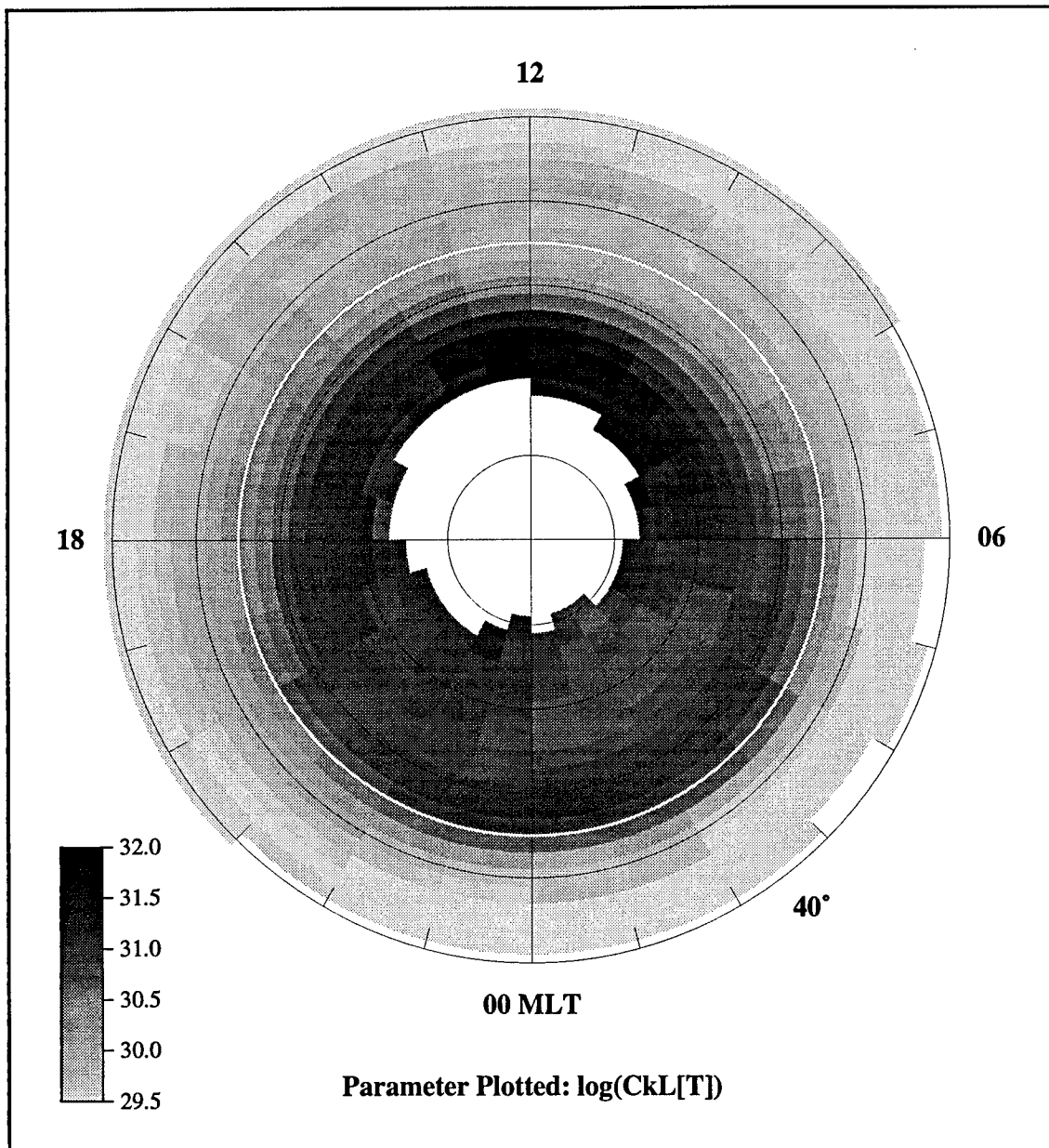


Latitude axis:  $55 + (\text{GMLAT-BNDLAT})$   
Range: 40.0 to 90.0  
Step size: 2.00

Time axis: Apex Local Time  
Step size: 1.00

Figure 20: Composite shade plot of  $\log(C_k L)$  for all SSN and all  $K_p$ . The radial axis is the latitude distance from the auroral precipitation boundary (solid white line) and the azimuthal coordinate is geomagnetic (apex) local time. The solid white circle indicates the zero point for the radial axis (*i.e.*, the auroral precipitation boundary).

Composite -- SSN Range: 0 to 25

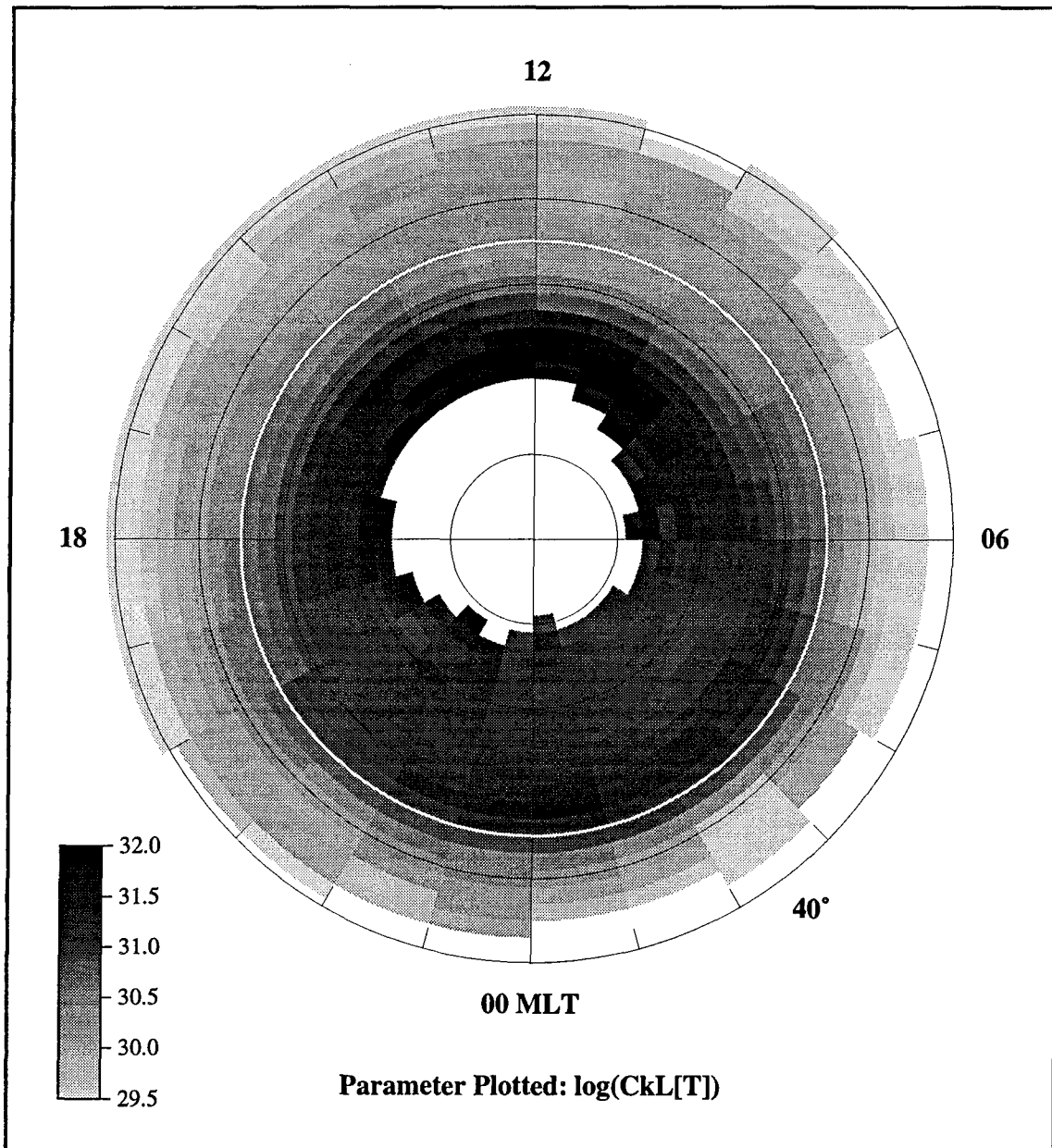


Latitude axis:  $55 + (\text{GMLAT} - \text{BNDLAT})$   
Range: 40.0 to 90.0  
Step size: 2.00

Time axis: Apex Local Time  
Step size: 1.00

Figure 21: Composite shade plot of  $\log(C_k L)$  for all  $K_p$  and  $0 \leq \text{SSN} \leq 25$ . Axis definition and annotation are as in Figure 20.

**Composite -- SSN Range: 25 to 50**

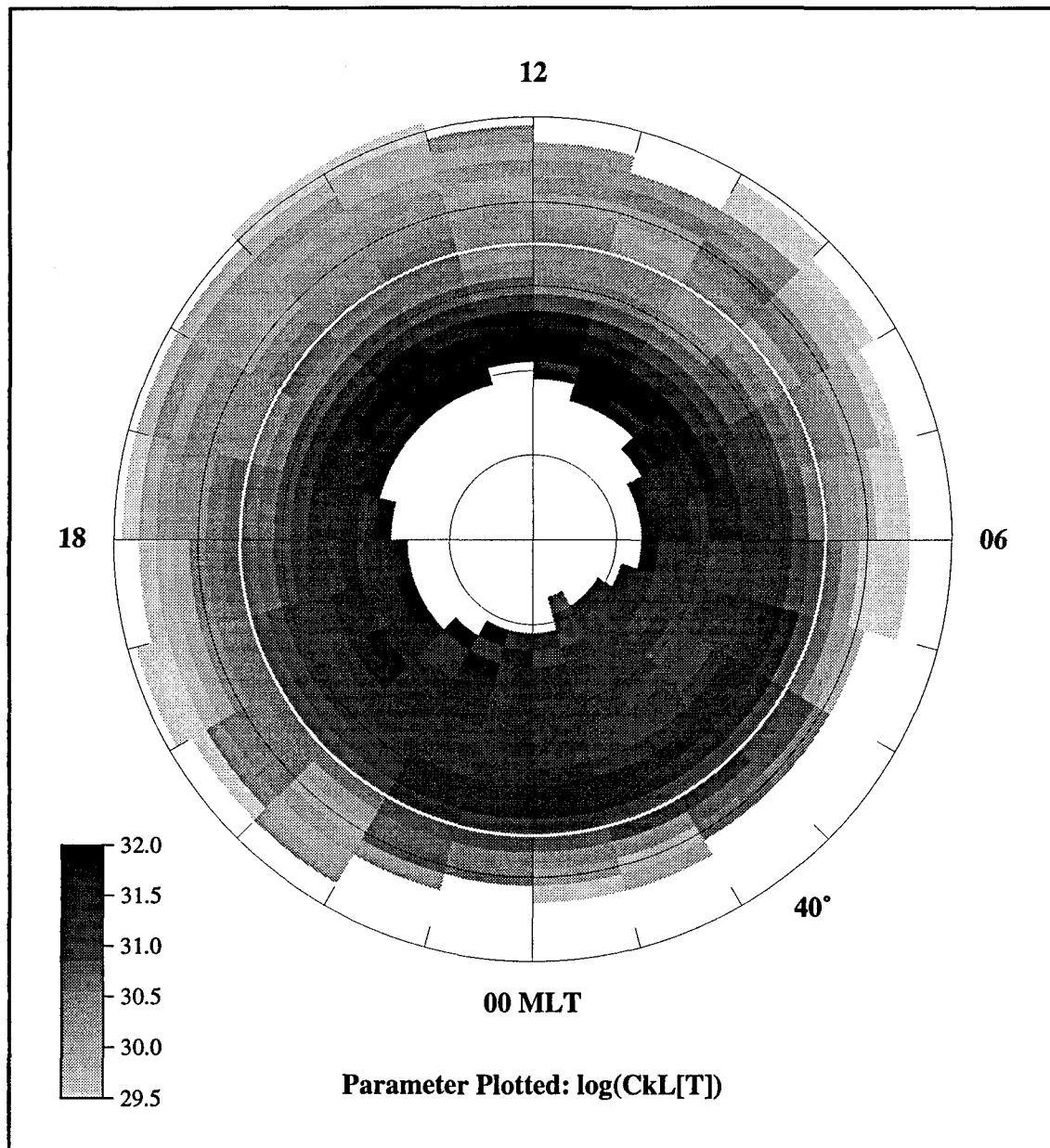


Latitude axis:  $55 + (\text{GMLAT-BNDLAT})$   
Range: 40.0 to 90.0  
Step size: 2.00

Time axis: Apex Local Time  
Step size: 1.00

Figure 22: Composite shade plot of  $\log(C_k L)$  for all  $K_p$  and  $25 \leq \text{SSN} \leq 50$ . Axis definition and annotation are as in Figure 20.

Composite -- SSN Range: 50 to 75



Latitude axis:  $55 + (\text{GMLAT} - \text{BNDLAT})$   
Range: 40.0 to 90.0  
Step size: 2.00

Time axis: Apex Local Time  
Step size: 1.00

Figure 23: Composite shade plot of  $\log(C_k L)$  for all  $K_p$  and  $50 \leq \text{SSN} \leq 75$ . Axis definition and annotation are as in Figure 20.

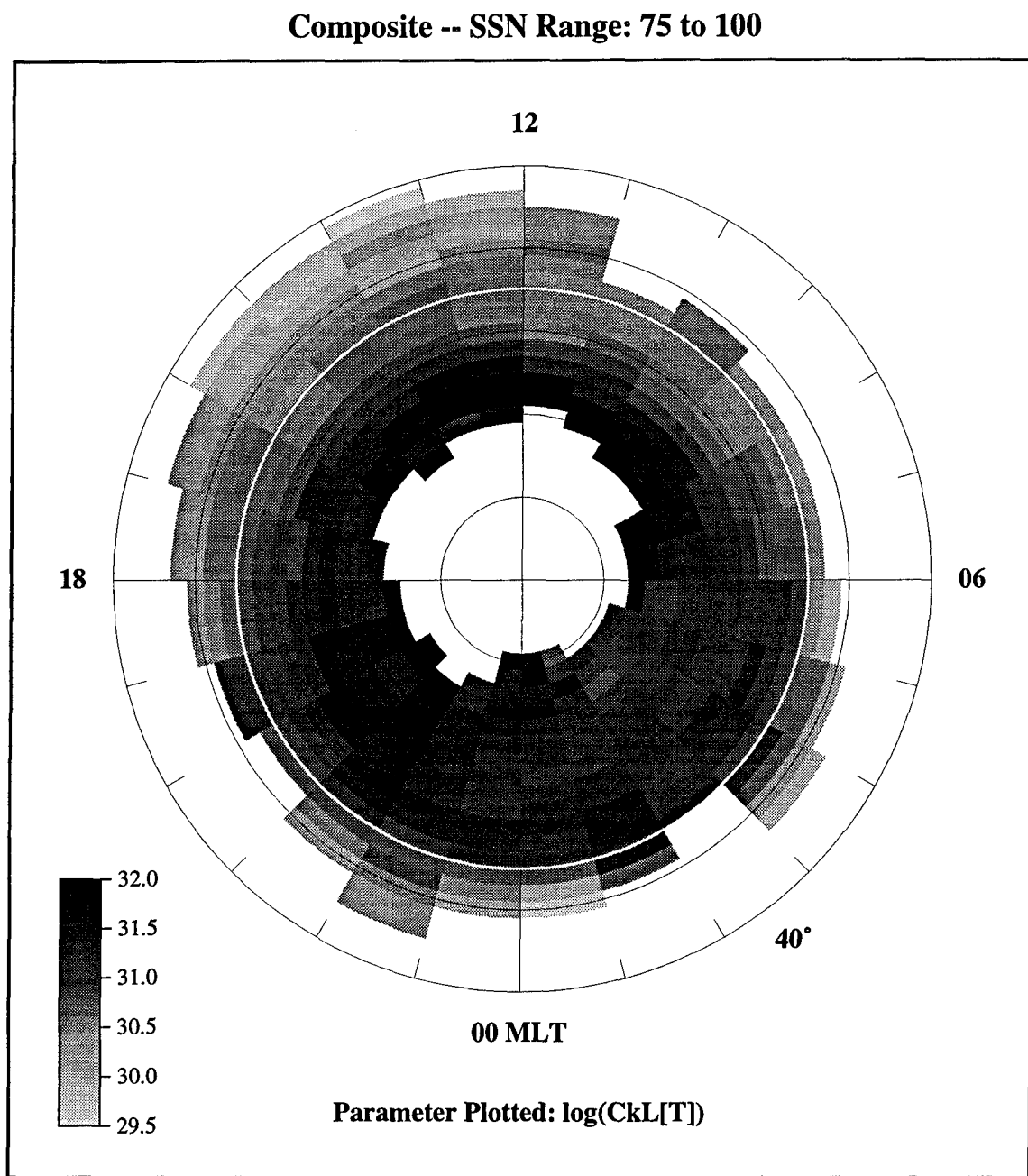
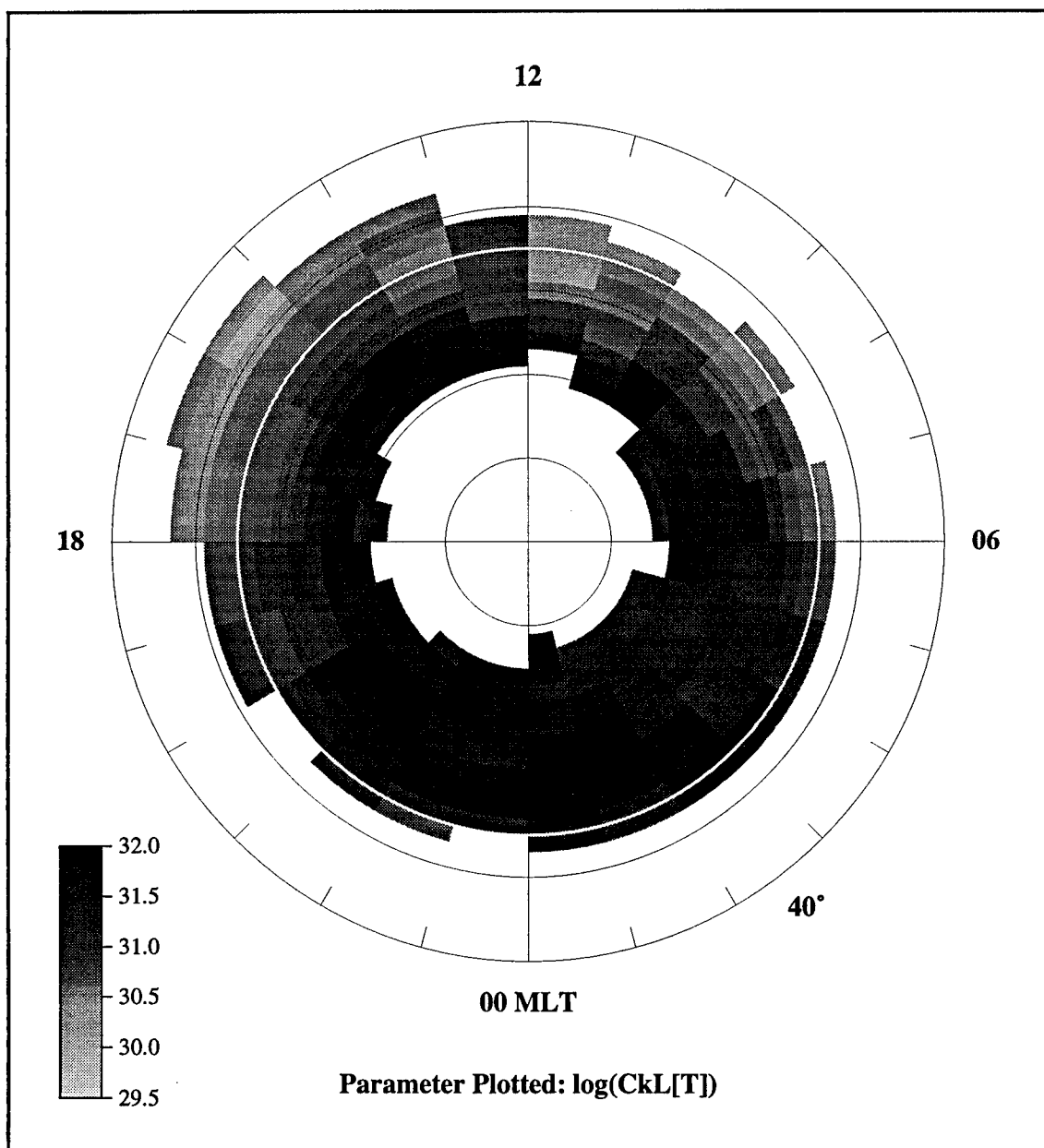


Figure 24: Composite shade plot of  $\log(C_k L)$  for all  $K_p$  and  $75 \leq \text{SSN} \leq 100$ . Axis definition and annotation are as in Figure 20.

**Composite -- SSN Range: 100 to 125**

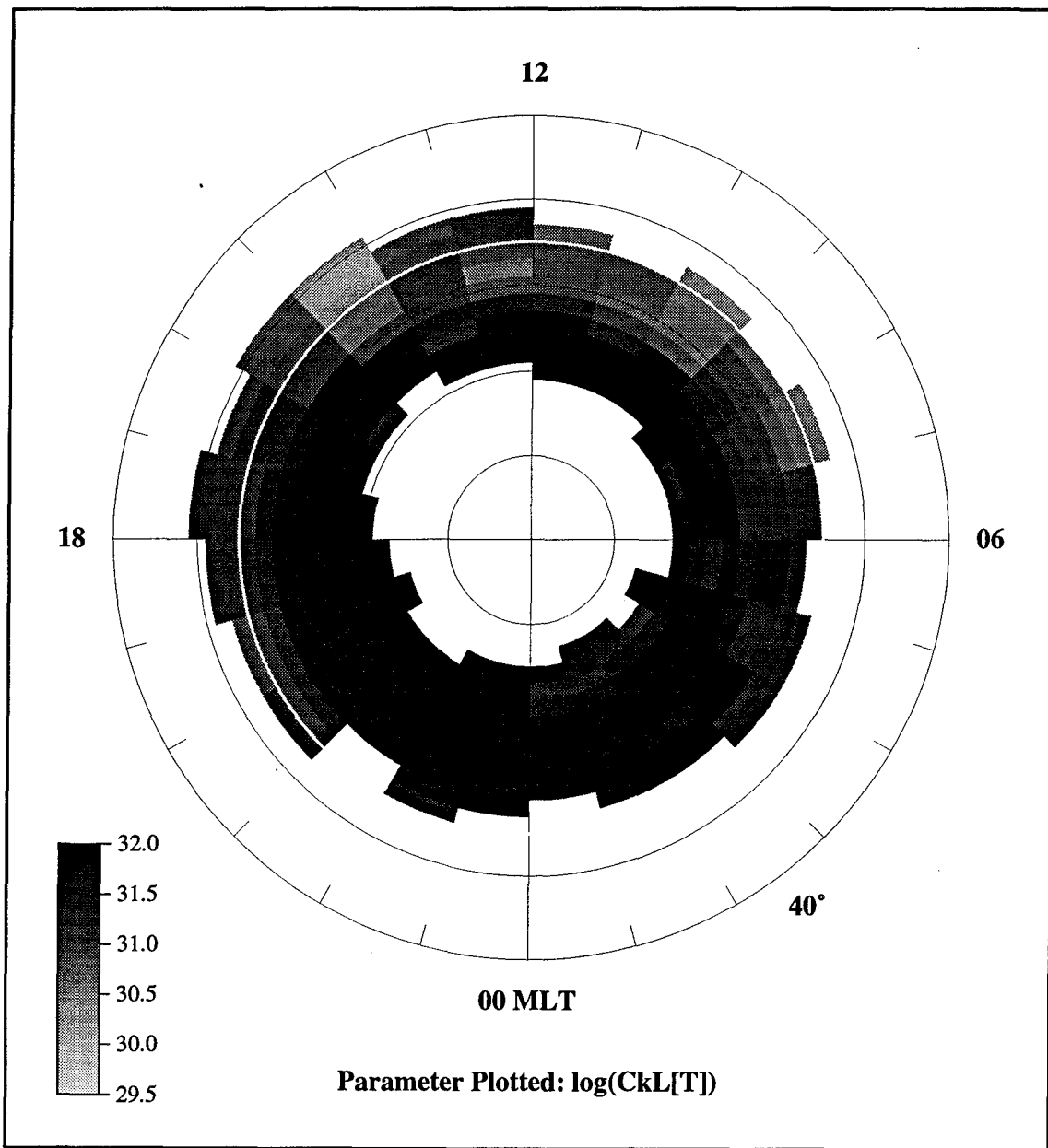


Latitude axis:  $55 + (\text{GMLAT-BNDLAT})$   
Range: 40.0 to 90.0  
Step size: 2.00

Time axis: Apex Local Time  
Step size: 1.00

Figure 25: Composite shade plot of  $\log(C_k L)$  for all  $K_p$  and  $100 \leq \text{SSN} \leq 125$ . Axis definition and annotation are as in Figure 20.

Composite -- SSN Range: > 125

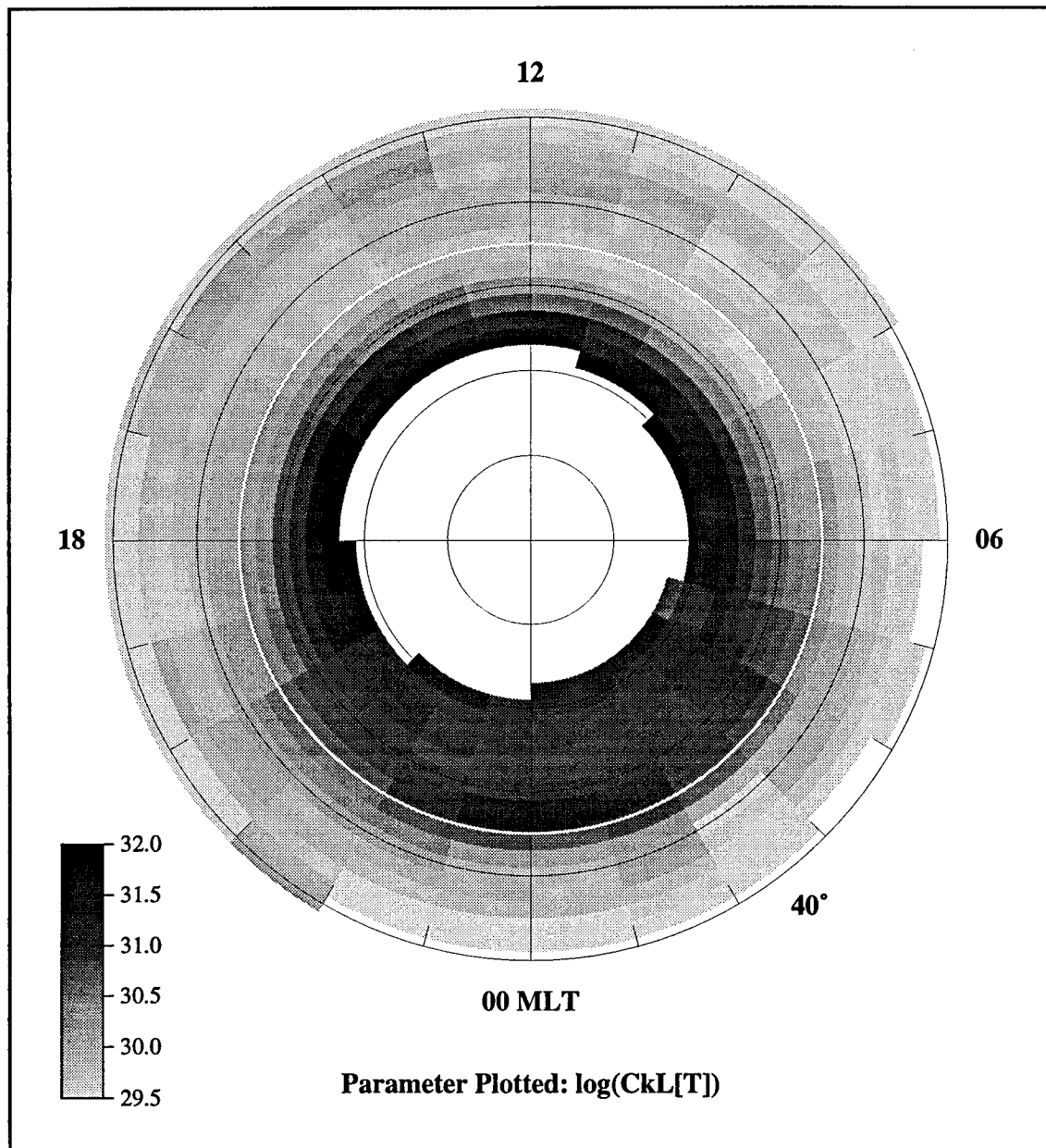


Latitude axis:  $55 + (\text{GMLAT-BNDLAT})$   
Range: 40.0 to 90.0  
Step size: 2.00

Time axis: Apex Local Time  
Step size: 1.00

Figure 26: Composite shade plot of  $\log(C_k L)$  for all  $K_p$  and  $SSN \geq 125$ . Axis definition and annotation are as in Figure 20.

**Composite -- K<sub>p</sub> Range: 0<sup>o</sup> to 1<sup>o</sup>**



Latitude axis:  $55 + (\text{GMLAT-BNDLAT})$   
Range: 40.0 to 90.0  
Step size: 2.00

Time axis: Apex Local Time  
Step size: 1.00

Figure 27: Composite shade plot of  $\log(C_k L)$  for all SSN and  $0^\circ \leq K_p \leq 1^\circ$ . Axis definition and annotation are as in Figure 20.

### Composite -- K<sub>p</sub> Range: 10 to 20

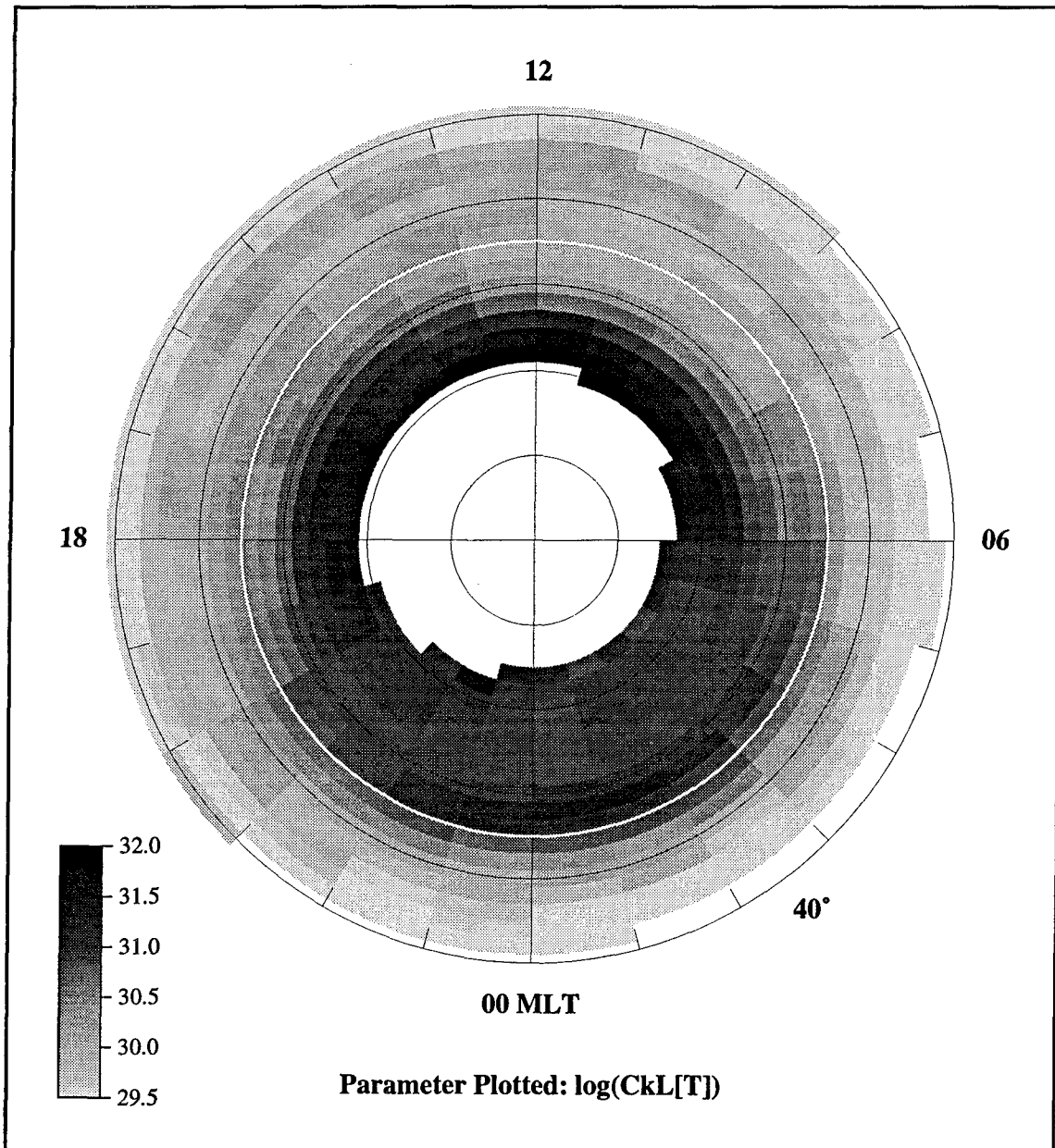
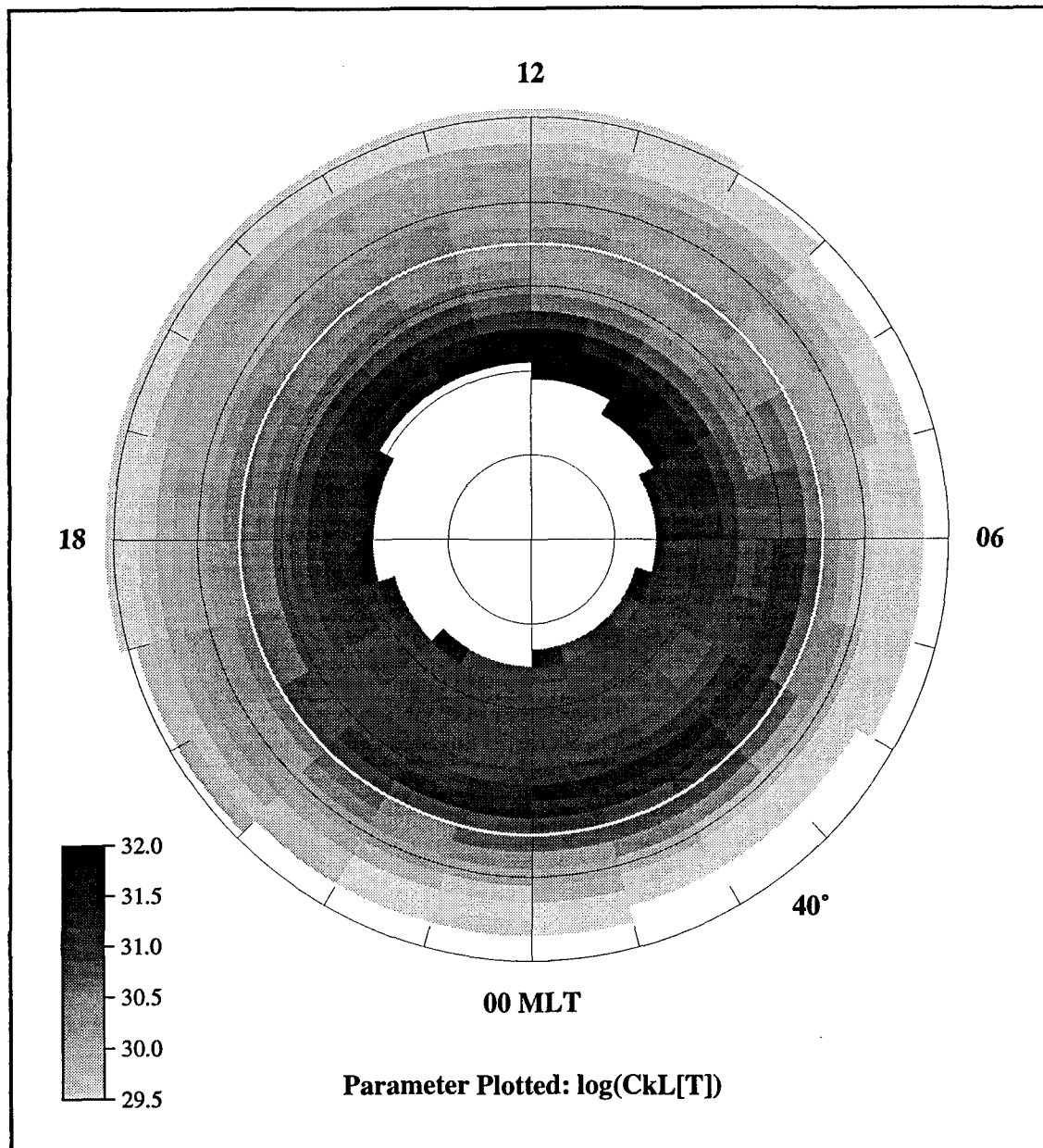


Figure 28: Composite shade plot of  $\log(C_k L)$  for all  $SSN$  and  $1^\circ \leq K_p \leq 2^\circ$ . Axis definition and annotation are as in Figure 20.

Composite -- Kp Range: 2o to 3o



Latitude axis:  $55 + (\text{GMLAT} - \text{BNDLAT})$   
Range: 40.0 to 90.0  
Step size: 2.00

Time axis: Apex Local Time  
Step size: 1.00

Figure 29: Composite shade plot of  $\log(C_k L)$  for all  $SSN$  and  $2^\circ \leq K_p \leq 3^\circ$ . Axis definition and annotation are as in Figure 20.

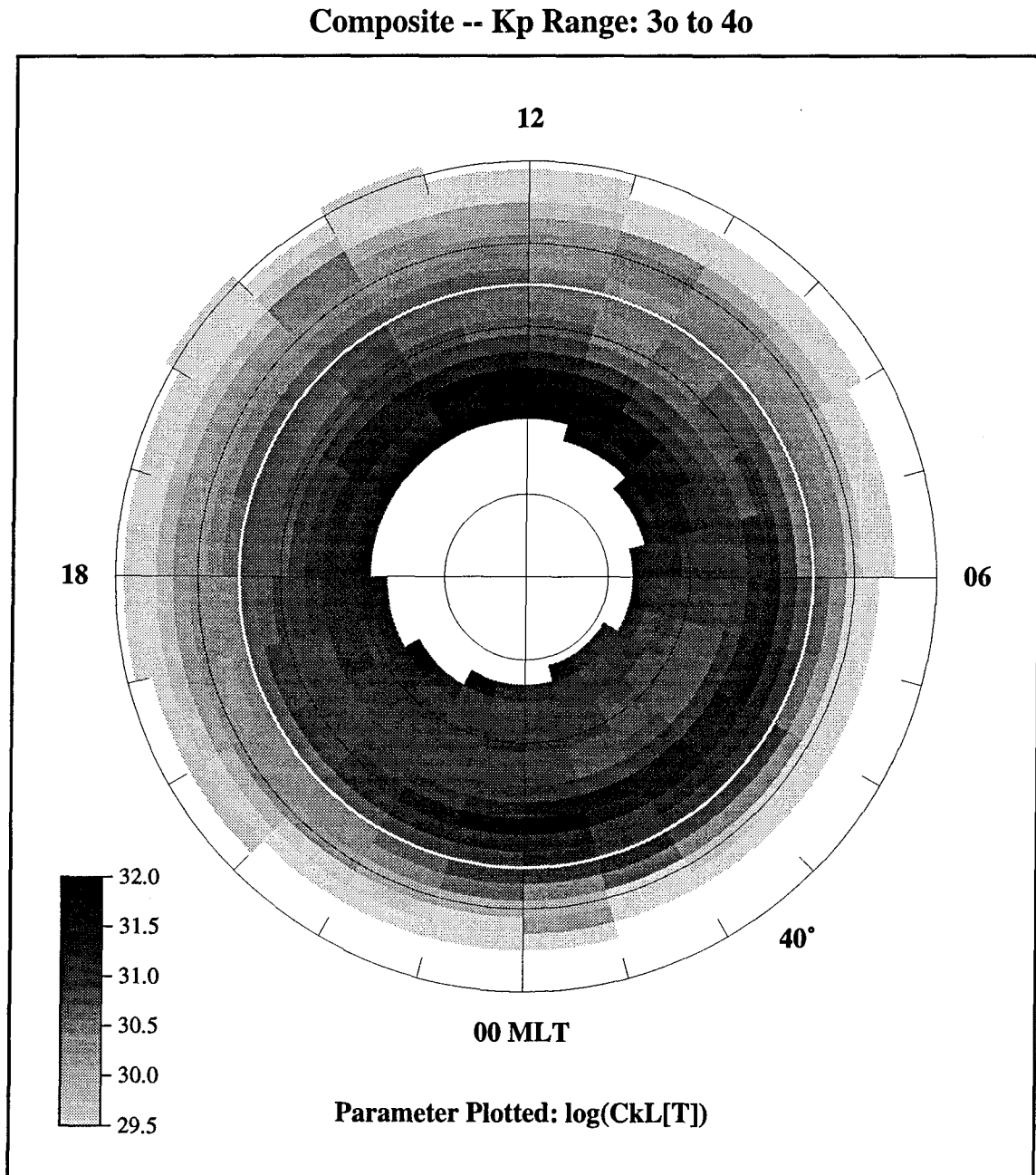
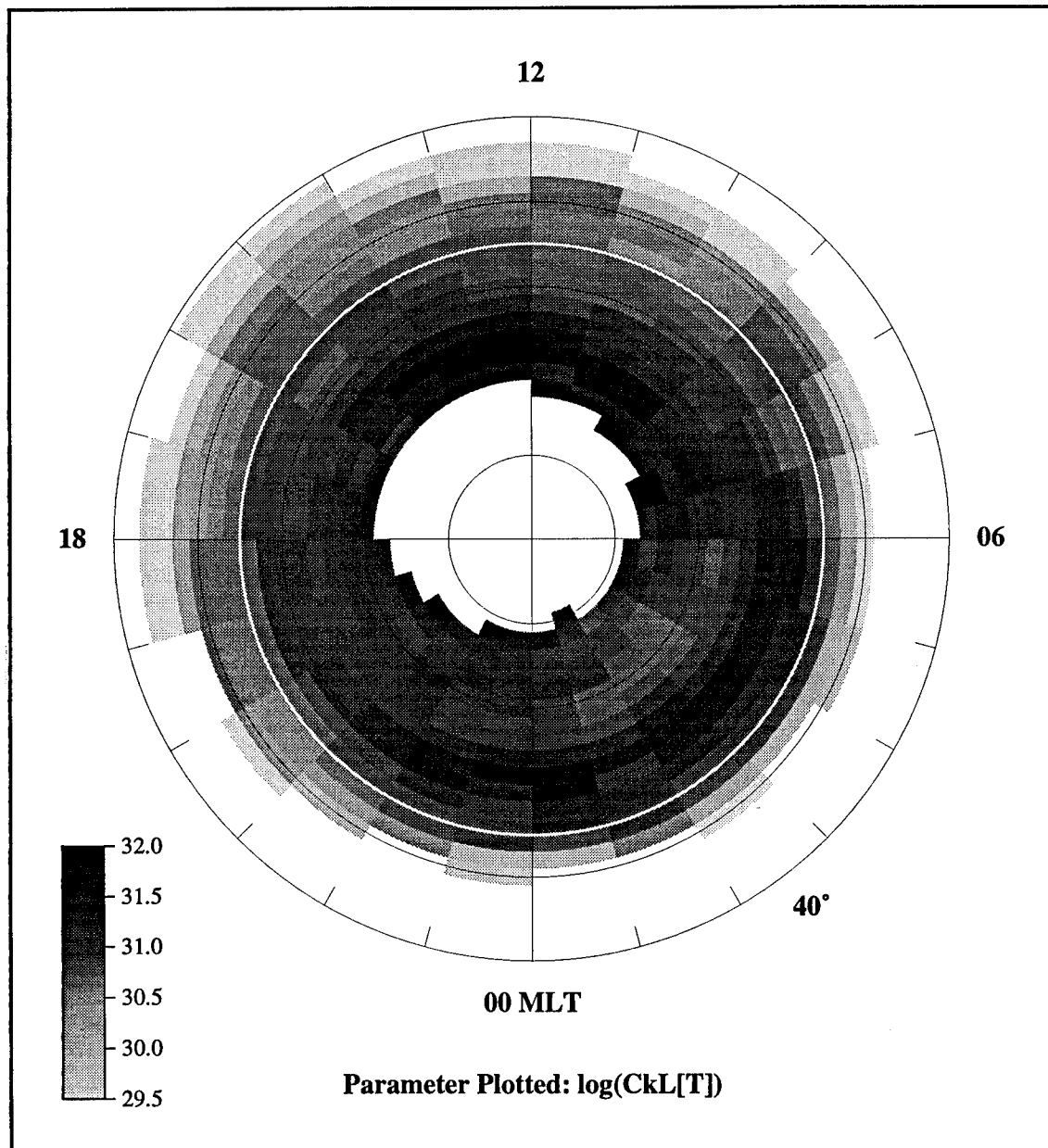


Figure 30: Composite shade plot of  $\log(C_k L)$  for all  $SSN$  and  $30^\circ \leq K_p \leq 40^\circ$ . Axis definition and annotation are as in Figure 20.

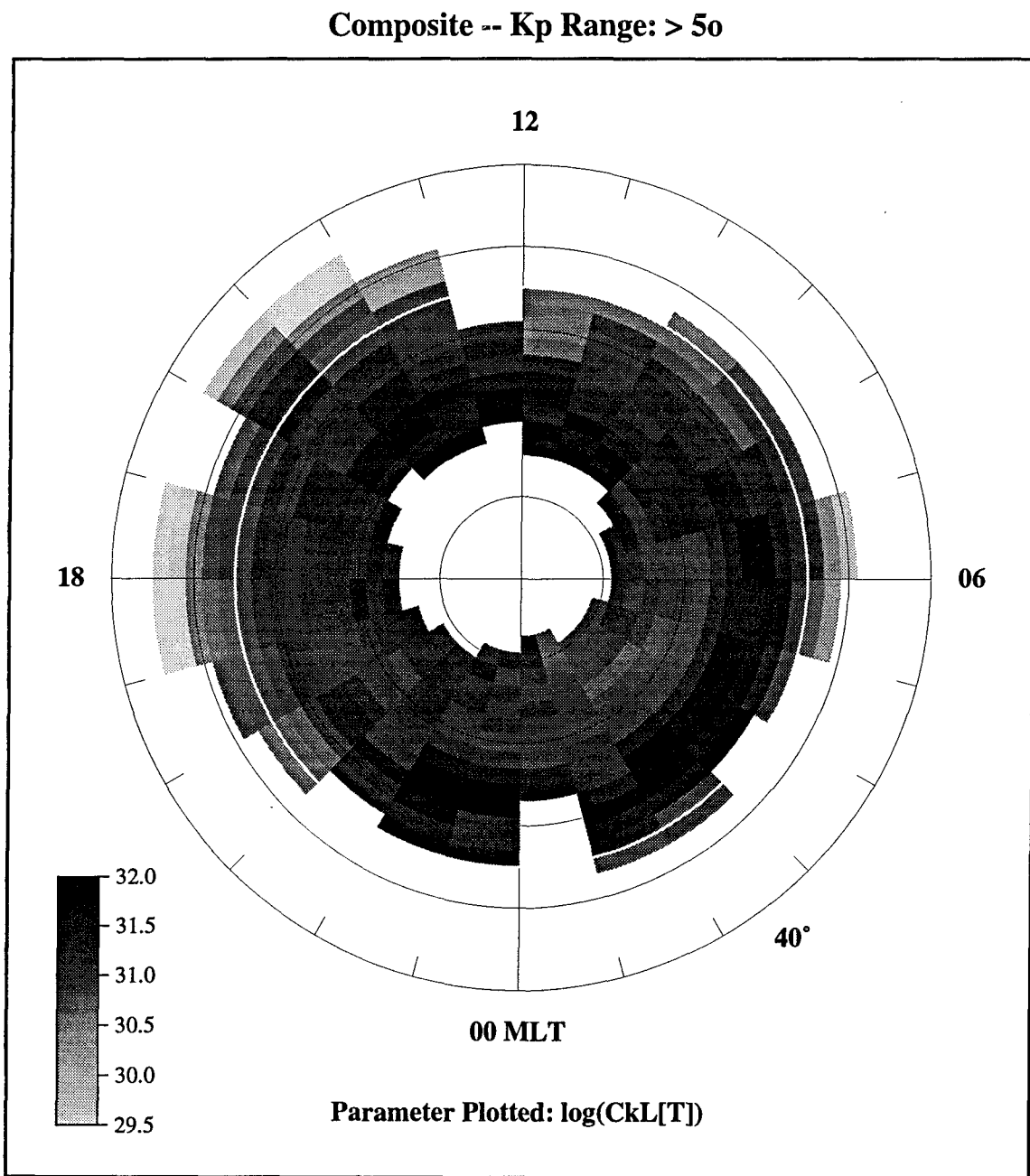
**Composite -- K<sub>p</sub> Range: 40 to 50**



Latitude axis:  $55 + (\text{GMLAT-BNDLAT})$   
Range: 40.0 to 90.0  
Step size: 2.00

Time axis: Apex Local Time  
Step size: 1.00

Figure 31: Composite shade plot of  $\log(C_k L)$  for all  $SSN$  and  $40^\circ \leq K_p \leq 50^\circ$ . Axis definition and annotation are as in Figure 20.



Latitude axis: 55 + (GMLAT-BNDLAT)  
 Range: 40.0 to 90.0  
 Step size: 2.00

Time axis: Apex Local Time  
 Step size: 1.00

Figure 32: Composite shade plot of  $\log(C_k L)$  for all  $SSN$  and  $K_p \geq 50$ . Axis definition and annotation are as in Figure 20.

## Appendix B. Results of High-Latitude $\log(C_k L)$ Modeling.

The figures in this appendix shows the results of the fitting process described in Section 3.2. Each pair of figures corresponds to one of the 13 data sets shown in Appendix A, and are presented in the same order as the figures in Appendix A. These figures show the variation of  $\log(C_k L)$  as a function of the distance from the auroral precipitation boundary ( $\Lambda$ ) from the data sets (light solid curves), from the new high-latitude model (heavy solid curves), and from the WBMOD Version 12.02 high-latitude model (heavy dashed curves). This variation is shown for six geomagnetic (apex) local time sectors: 0000 to 0400 GMLT, 0400 to 0800 GMLT, 0800 to 1200 GMLT, 1200 to 1600 GMLT, 1600 to 2000 GMLT, and 2000 to 2400 GMLT. The vertical dotted line in each plot indicates the location of the auroral precipitation boundary ( $\Lambda = 0$ ).

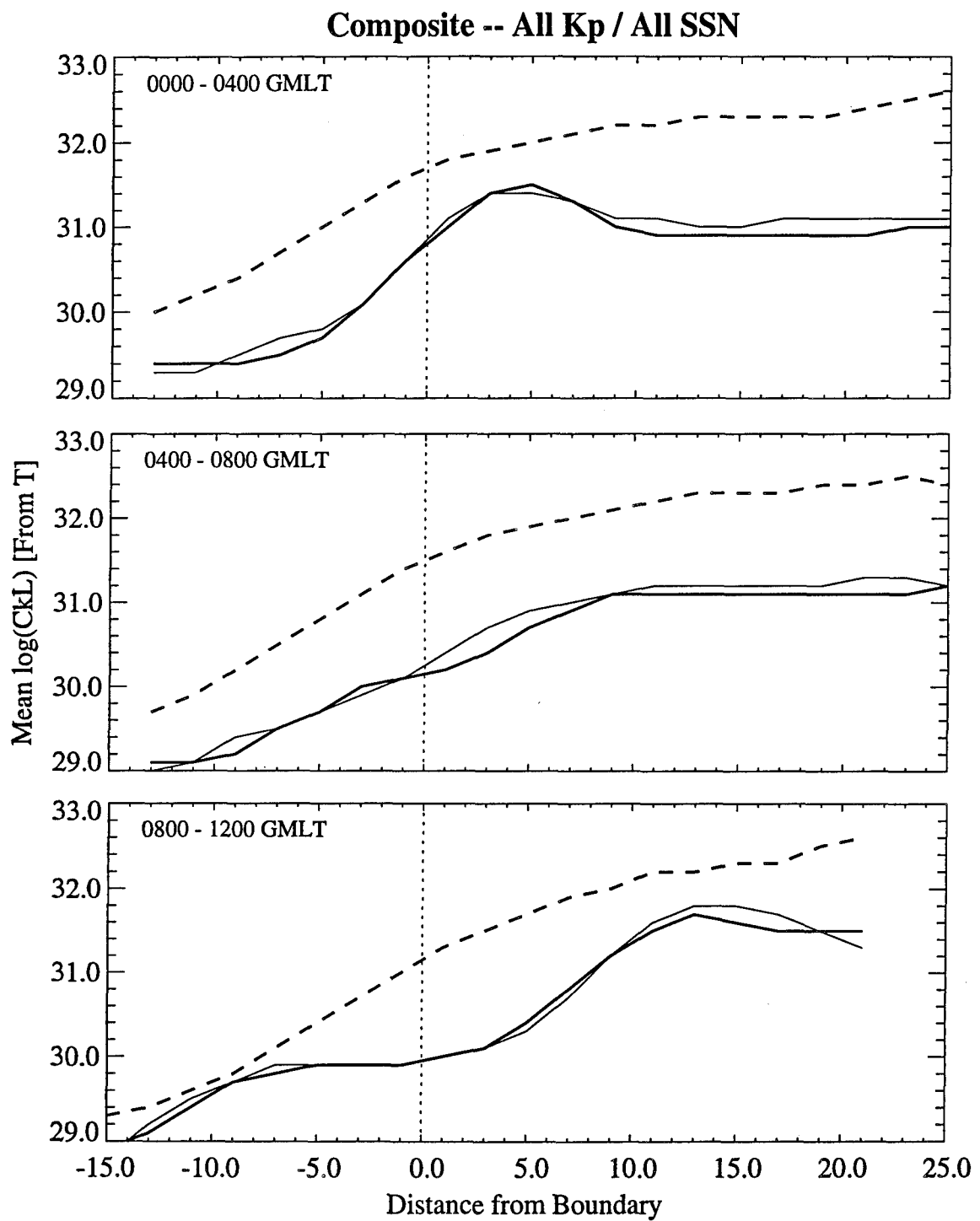


Figure 33: Comparison of WBMOD Version 12.02 (heavy dashed line) and SCINTMOD Version 1.0 (heavy solid line) to composite observations of  $\log(C_k L)$  (light solid line) for all SSN and all  $K_p$ .

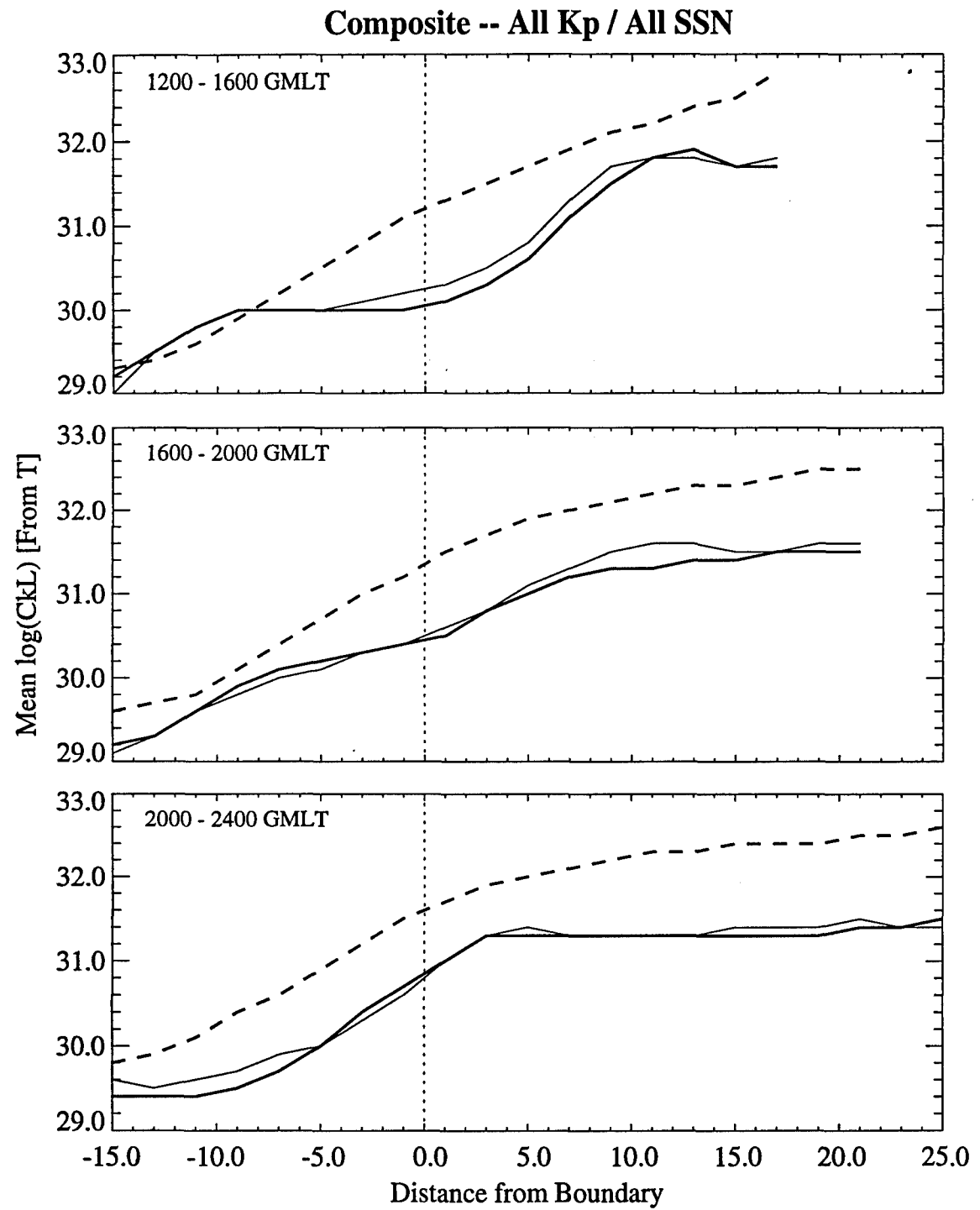


Figure 34: Continuation of comparison in Figure 33.

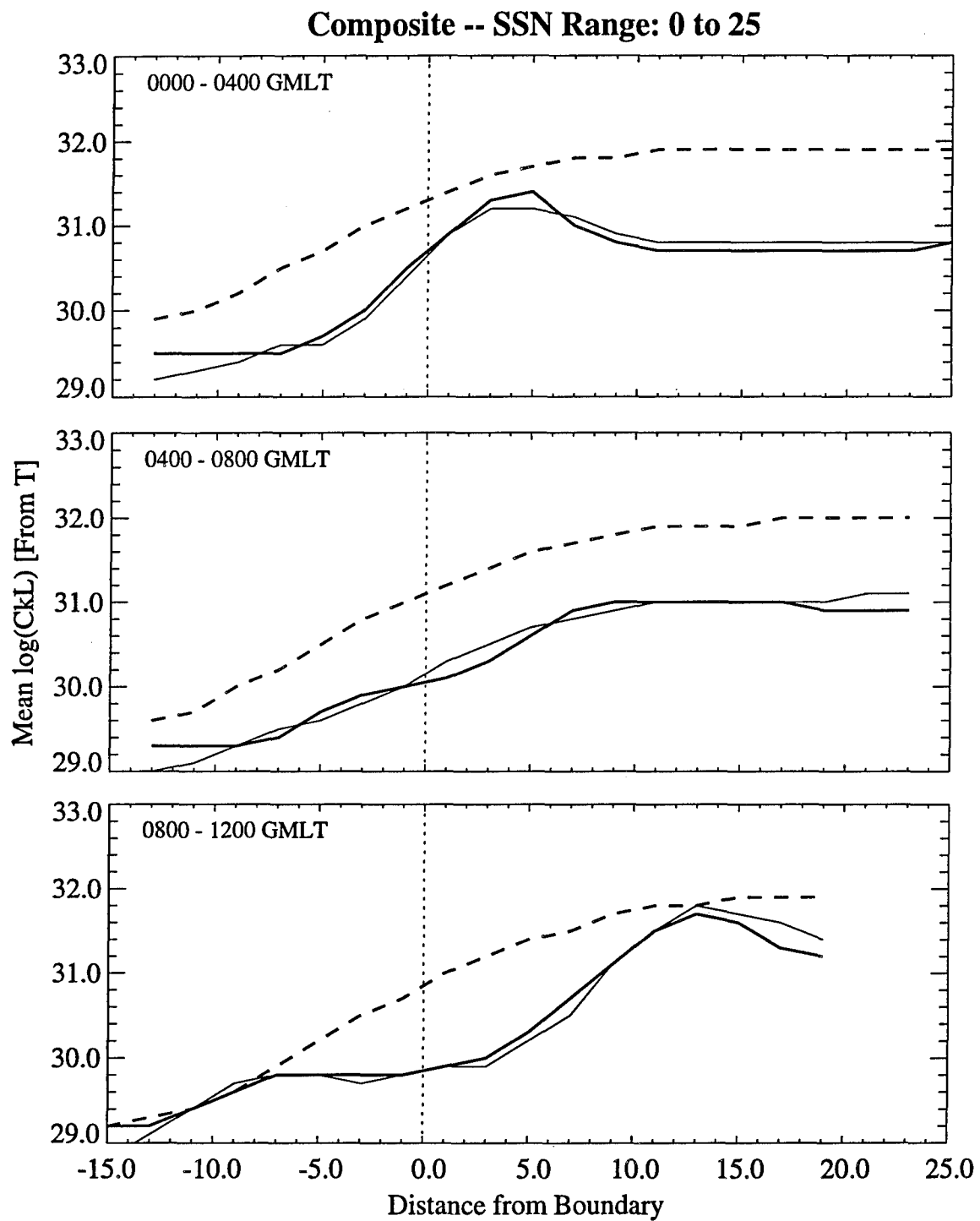


Figure 35: Comparison of WBMOD Version 12.02 (heavy dashed line) and SCINTMOD Version 1.0 (heavy solid line) to composite observations of  $\log(C_k L)$  (light solid line) for all  $K_p$  and  $0 \leq \text{SSN} \leq 25$ .

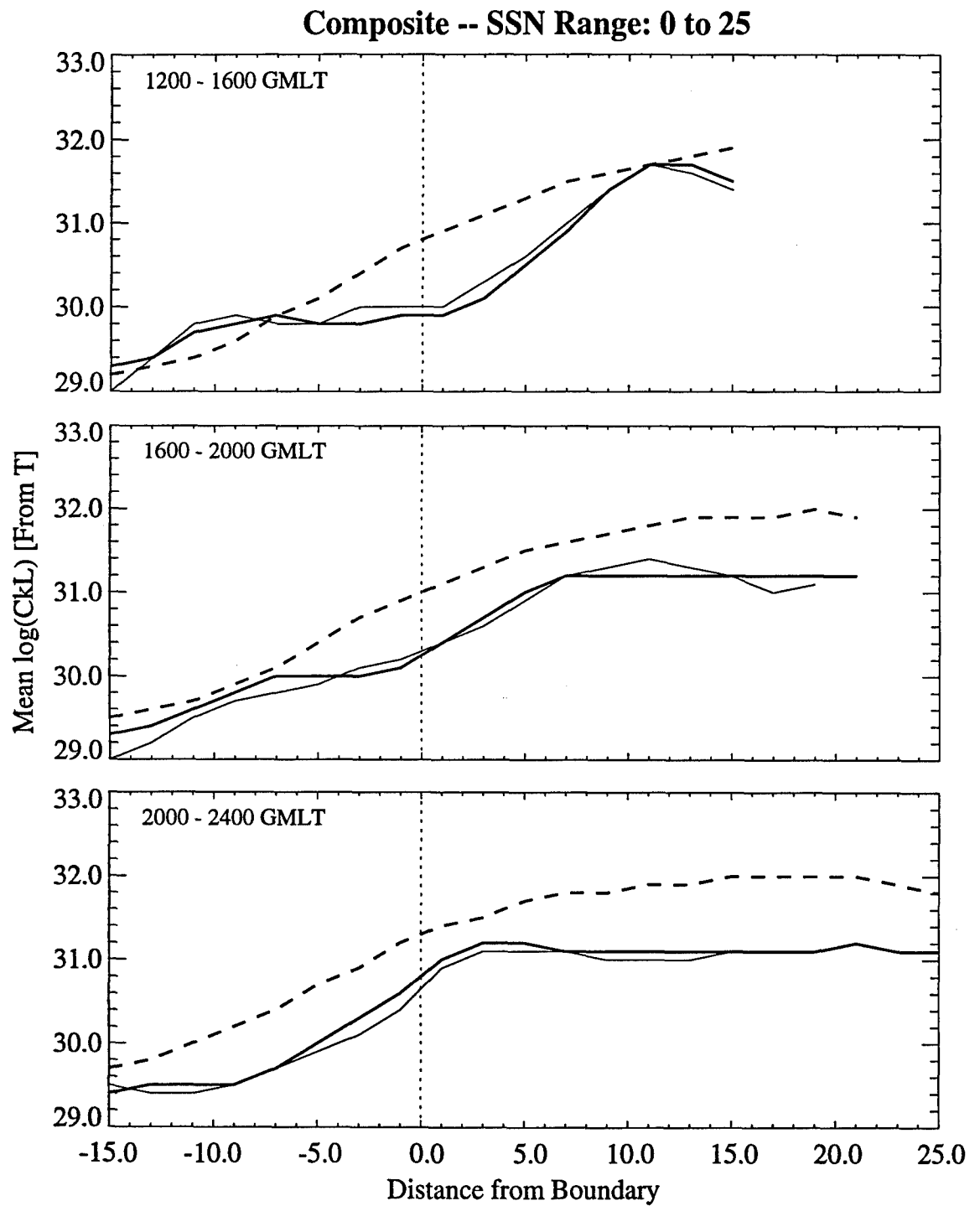


Figure 36: Continuation of comparison in Figure 35.

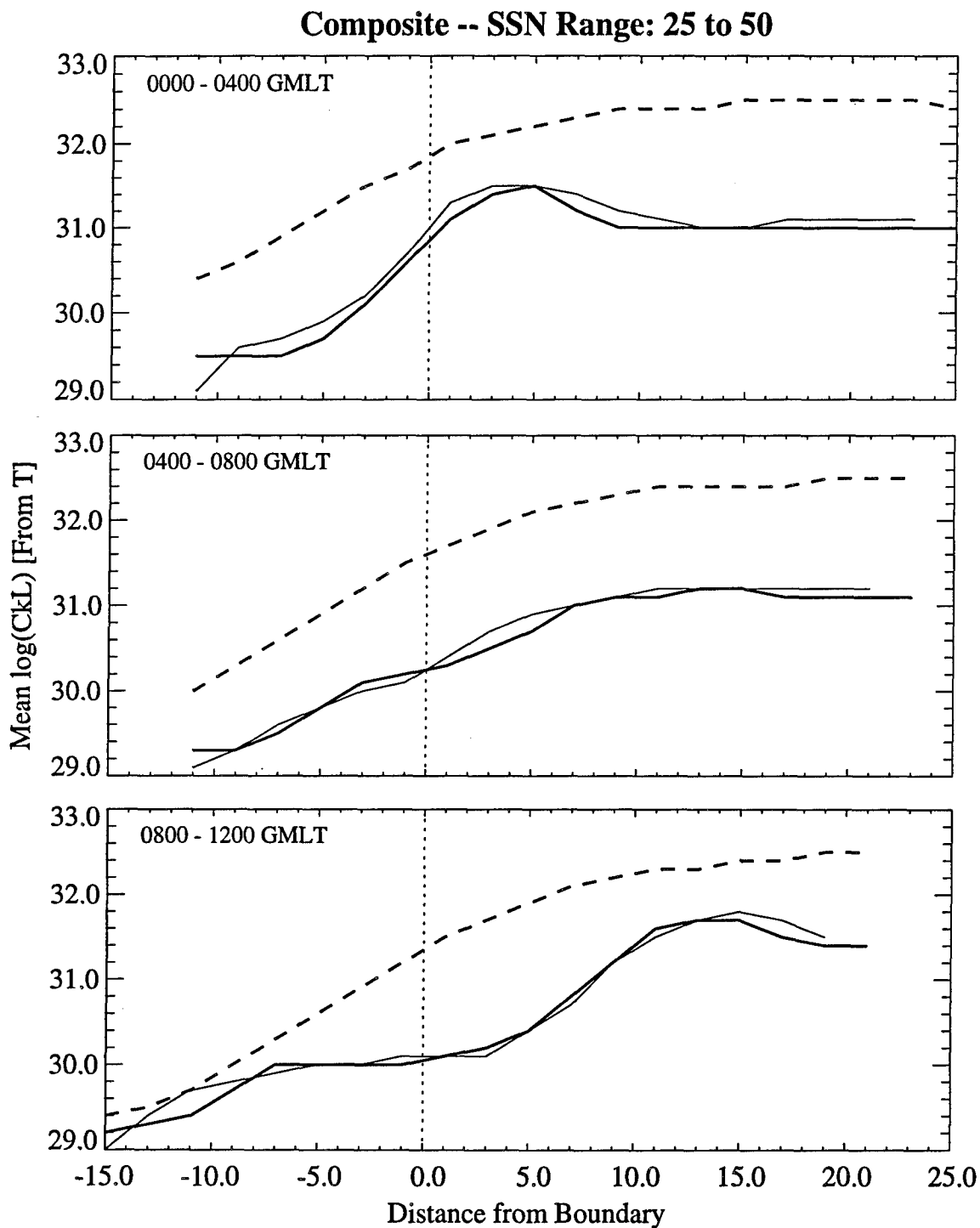


Figure 37: Comparison of WBMOD Version 12.02 (heavy dashed line) and SCINTMOD Version 1.0 (heavy solid line) to composite observations of  $\log(C_k L)$  (light solid line) for all  $K_p$  and  $25 \leq \text{SSN} \leq 50$ .

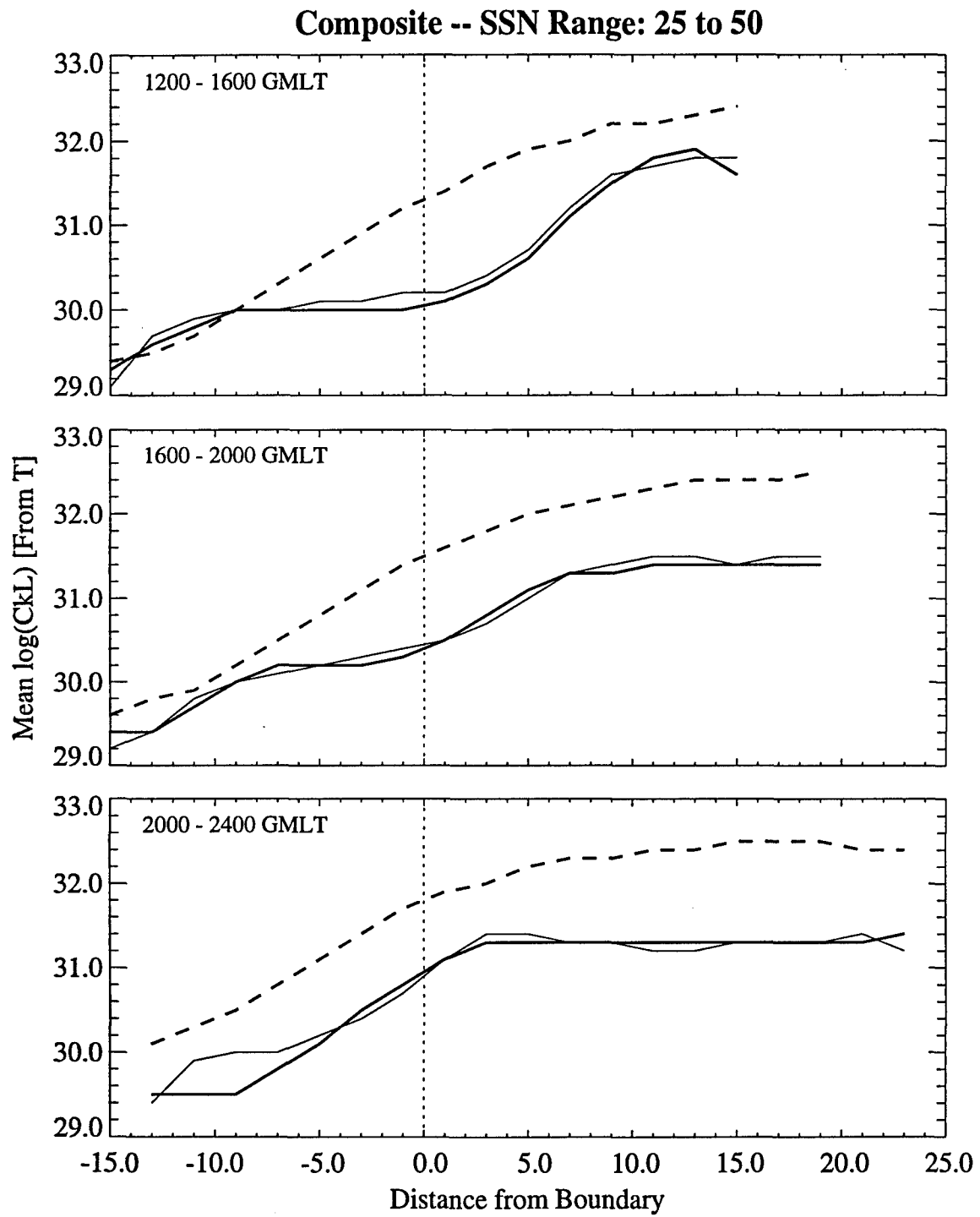


Figure 38: Continuation of comparison in Figure 37.

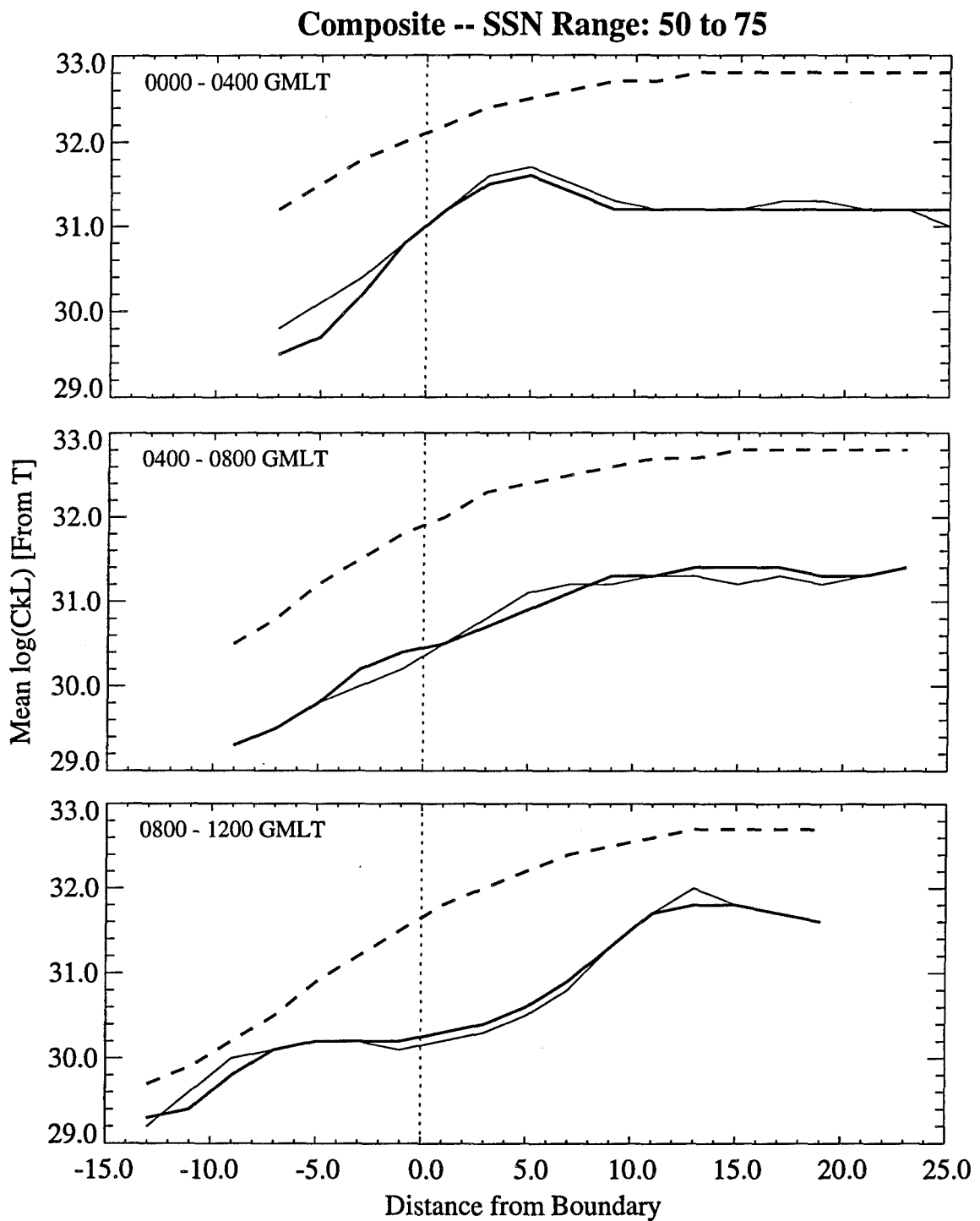


Figure 39: Comparison of WBMOD Version 12.02 (heavy dashed line) and SCINTMOD Version 1.0 (heavy solid line) to composite observations of  $\log(C_k L)$  (light solid line) for all  $K_p$  and  $50 \leq \text{SSN} \leq 75$ .

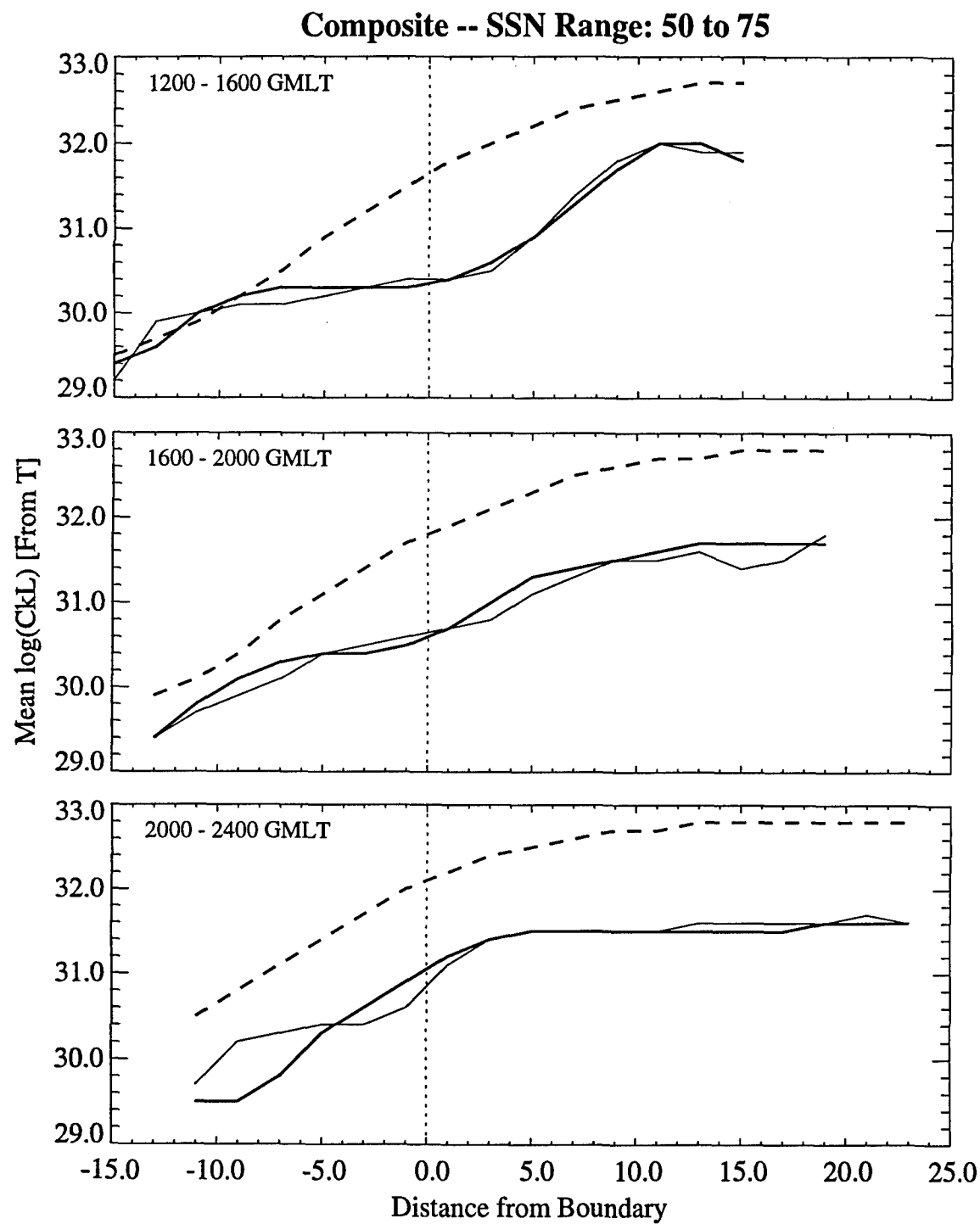


Figure 40: Continuation of comparison in Figure 39.

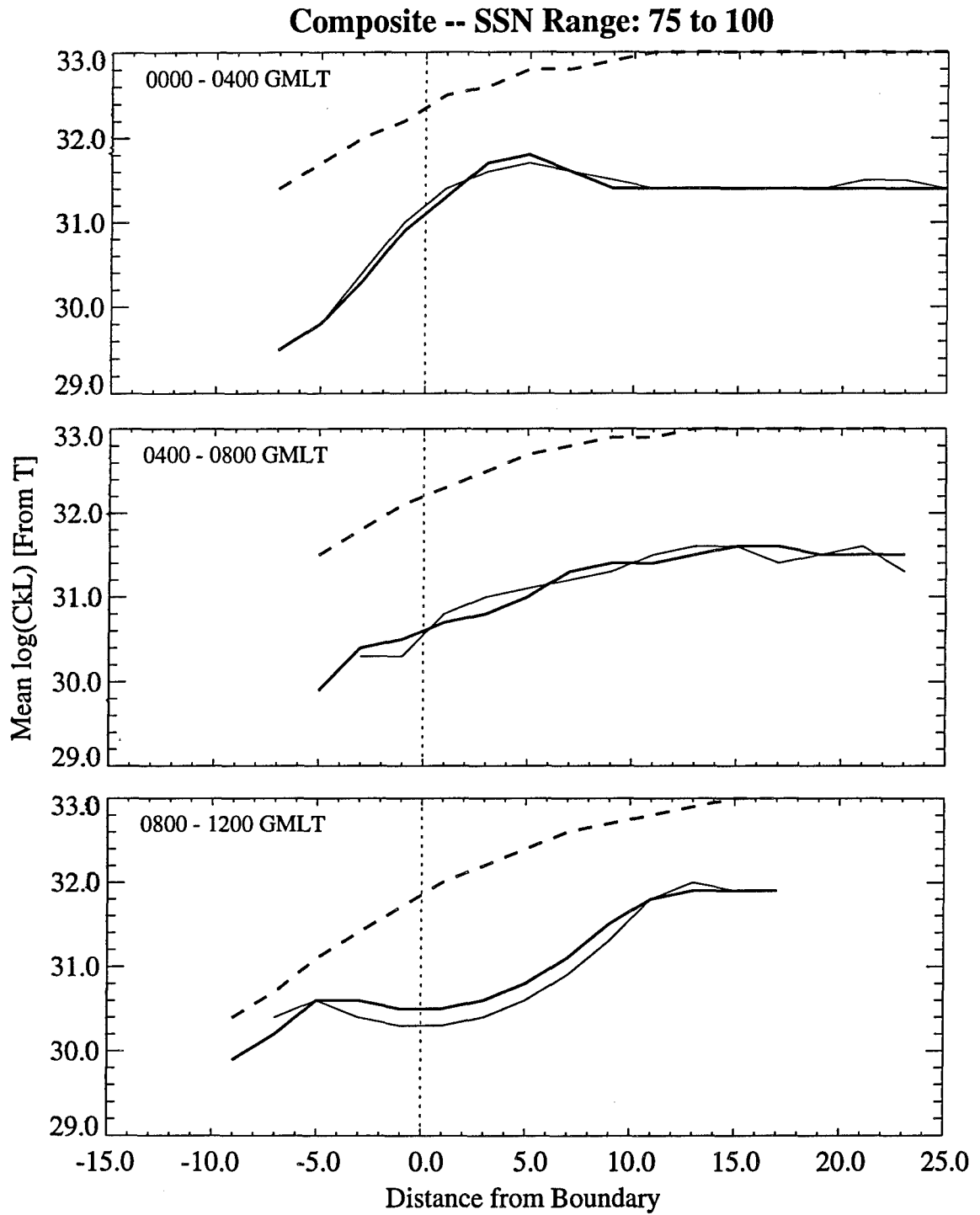


Figure 41: Comparison of WBMOD Version 12.02 (heavy dashed line) and SCINTMOD Version 1.0 (heavy solid line) to composite observations of  $\log(C_k L)$  (light solid line) for all  $K_p$  and  $75 \leq \text{SSN} \leq 100$ .

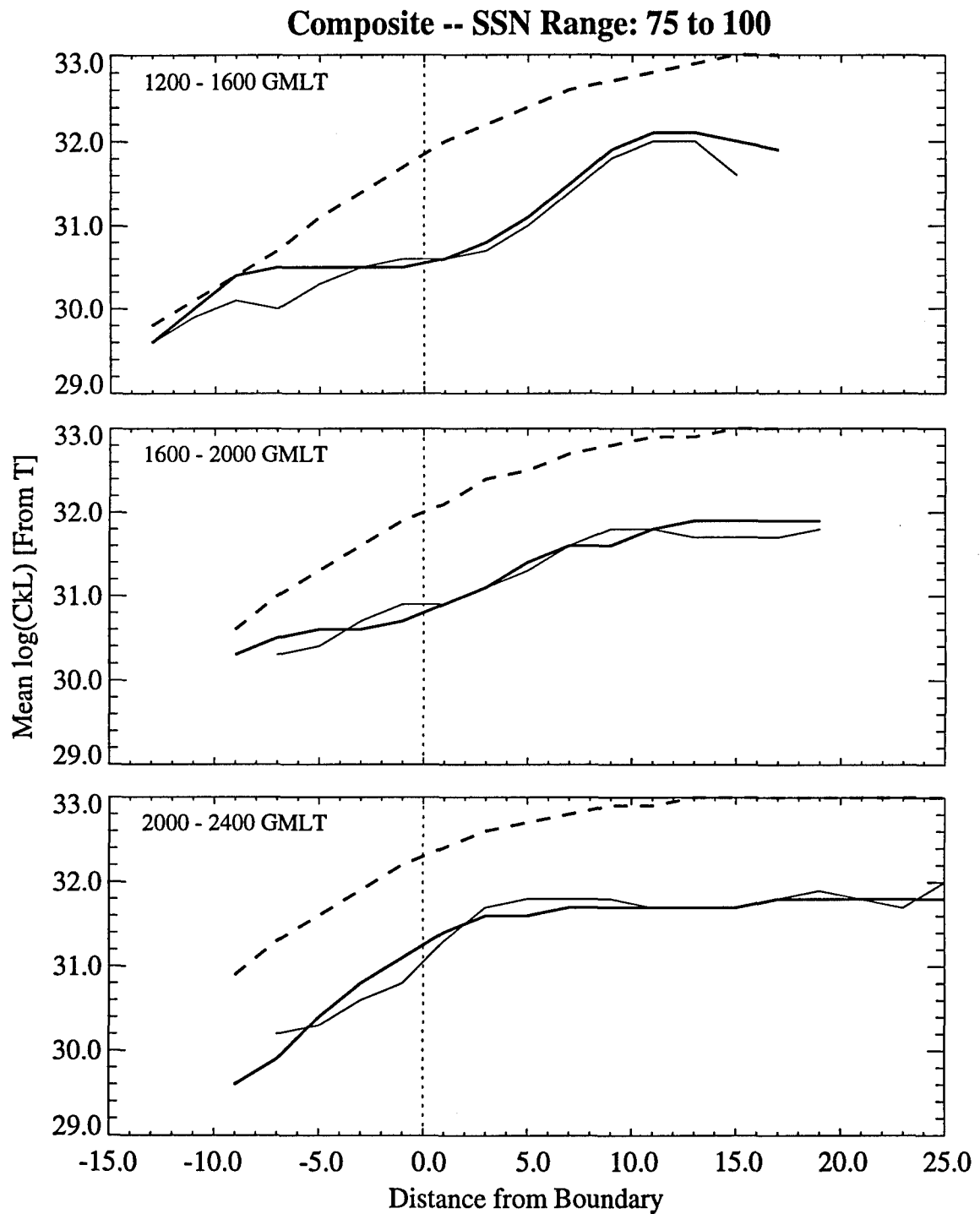


Figure 42: Continuation of comparison in Figure 41.

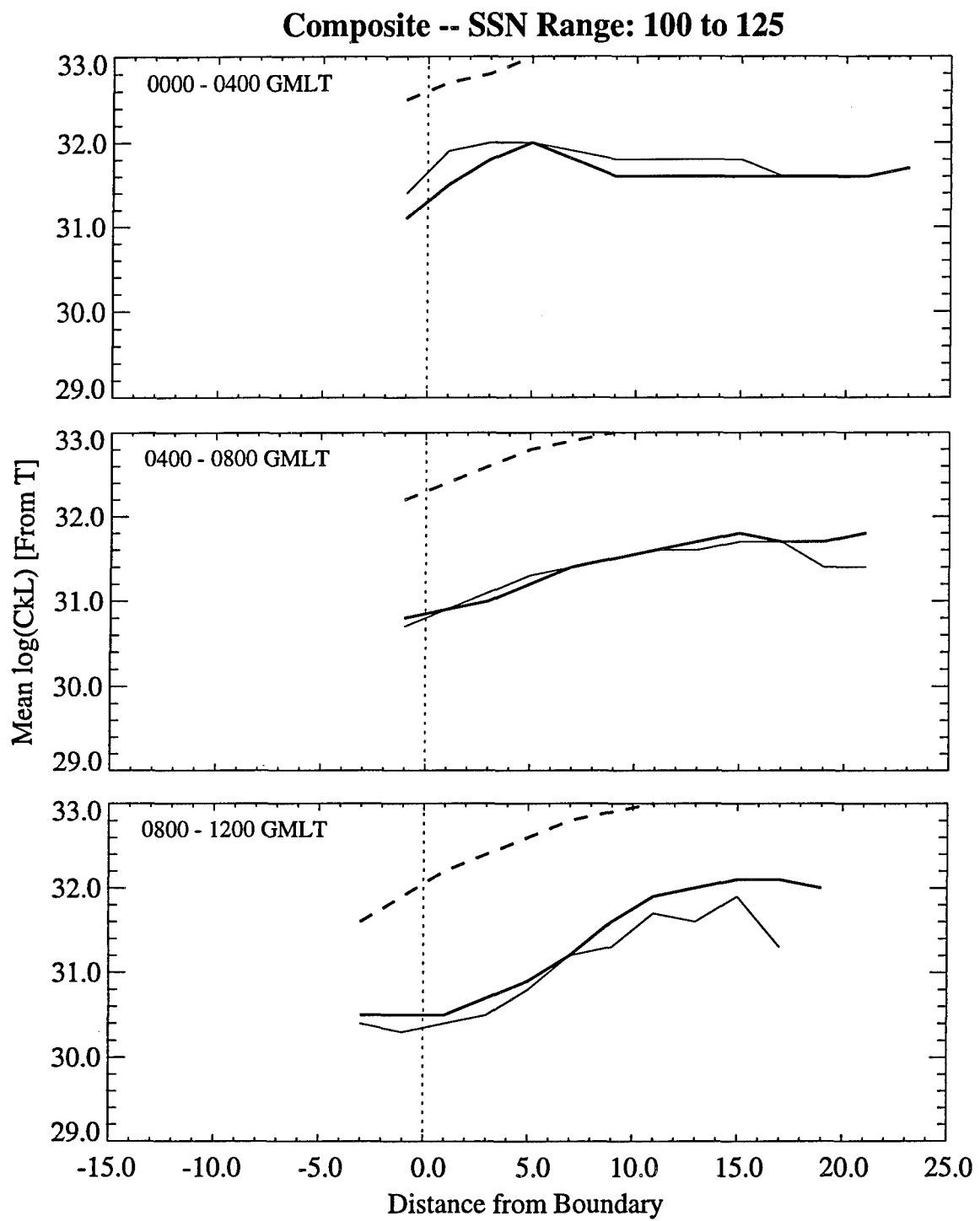


Figure 43: Comparison of WBMOD Version 12.02 (heavy dashed line) and SCINTMOD Version 1.0 (heavy solid line) to composite observations of  $\log(C_k L)$  (light solid line) for all  $K_p$  and  $100 \leq \text{SSN} \leq 125$ .

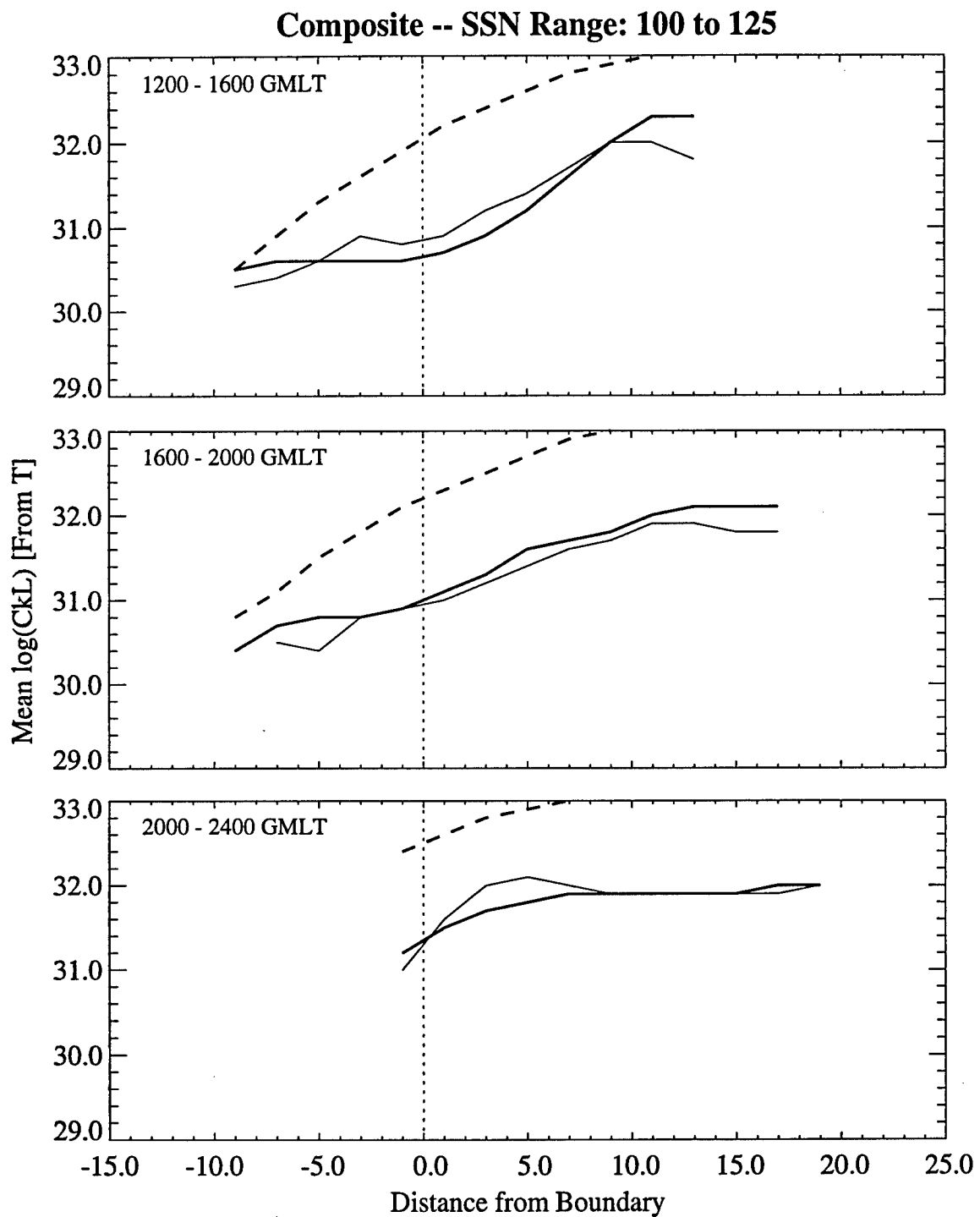


Figure 44: Continuation of comparison in Figure 43.

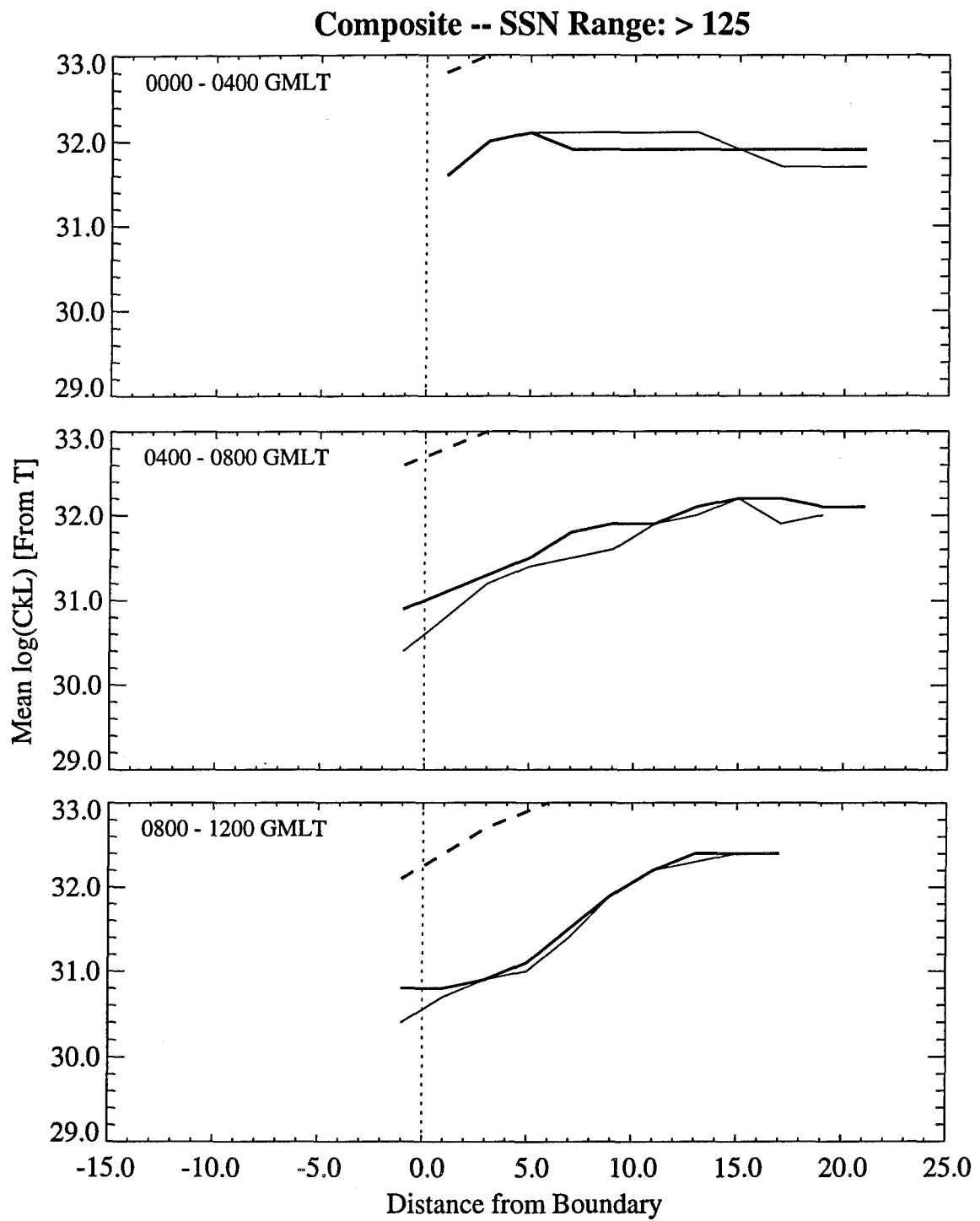


Figure 45: Comparison of WBMOD Version 12.02 (heavy dashed line) and SCINTMOD Version 1.0 (heavy solid line) to composite observations of  $\log(C_k L)$  (light solid line) for all  $K_p$  and  $SSN \geq 25$ .

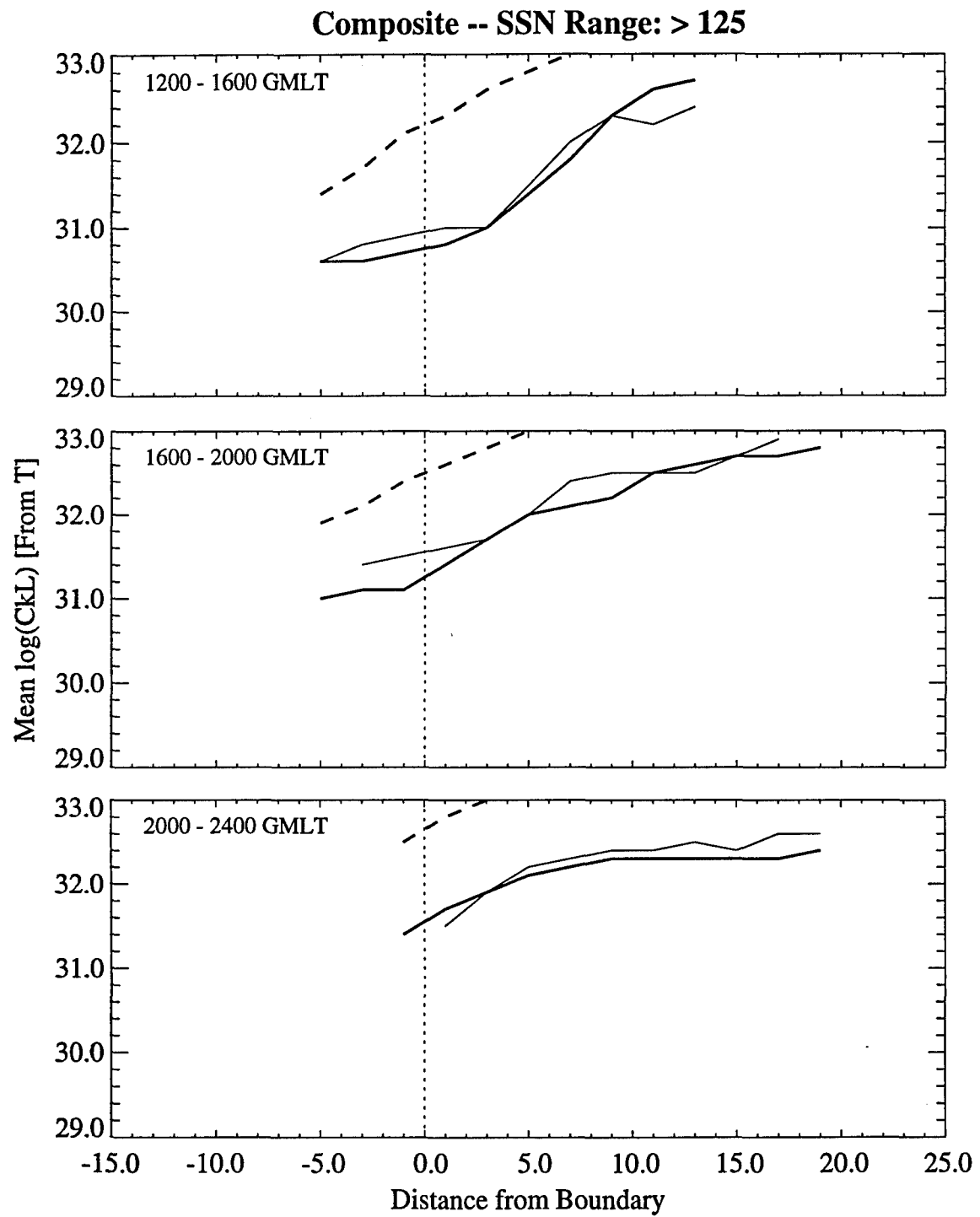


Figure 46: Continuation of comparison in Figure 45.

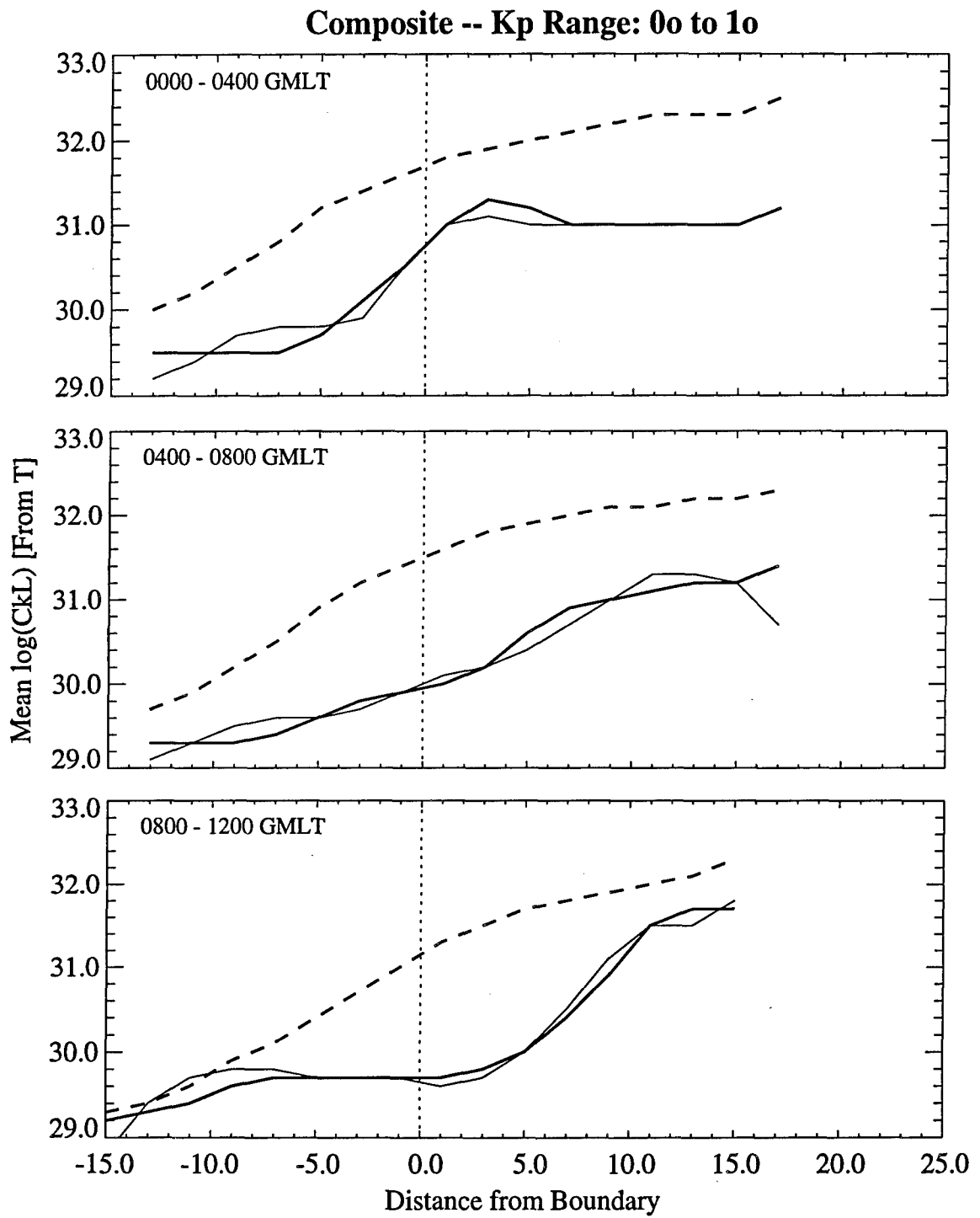


Figure 47: Comparison of WBMOD Version 12.02 (heavy dashed line) and SCINTMOD Version 1.0 (heavy solid line) to composite observations of  $\log(C_k L)$  (light solid line) for all SSN and  $0^\circ \leq K_p \leq 1^\circ$ .

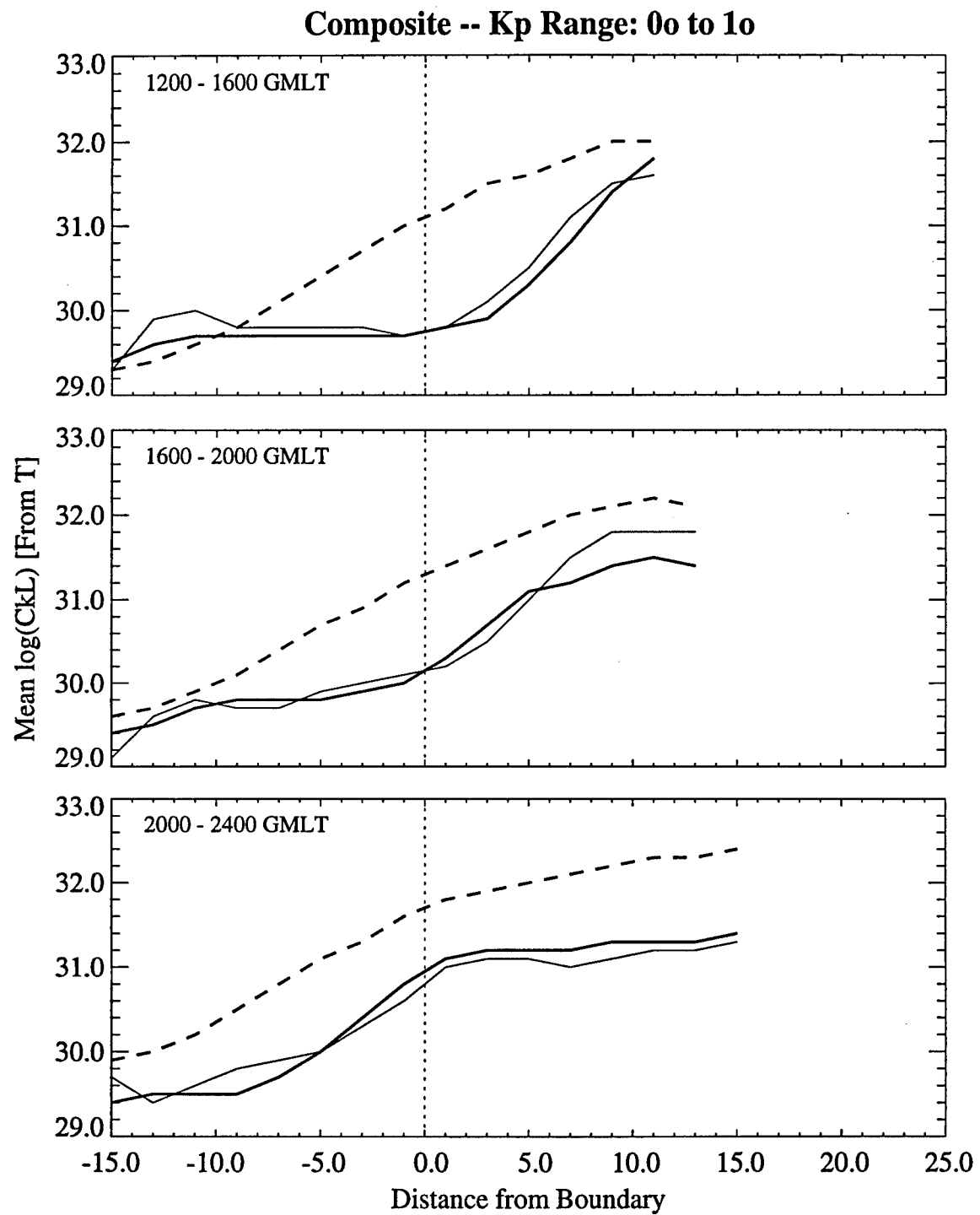


Figure 48: Continuation of comparison in Figure 47.

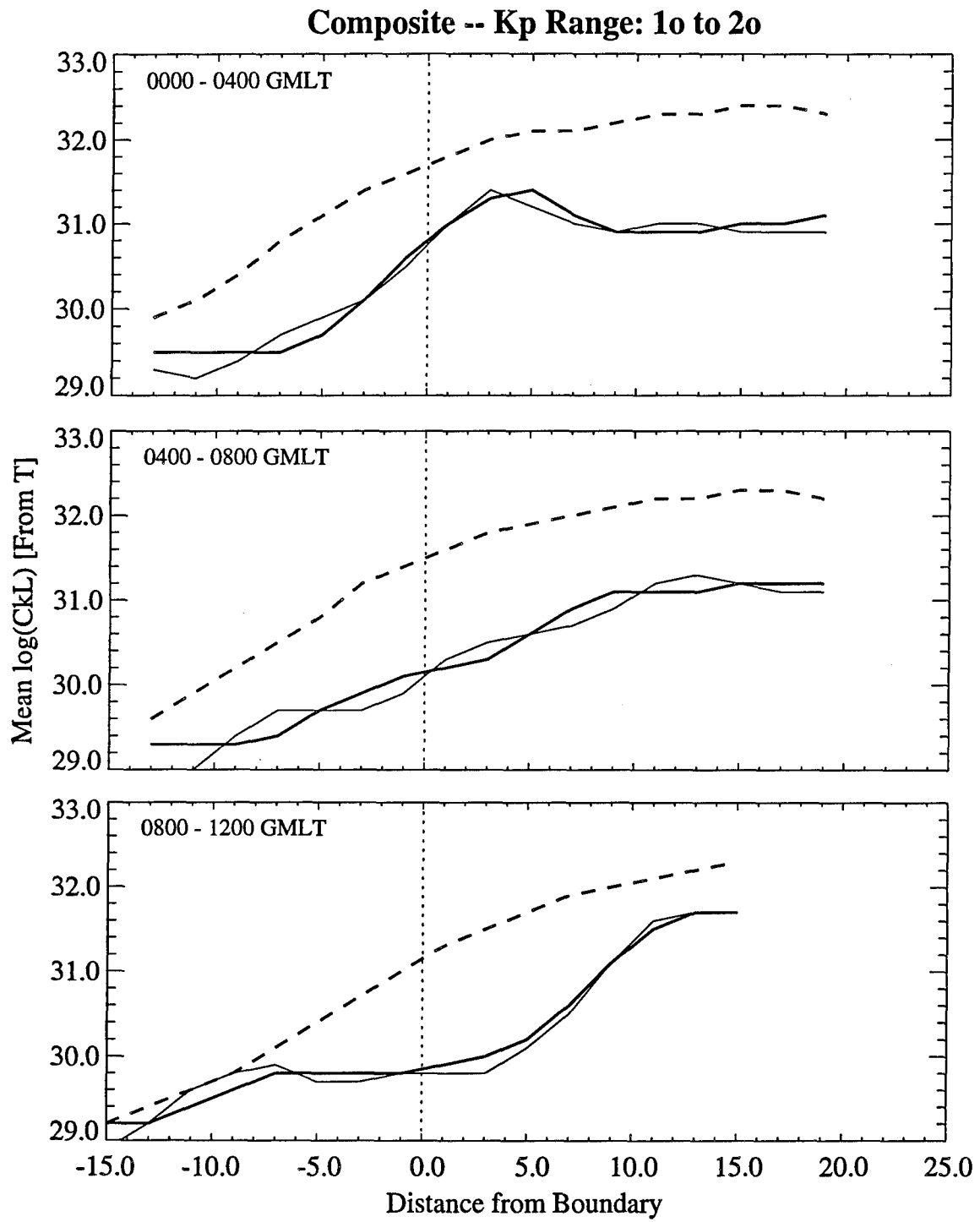


Figure 49: Comparison of WBMOD Version 12.02 (heavy dashed line) and SCINTMOD Version 1.0 (heavy solid line) to composite observations of  $\log(C_k L)$  (light solid line) for all SSN and  $10 \leq K_p \leq 20$ .

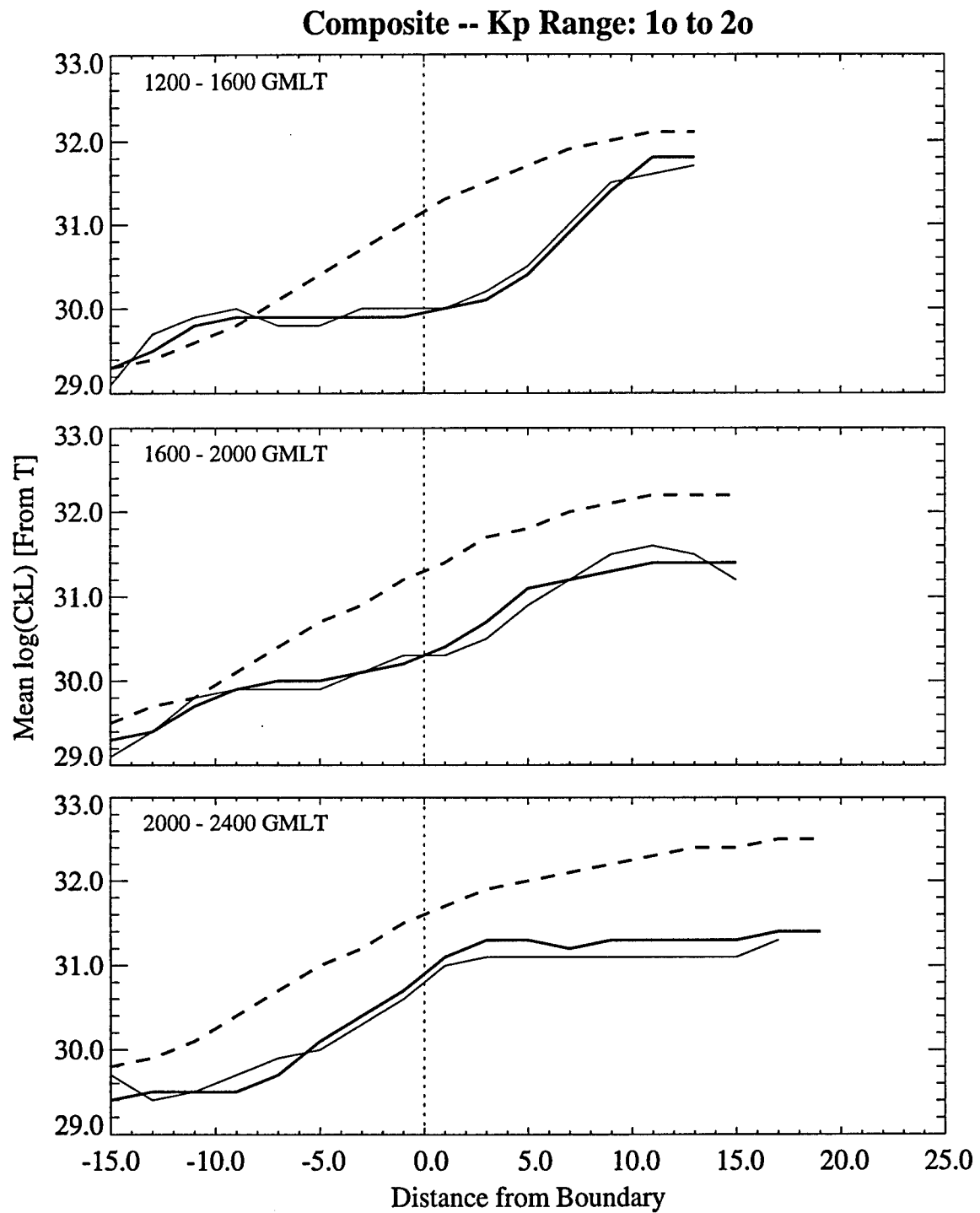


Figure 50: Continuation of comparison in Figure 49.

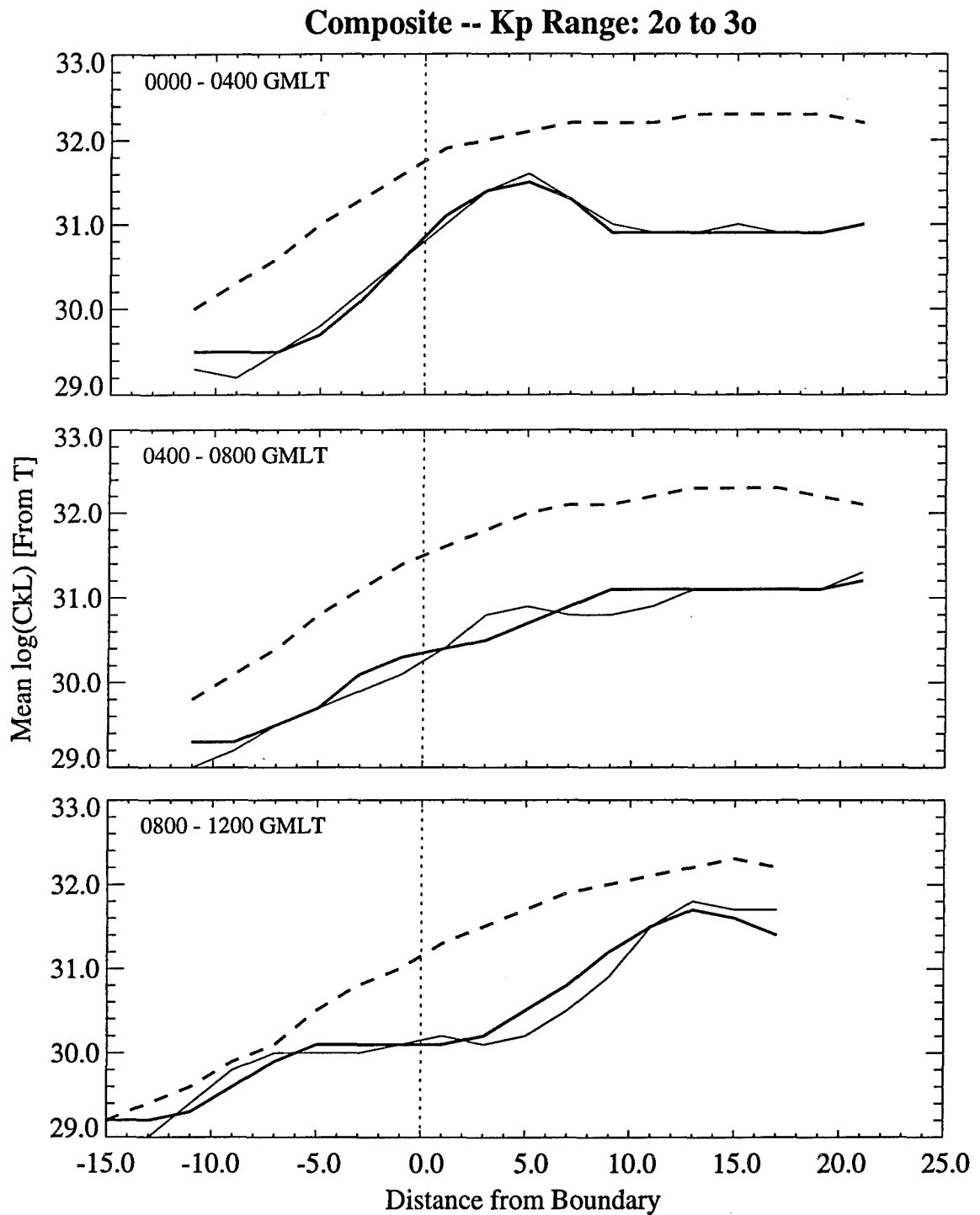


Figure 51: Comparison of WBMOD Version 12.02 (heavy dashed line) and SCINTMOD Version 1.0 (heavy solid line) to composite observations of  $\log(C_k L)$  (light solid line) for all SSN and  $2^{\circ} \leq K_p \leq 3^{\circ}$ .

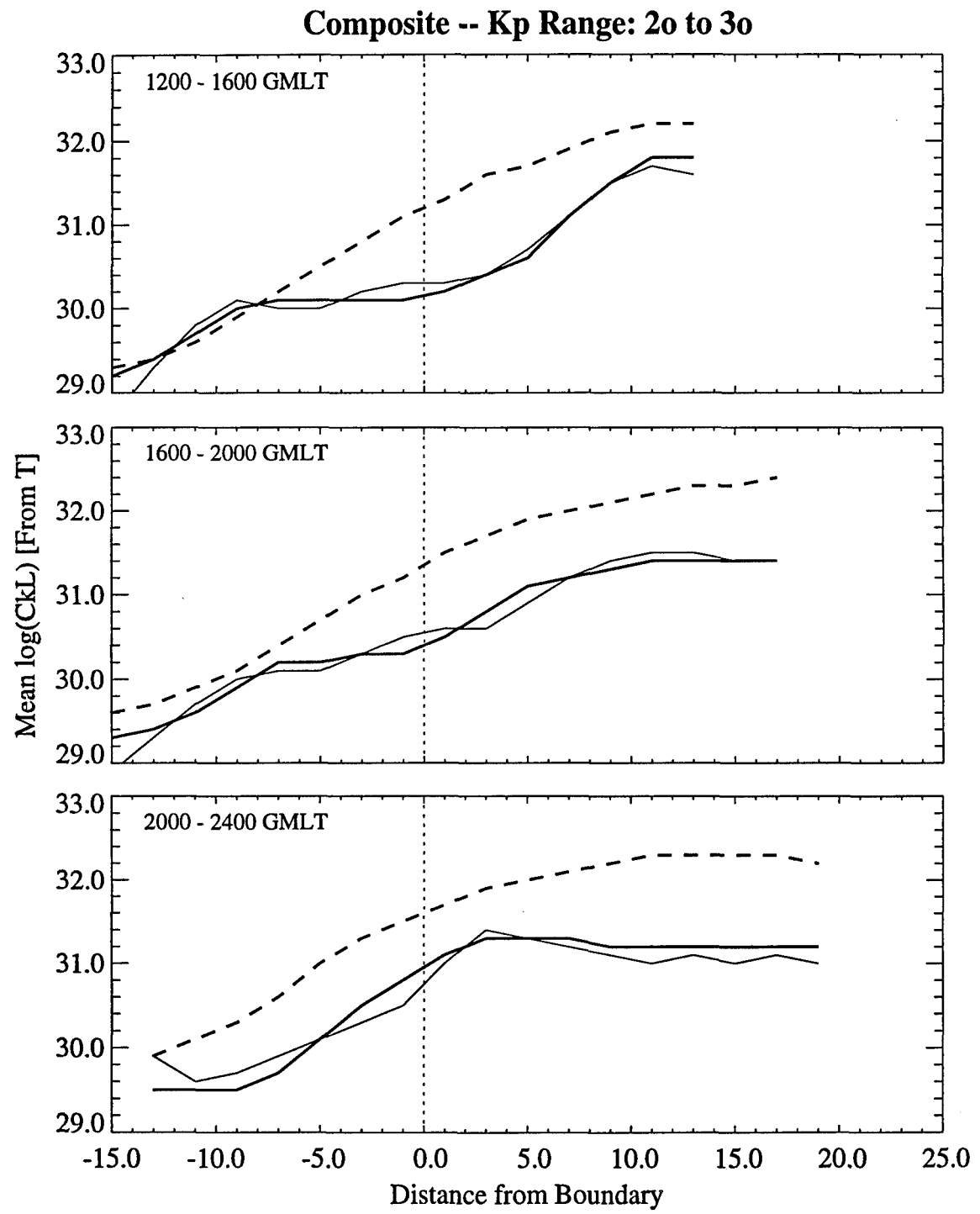


Figure 52: Continuation of comparison in Figure 51.

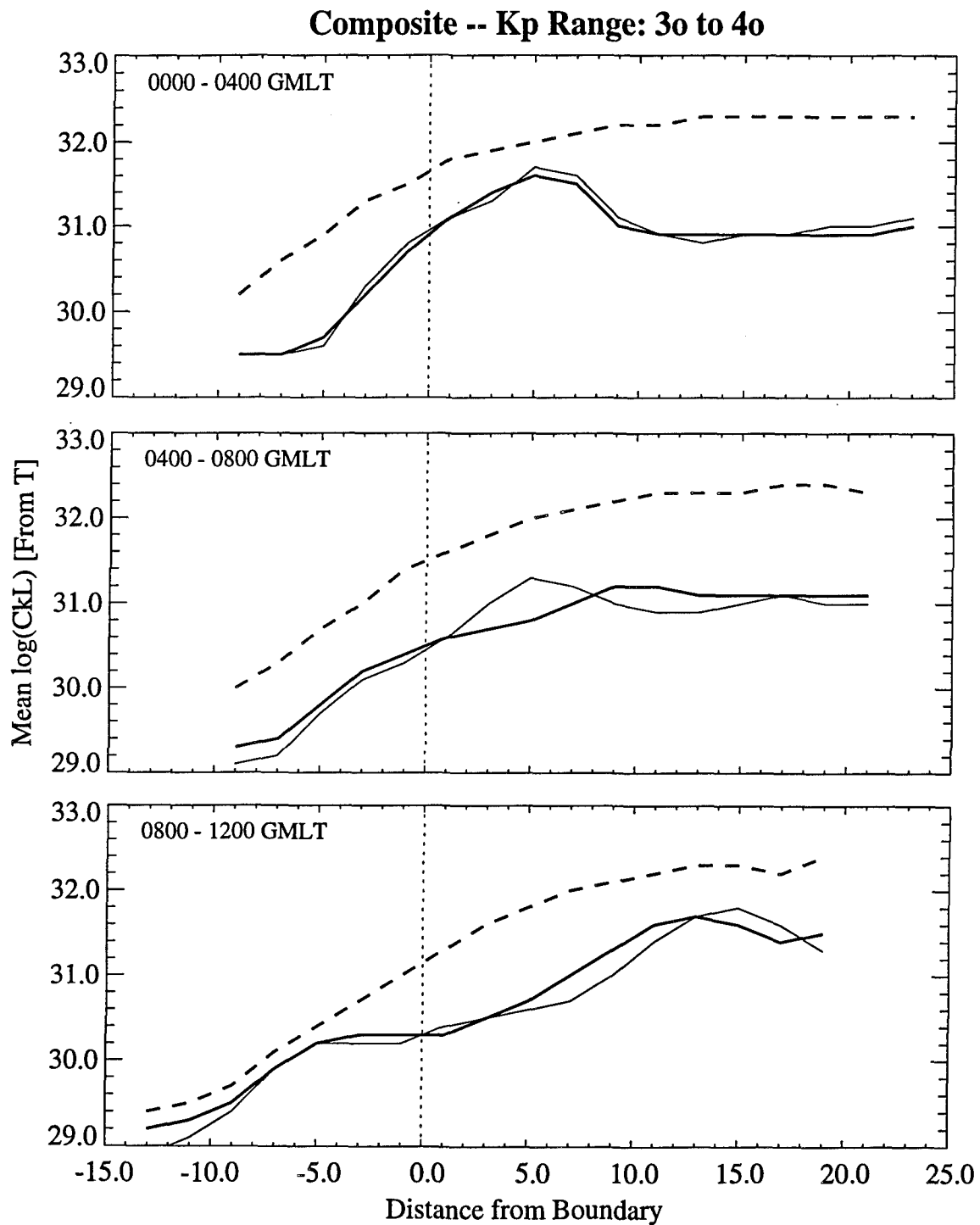


Figure 53: Comparison of WBMOD Version 12.02 (heavy dashed line) and SCINTMOD Version 1.0 (heavy solid line) to composite observations of  $\log(C_k L)$  (light solid line) for all SSN and  $3^\circ \leq K_p \leq 4^\circ$ .

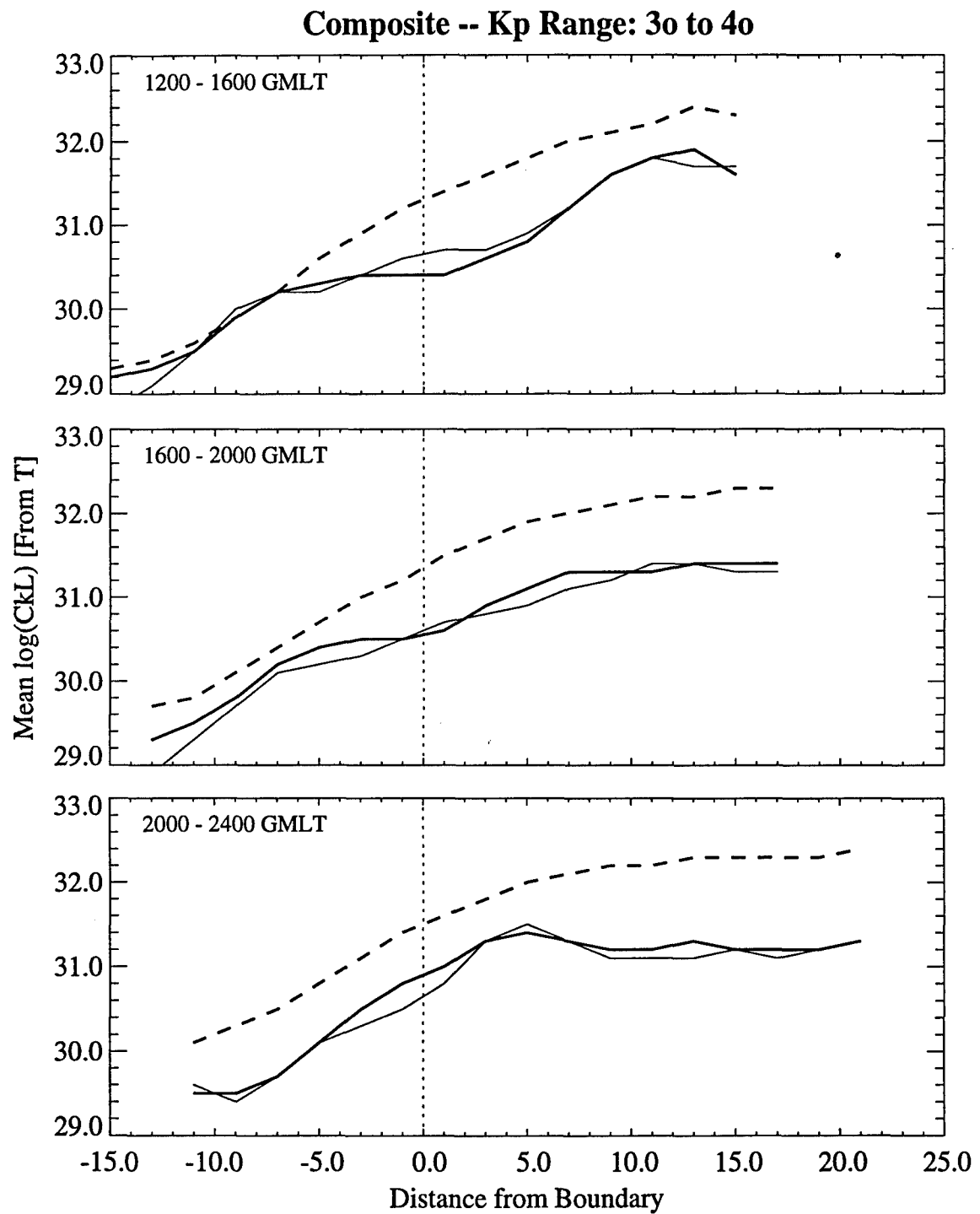


Figure 54: Continuation of comparison in Figure 53.

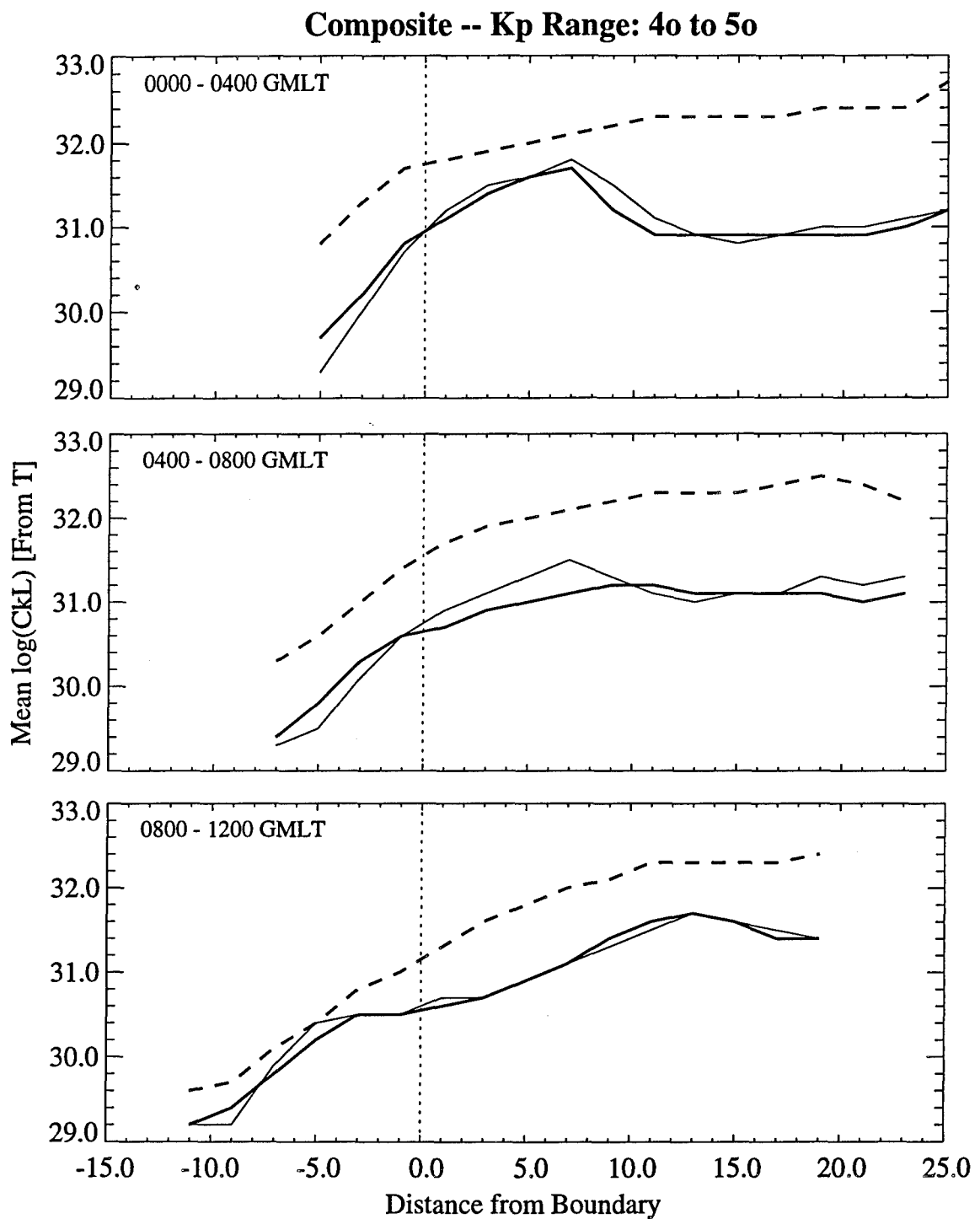


Figure 55: Comparison of WBMOD Version 12.02 (heavy dashed line) and SCINTMOD Version 1.0 (heavy solid line) to composite observations of  $\log(C_k L)$  (light solid line) for all SSN and  $4^\circ \leq K_p \leq 5^\circ$ .

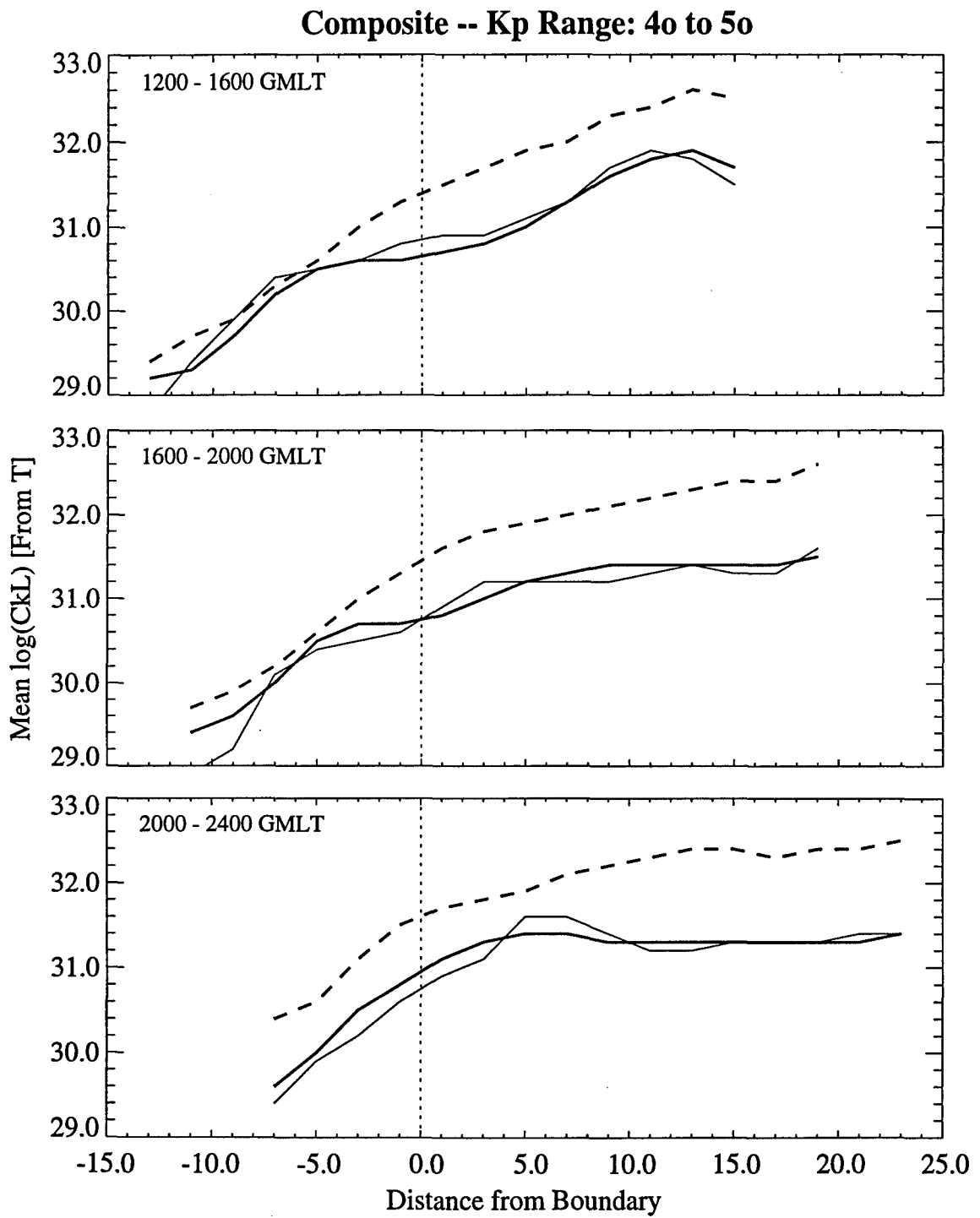


Figure 56: Continuation of comparison in Figure 55.

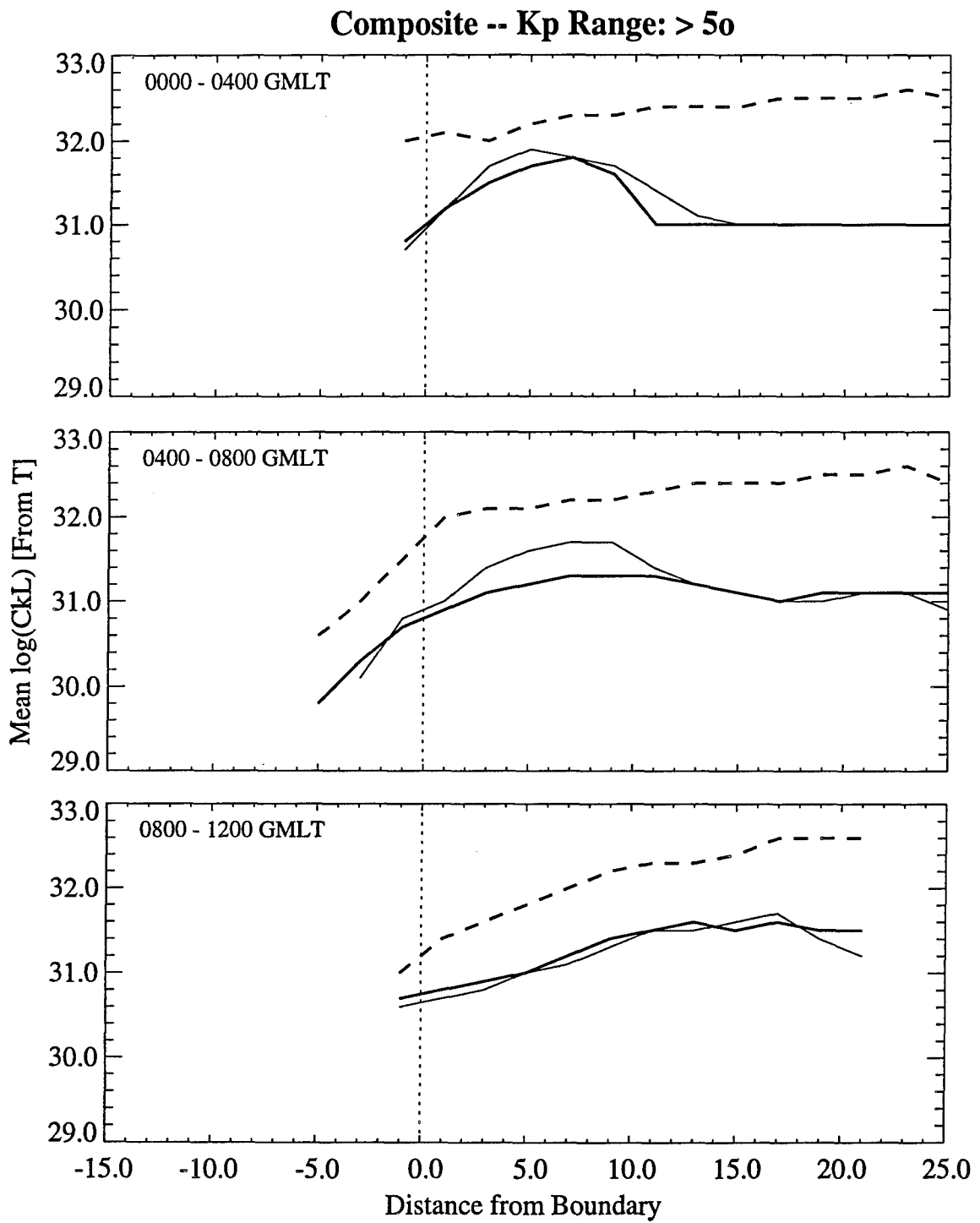


Figure 57: Comparison of WBMOD Version 12.02 (heavy dashed line) and SCINTMOD Version 1.0 (heavy solid line) to composite observations of  $\log(C_k L)$  (light solid line) for all SSN and  $K_p \geq 50$ .

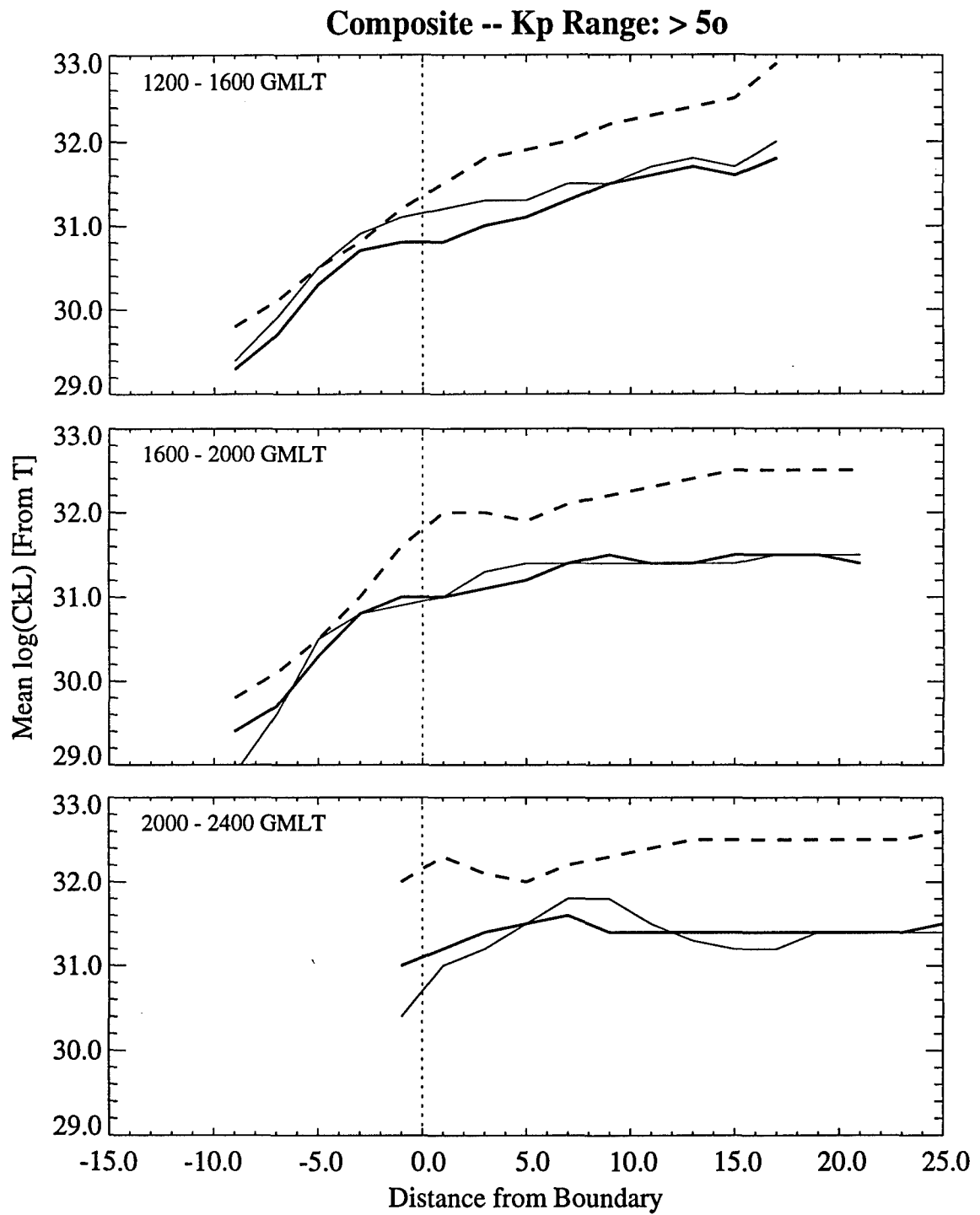


Figure 58: Continuation of comparison in Figure 57.